TECHNICAL UNIVERSITY OF CRETE
SCHOOL OF PRODUCTION ENGINEERING & MANAGEMENT
TURBOMACHINES & FLUID DYNAMICS LABORATORY

Diploma Thesis

Design and analysis of a Formula Student Vehicle

Matthaios K. Lilikakis

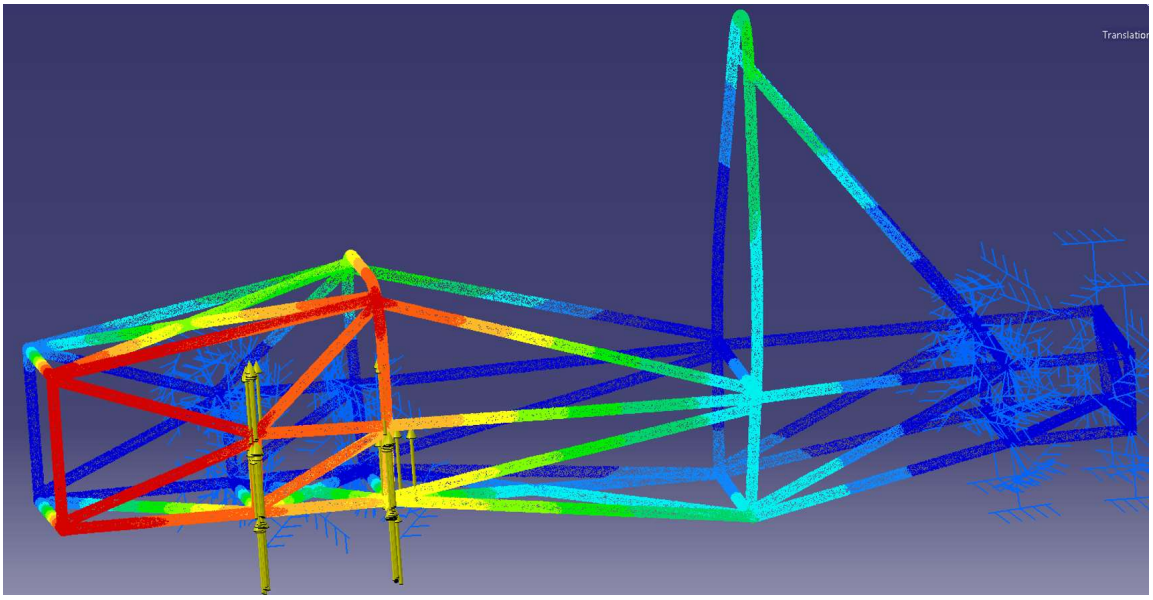

Supervisor: Prof. Dr. Ioannis K. Nikolos

Chania, November 2024

ΠΕΡΙΛΗΨΗ

Αυτή η διπλωματική εργασία έχει ως στόχο να παρουσιάσει τη διαδικασία μοντελοποίησης του χωροδικτυώματος-σκελετού (σασί) του αγωνιστικού μονοθέσιου που αναπτύχθηκε από την ομάδα Formula Student του Πολυτεχνείου Κρήτης (FSTUC) με τις πραγματικές διαστάσεις του (αφού κατασκευάστηκε) και την μελέτη της στρεπτικής ακαμψίας του. Έπειτα από λεπτομερή και ακριβή μέτρηση του πραγματικού σασί, έγινε από την αρχή η τριδιάστατη σχεδίασή του σε λογισμικό CAD. Η δημιουργία του πλέγματος γραμμών αποτελούμενο μόνο από κόμβους και γραμμές, τοποθετημένα βάσει των νέων μετρήσεων, ήταν το πρώτο βήμα του σχεδιασμού. Πάνω στο αρχικό αυτό σχέδιο του σασί, ξεκίνησε η ανάπτυξη επιφανειών, οι οποίες έδωσαν μορφή στο σχέδιο. Ακολούθησε η μετατροπή των παραπάνω κυλινδρικών επιφανειών σε όγκους, οι οποίοι έδωσαν τη τελική μορφή του σχεδίου, καθώς το πραγματικό σασί είναι κατασκευασμένο από ατσάλινους κυλινδρικούς σωλήνες. Το επόμενο βήμα της μελέτης αυτής ήταν η στρεπτική ανάλυση της κατασκευής. Με τη δημιουργία κατάλληλου τετραεδρικού πλέγματος για την διακριτοποίηση της γεωμετρίας, την ακινητοποίηση των τριών αναρτήσεων και την επιβολή φορτίων στην περιοχή της ελεύθερης εμπρόσθιας ανάρτησης, έγινε προσομοίωση του σασί σε στρεπτική φόρτιση. Στόχος ήταν η λήψη δεδομένων για την αντοχή της κατασκευής και ο εντοπισμός των σημείων που επιδέχονται βελτίωσης σε μελλοντικό νέο σασί για το μονοθέσιο. Τα αποτελέσματα που προέκυψαν ήταν θετικά ως προς την αντοχή της κατασκευής και την παραμόρφωσή της σε υψηλά φορτία και η προσομοίωση υπέδειξε τις (λίγες) περιοχές όπου εμφανίζονται υψηλές τάσεις.

ABSTRACT

This Diploma Thesis presents the process of modeling the chassis of the car prototype developed by the Formula Student team of the Technical University of Crete with the real dimensions of it and the study of its torsional stiffness. After detailed and precise measurement of the chassis' dimensions, it was redesigned in 3D CAD software. The first step was the design of the wireframe, consisting of points and lines placed according to the new measurements. The wireframe was the basis for the development of cylindrical surfaces. They were designed around the lines so they began to give shape to the structure. Based on those surfaces, volumes of cylindrical tubes were constructed for the final geometry of the chassis. The next step of this study was the torsional analysis of the structure. The optimal meshing for the discretization of the geometry, the clamped suspension areas and the placement of loads on the last moving suspension, were the necessary steps for the simulation of the chassis. The structure was simulated with the purpose of collecting useful data for chassis durability and pinpointing the areas where will be further improvement in the future design.

ΕΥΧΑΡΙΣΤΙΕΣ

Θα ήθελα να ευχαριστήσω θερμά τον επιβλέποντα καθηγητή της διπλωματικής μου εργασίας, κ. Νικολό Ιωάννη για την εμπιστοσύνη που μου έδειξε, τη καθοδήγηση που μου προσέφερε, τις πολύτιμες συμβουλές που μου έδωσε και για τις ουσιαστικές παρατηρήσεις του, που βοήθησαν στην ολοκλήρωση αυτής της εργασίας, καθώς αποτελεί την ολοκλήρωση των σπουδών μου στο τμήμα Μηχανικών Παραγωγής και Διοίκησης του Πολυτεχνείου Κρήτης.

ACKNOWLEDGMENTS

I would like to warmly thank the supervisor of my diploma thesis, Professor Dr. Ioannis K. Nikolos, for his trust on me, the guidance he offered me, the valuable advice he gave me and his significant observations that helped in the completion of this work, as it represents the completion of my studies in the School of Production Engineering and Management, Technical University of Crete.

Contents

Table of Figures

1. Introduction

The goal of this Thesis is to create a digital CAD model of the chassis of the Formula Student TUC racing car prototype (2023 model) and conduct a Finite Element Analysis (FEA) and more specifically, a torsional stress analysis.

The Formula Student team of the Technical University of Crete (FSTUC) developed a racing car according to the Formula Student 2023 rules. After the construction of the chassis, detailed measurements of it were applied, and according to them, the development of the 3D model in CATIA V5 (CAD/CAE software) was accomplished. The FSTUC team had already designed a 3D prototype of the chassis before constructing it in real life but various deviations have been observed between the CAD model and the actual chassis. The purpose of developing a new 3D model from the start, based on the real dimensions of the constructed chassis, was to study the mechanical characteristics of it and be as close to the real chassis as possible.

Following up the chassis design, the FEA was conducted also in the environment of CATIA V5. The steel properties were specified and after deciding about the ideal type of mesh to approximate the geometry of it and exerting loads on it, the chassis was ready for the stress simulations. The stress simulations gave the expected results and approved the structure characteristics and performance under extreme conditions.

2. State of the art

2.1 Aerodynamic analyses

There are lot of scientific studies concerning the aerodynamic analysis and optimization of Formula SAE and Formula Student racing cars which the use of CFD analysis. To find the optimal aerodynamic design, analyses of different models are usually necessary. Through these computational experiments, switching between car design characteristics is generally easy, and different combinations provide different results; some of the available studies in the open literature will be presented in the following.

In the study of (Tzanakis, 2012) a racing car was designed (***Figure 1***), while the variations of the model design were simulated in ANSYS CFX. At first, some simplifications to the design have been applied for the purpose of making the flow simulation easier; the wheels of the vehicle were assumed as stationary, all different parts were computed as one solid part and some of the rims were considered as closed surfaces.

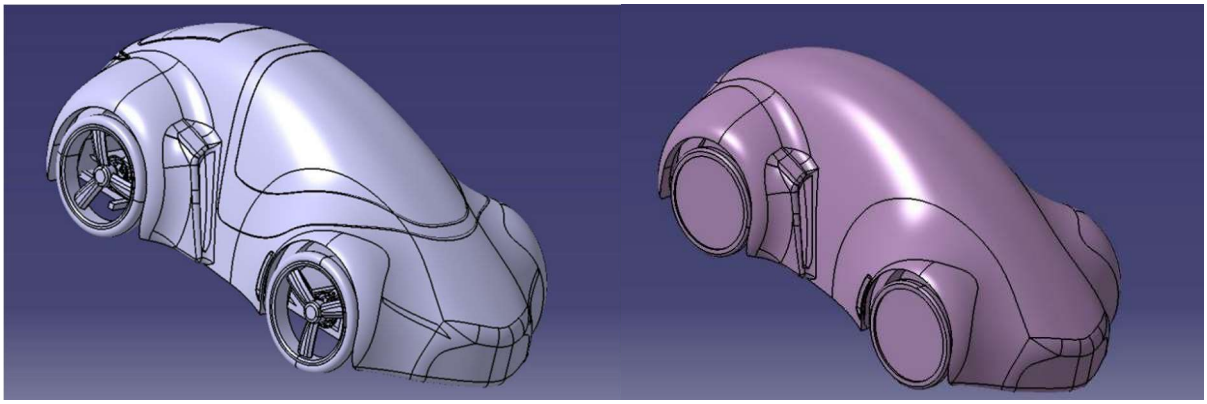

Figure 1: Two stages of the surface design of (Tzanakis, 2012).

The construction of the flow domain is considered only the half of the car, due to symmetry. As a result, the mesh generation was simpler and the simulation time was smaller, as only half of the flow domain was simulated (***Figure 2***).

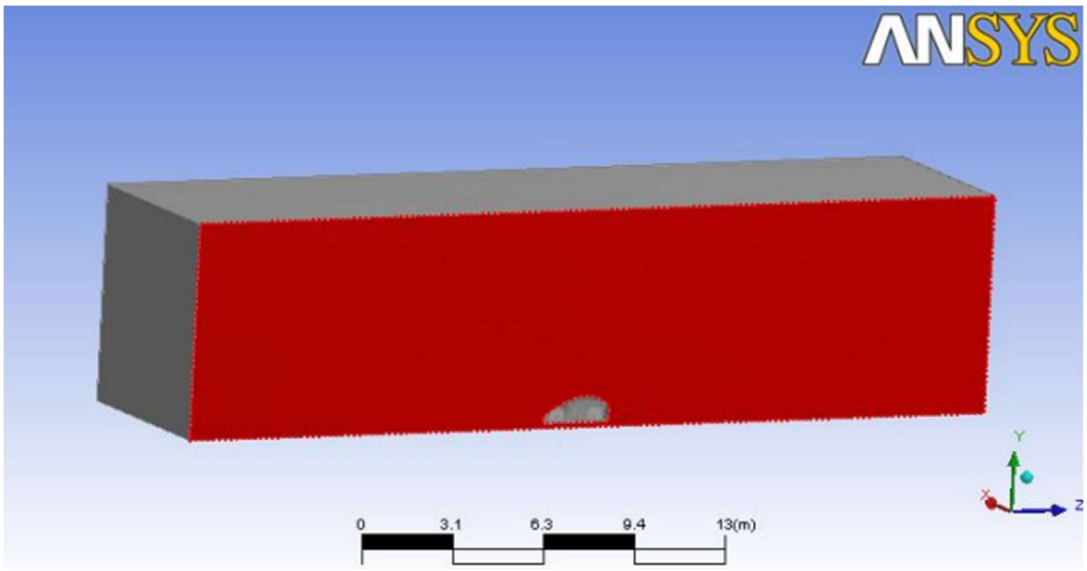

Figure 2: The flow domain of the racing car of (Tzanakis, 2012).

The first design was used as the reference one, with which the rest of the models were compared to; it was characterized by a high drag formation in the rear area of the car and a large pressure difference between the front area and the rear area. To change this, a rounder design of the front area was proposed along with an extension of the rear side, as depicted in ***Figures 3, 4*** and ***5***.

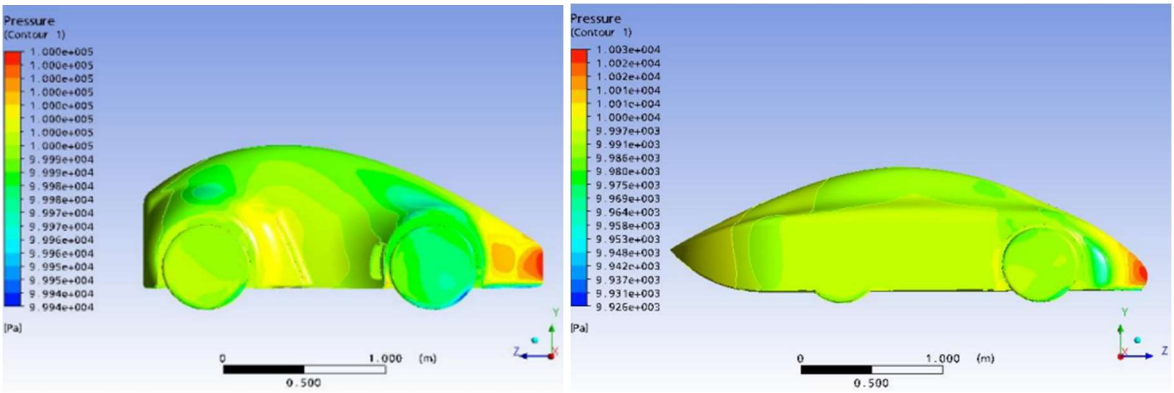

Figure 3: Pressure contours on the surface of different types of the racing car of (Tzanakis, 2012).

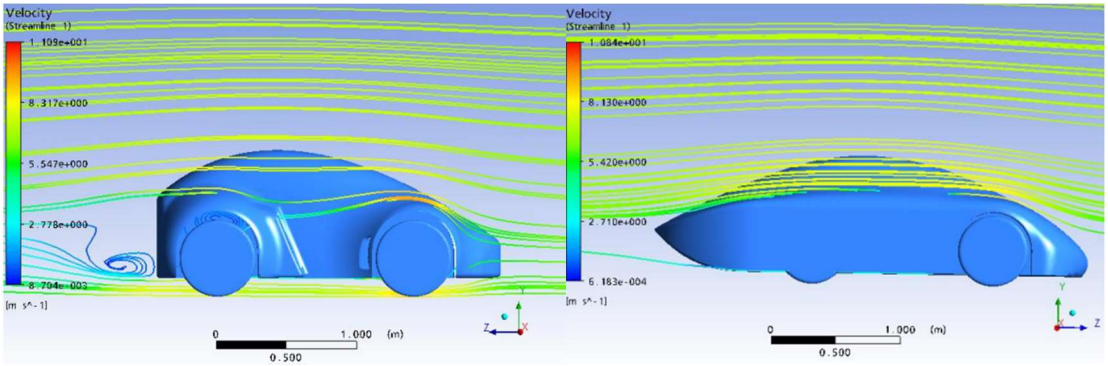

Figure 4: Streamlines around the surface of different types of the racing car of (Tzanakis, 2012).

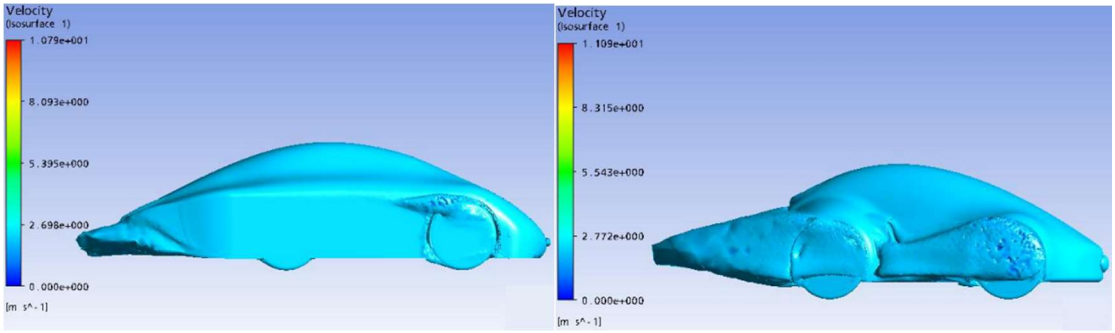

Figure 5: Velocity iso-surfaces around the surface of different types of the racing car of (Tzanakis, 2012).

With these modifications the drag formation was reduced by 56% and the overall efficiency was improved. The different car models were compared based on their aerodynamic efficiency with the construction of a flow domain and the final decision of the model was taken based on the weight, cost of the construction material, and the aesthetics. Also, another factor taken into consideration was the power consumption of the car to maintain a constant velocity of 25 *km/h*.

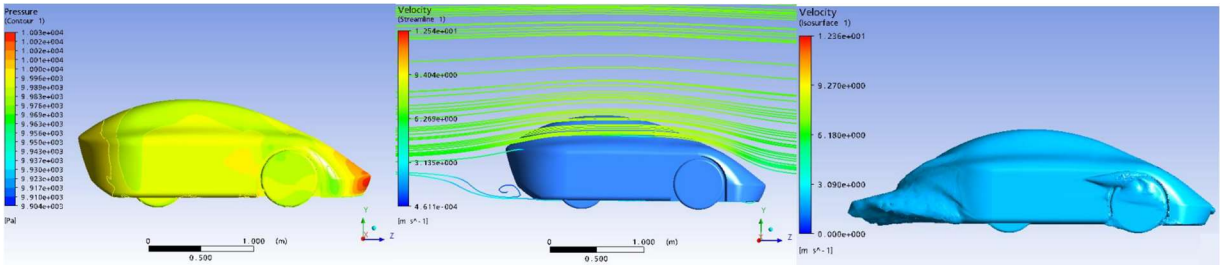

Figure 6: The alternative car design: flow simulation results (Tzanakis, 2012).

An alternative design was then produced and tested (***Figure 6***). The front and rear side areas of the model were smaller, the distance between the wheels was reduced and a more curved rear side design was implemented. The overall size and weight of the vehicle was reduced, having in addition better turning circle capabilities.

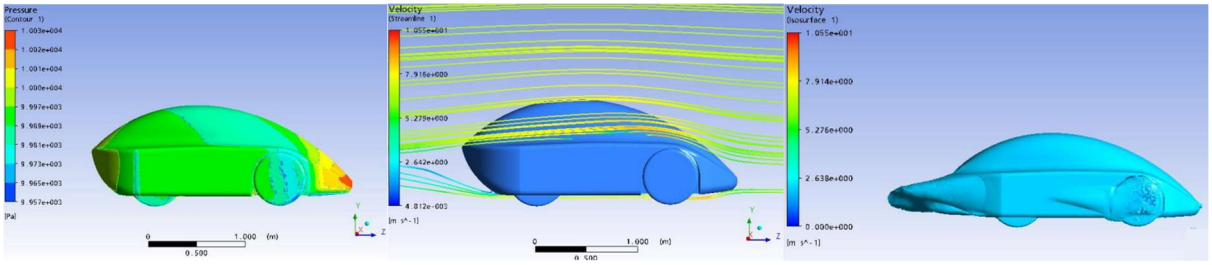

Figure 7: Visuals of third design's pressure and velocity simulations (Tzanakis, 2012).

The third design (***Figure 7***) was a modified version of the previous one. A comparison between the three designs is included in ***Figure 8***. The final real-life carbon-fiber surface that was constructed, is presented in ***Figure 9*** (Tzanakis, 2012).

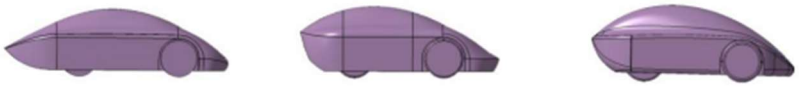

Drag Coefficient(C_d)	0.19	0.23	0.21
Weight(kg) (4 Carbon fiber layers)	10kg	9kg	8.2
Cost (€)(of carbon fiber)	€984	€852	€780
Aesthetic	★	★★	★★★

Figure 8: Table of comparison of the three models of the car (Tzanakis, 2012).

Figure 9: Final real-life carbon-fiber made surface (Tzanakis, 2012).

In the next study of (Parmar, et al., 2018) all the different car models were subjected to air flow simulations for the purpose of optimizing the minimum drag and vehicle stability, by calculating the pressure and velocity fields around the alternative models. The main car characteristics of this investigation are the side rod, the firewall vent, the front spoiler and without it (***Figure 10***).

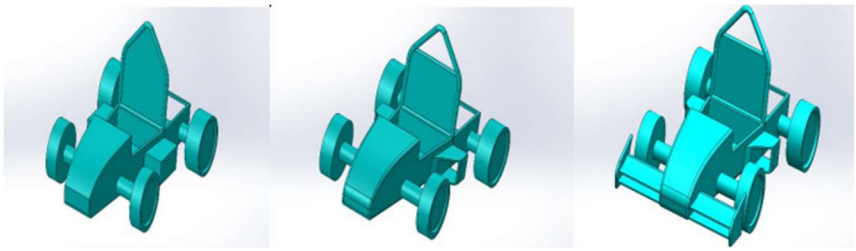

Figure 10: The three simulated car models of (Parmar, et al., 2018).

The three models were tested in a wind tunnel sized flow domain, and the simulation parameters were set in accordance (***Figure 11***).

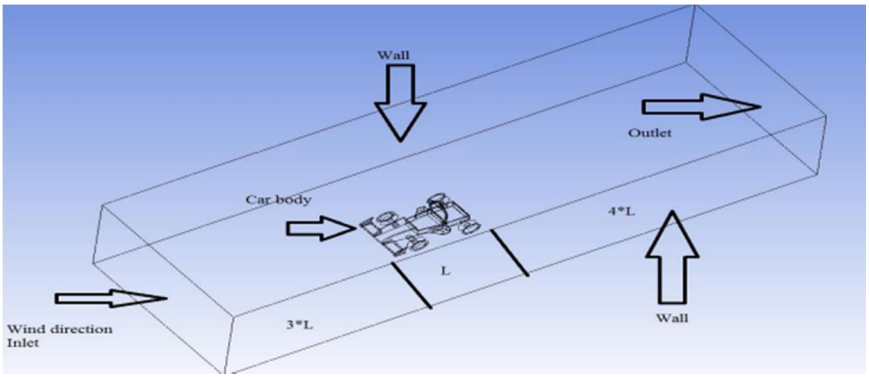

Figure 11: The flow domain used in (Parmar, et al., 2018).

After the meshing of each flow domain was completed, the analysis of the air flow was accomplished using CFD simulations. For all three models the inlet velocity was set to 30 *m/s*. Visual representations of surface pressure contours and streamlines around the alternative models are presented in the following ***Figures 12 – 14***.

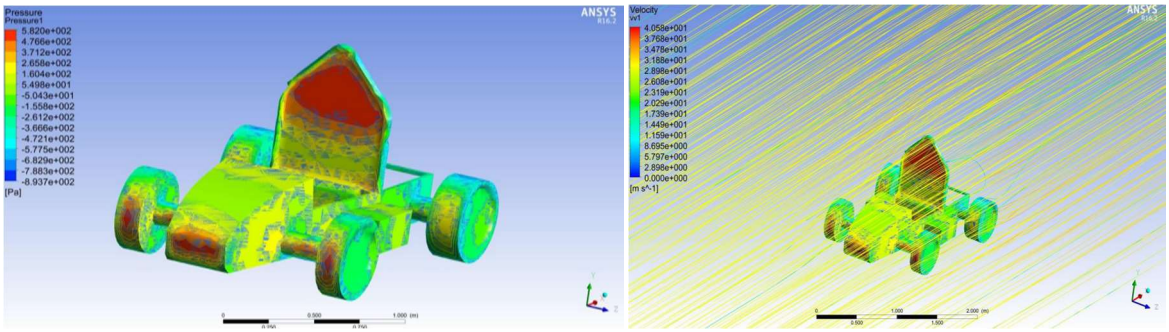

Figure 12: Pressure contours and streamlines for the first car model of (Parmar, et al., 2018).

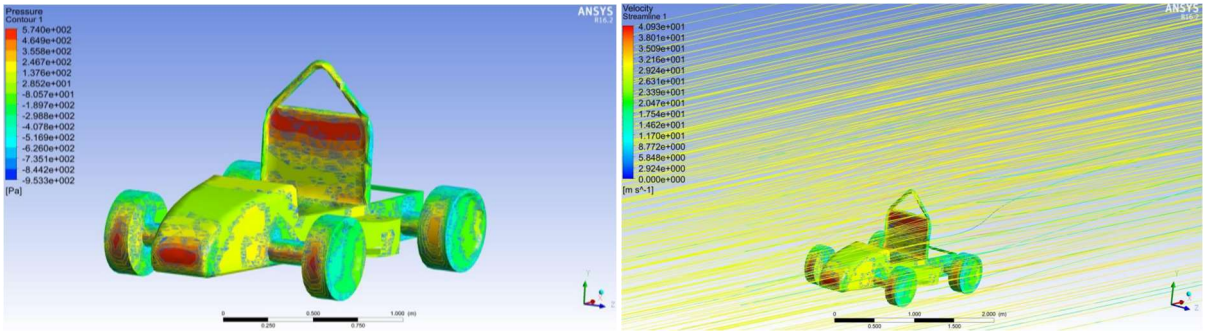

Figure 13: Pressure contours and streamlines for the second car model of (Parmar, et al., 2018).

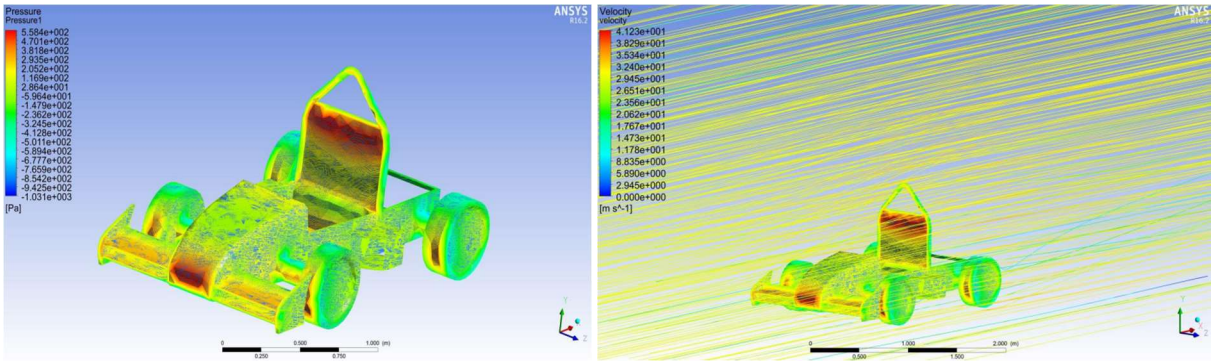

Figure 14: Pressure contours and streamlines for the third car model of (Parmar, et al., 2018).

The graphs of drag and lift coefficients were plotted for each model and the results showed that the modified model performed better than the base one. The firewall cut and the side rod reduced the drag as the vent made some space for the air to flow through it (***Figure 13-14***). The front spoiler increased the downforce and reduced the lift providing better stability and grip to the car (Parmar, et al., 2018) .

At the University of Perugia (Mariani, et al., 2015) a wind tunnel (***Figure 15***) was used for the testing of a part of a racing car, while these experimental results were then used in combination with the results of a CFD analysis.

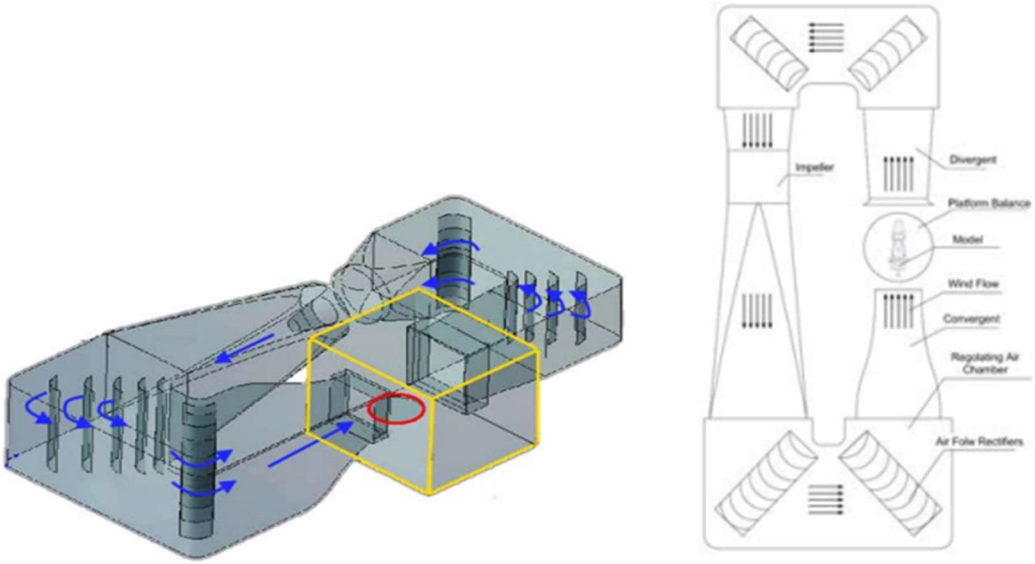

Figure 15: The wind tunnel used in the work of (Mariani, et al., 2015).

The goal of this study was to decrease the vehicle's drag and to increase its down-force. The differences of the models that were compared in this study were the installation of a front wing, rear extractors and rear hood and the removal of excess headrest. The part of the car that was put in for testing in the wind tunnel was the nose of the vehicle (***Figure 16***).

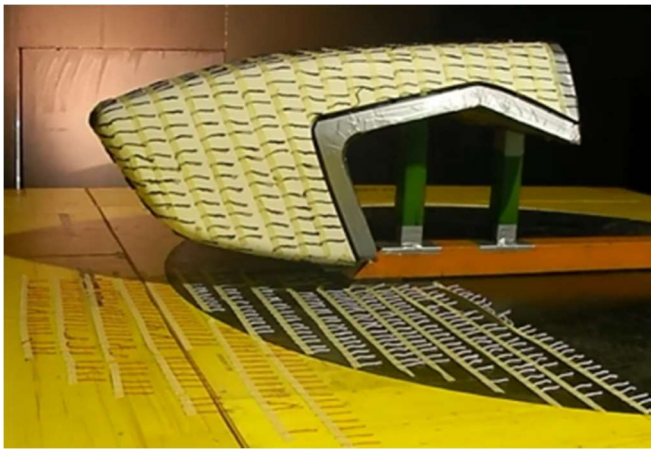

Figure 16: The nose of the vehicle of (Mariani, et al., 2015).

The test was carried out in a set speed of 85 *km/h*. The experimental values of the drag coefficient helped the selection of the optimal mesh of the CFD models. The comparison of the experimental results with the numerical results of the C_d showed that the first had a value of 0.43 and the simulation value was 0.46, an error of only 6%. As it is reported, the applied

modifications to the car improved the overall results (***Figures 17-20***). The removal of the excess surface of the headrest reduced the drag, as the air flowed through the opening (***Figure 17***).

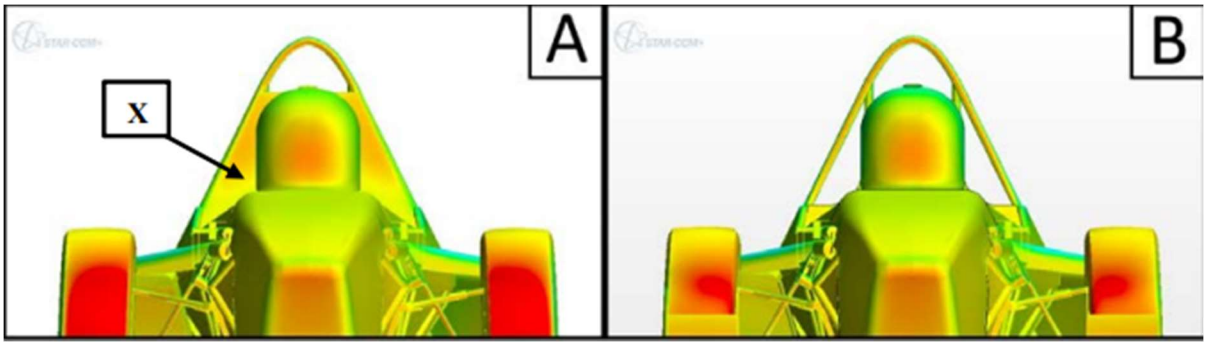

Figure 17: Before and after the improvement in the firewall of (Mariani, et al., 2015).

The addition of the front wing and rear air extractors reduced the total pressure of the car and generated positive down-force (***Figures 18-20***).

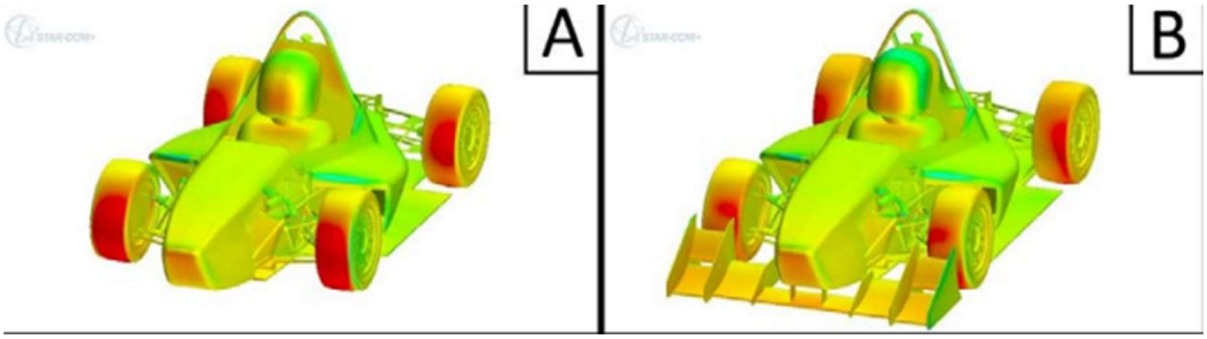

Figure 18: Before and after the addition of the front wing of (Mariani, et al., 2015).

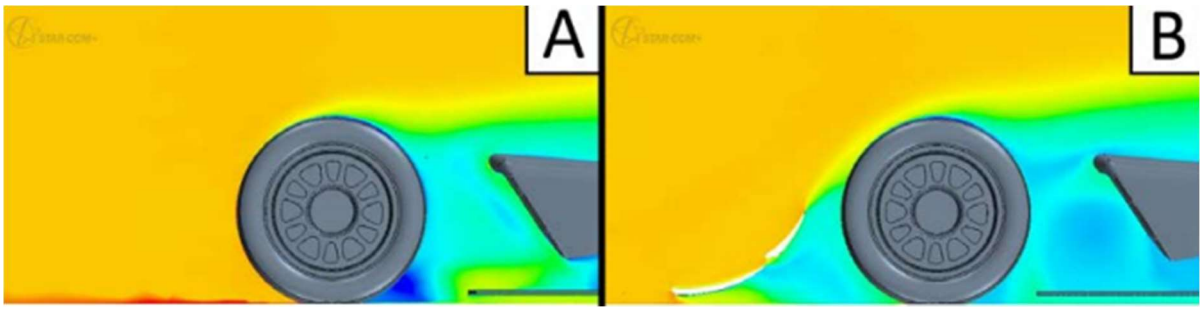

Figure 19: The difference of the air flow before and after the installation of the front wing of (Mariani, et al., 2015).

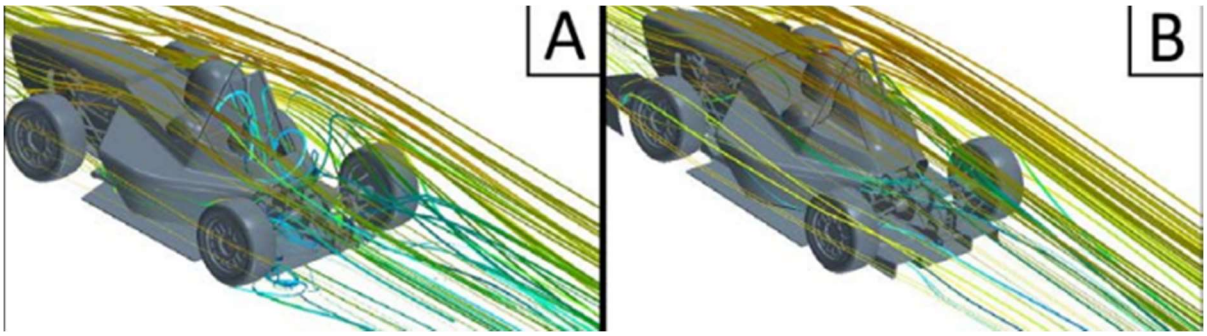

Figure 20: The difference in air diversion after the installation of the front wing of (Mariani, et al., 2015).

More specifically, the front wing diverted the air to the top of the shell and this also helped with the reduction of drag in the wheel area. The streamlines allowed the flow visualization, so the overall improvement between the two models was clearer (Mariani, et al., 2015).

The wind tunnel experiment with combination of CFD analysis was also used in another study (Hetawal, et al., 2014) but this time the only conditions were a car without tires, as well as a car with tires. This differentiation shows the percentage in overall drag coefficient in which the tires and wheels account for.

The tunnel model was made at 1/10th scale and it was tested at 10-30 *m/s* speed (***Figures 21***). The result was a drag coefficient of 0.48 but the lift coefficient wasn't calculated because of the balance system of the model.

Figure 21: The wind tunnel and the 1/10 scale model used (Hetawal, et al., 2014).

The simulation results of the car without tires showed low drag coefficient of 0.312 and a smooth flow at the front part of the car but around the cockpit area and the engine bonnet turbulence and large vortices appeared (***Figure 22***). The car with tires had a higher drag coefficient of 0.42, so that meant that the tyres and wheels are causing 25.7% of the drag (***Figure 23***). Also, the car with tires generated lift and made the turbulence at the back of the car even worse.

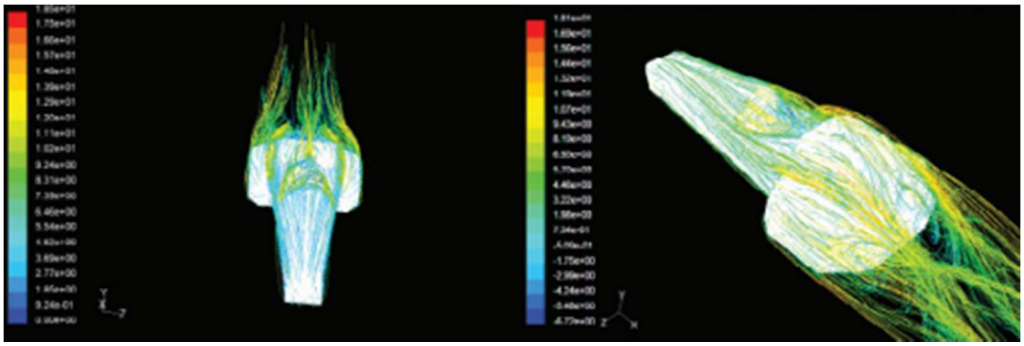

Figure 22: Visualization of air flow simulation without front wheels (Hetawal, et al., 2014).

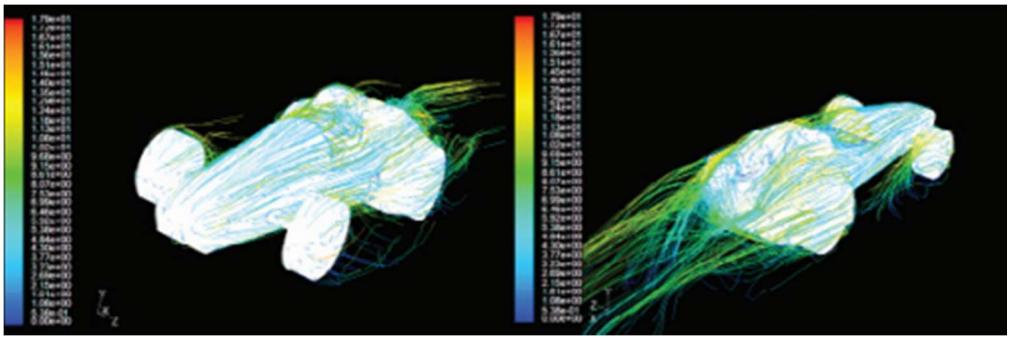

Figure 23: Visualization of air flow simulation with front wheels (Hetawal, et al., 2014).

An important difference between wind tunnel experiment and CFD was that in the first one the flow was viscous so it's natural for the wind tunnel's result to have higher drag. The difference between the drag coefficient of the experimental and numerical was 12.5%.

To enhance the stability of the car and reduce the drag a CFD simulation took place and compared three models of a SAE formula car (***Figures 24-26***). The flow analysis for all the models was at a set speed of 25 *m/s* and the results were plotted in graphs. At this study also, for the sake of the reduction of the required computational time, its symmetry allowed that half of the car model to be used for the simulation.

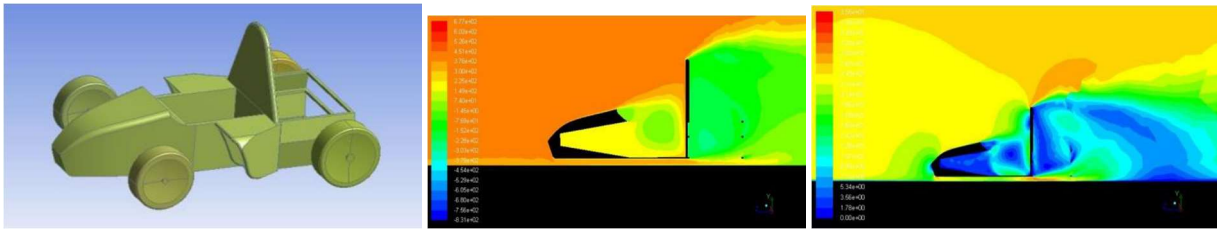

Figure 24: Visualization of pressure and velocity simulation results for the first model (Hetawal, et al., 2014).

The second model had a cut in the firewall for drag reduction since it allowed the air flow and reduced the overall pressure at the driver's space (***Figure 25***). The drag coefficient was found to be equal to 0.75, while in the first model was equal to 0.85. For further improvement in those areas and for the total pressure reduction and velocity increase, more adjustments had been made in the next model.

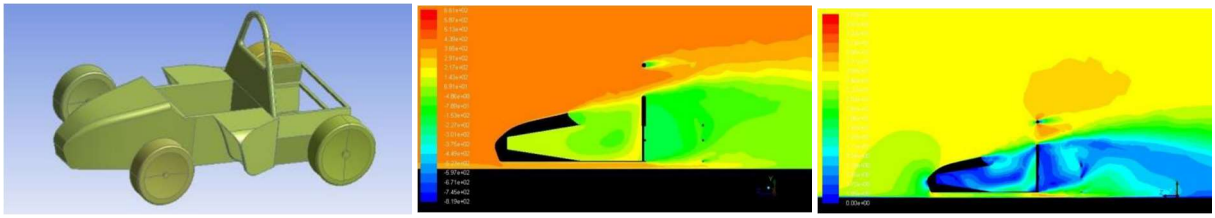

Figure 25: Visualization of pressure and velocity simulation results for the second model (Hetawal, et al., 2014).

The addition of the front wing in the third model caused a reduction of the lift and the improvement of the car stability (***Figure 26***). The C_d was found to be 0.7 and the lift coefficient reduced from the first model from 0.2 to -0.25. Furthermore, in comparison with the first model (***Figure 24***), there was a reduction in the total pressure from 340 *Pa* to 80 *Pa* and an increase in velocity from 26 *m/s* to 32 *m/s*.

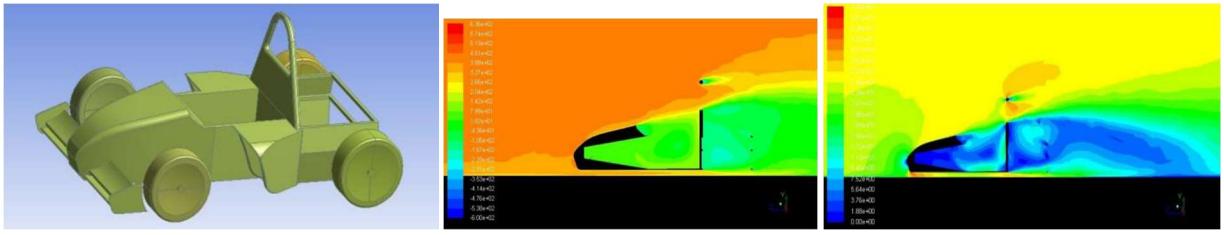

Figure 26: Visualization of pressure and velocity simulation results for the third model (Hetawal, et al., 2014).

Starting with the simplest version and continuing with cut out in the firewall and the addition of a front wing, the latter gave better aerodynamic results in every aspect that this study included (Hetawal, et al., 2014).

A multi-element wing design and simulation took place in (Jackson, 2018) and showed that can withstand higher angles of attack and produce grater downforce than a single-element wing. The speed of the air was set at 26.8 *m/s*. To reach the optimal design, parameters such as the angle, overlap and the gaps between the main element and the flaps, were taken into consideration and a lot of combinations of different values were made. The main element was equal to 540 mm, the flaps 180 mm and the overlap of them was equal to 26.25 mm (***Figure 27***). The main gap was equal to 20 mm. The symmetry of the wings was used to reduce the computational time.

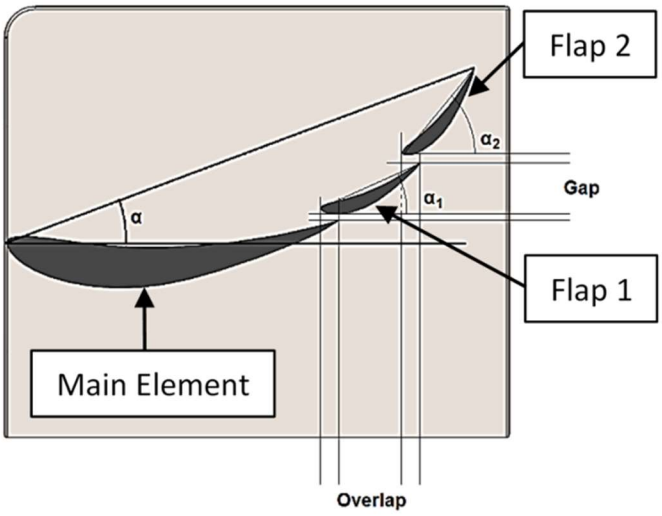

Figure 27: Flap design (Jackson, 2018).

The various configurations between the flaps that were made are presented to the following table (***Figure 28***).

Study No.	Flap 1 AOA (degrees)	Flap 2 AOA (degrees)	Overall AOA (degrees)
0	20	20	13.80
1	25	30	16.65
2	26	40	18.73
3	27	50	20.80
4	28	60	22.81
5	29	70	24.71

Figure 28: Table of values of different studies (Jackson, 2018).

The fourth study is preferred because the car had the largest downforce generated without stall (***Figure 29***).

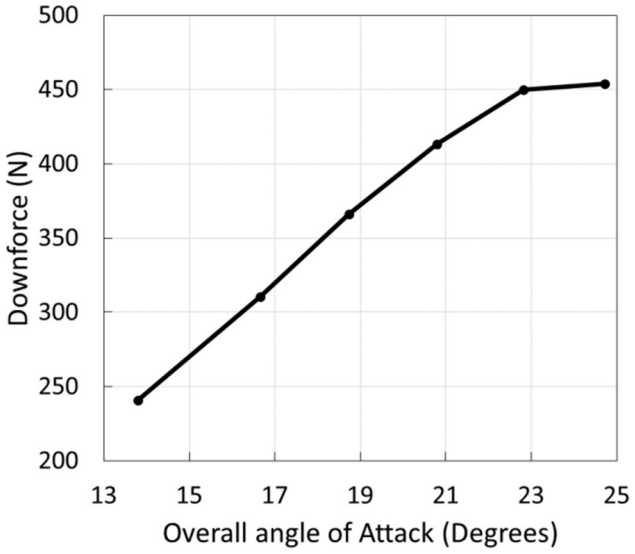

Figure 29: Downforce-Angle of Attack graph (Jackson, 2018).

A comparison of the drag force, car velocity, cornering speed and radius of the corner was also made with the DRS mechanism open and closed (***Figure 30***). When the DRS is open, the car has low drag and when it is closed the car has high downforce. The results showed that with the DRS closed the drag coefficient was 1.21 and with the DRS open it was 0.79, which is a 35% reduction. The lift coefficient also had a large reduction, since with the DRS closed it was equal to 1.15 and with the DRS open it was equal to 0.26.

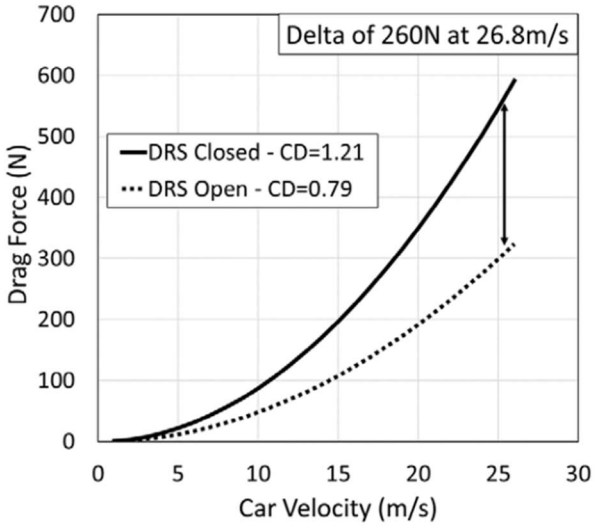

Figure 30: Drag Force-Velocity graph (Jackson, 2018).

As for cornering speed, the car with a rear wing performed better with a 3.1% improvement for a corner radius of 13 m (***Figure 31***).

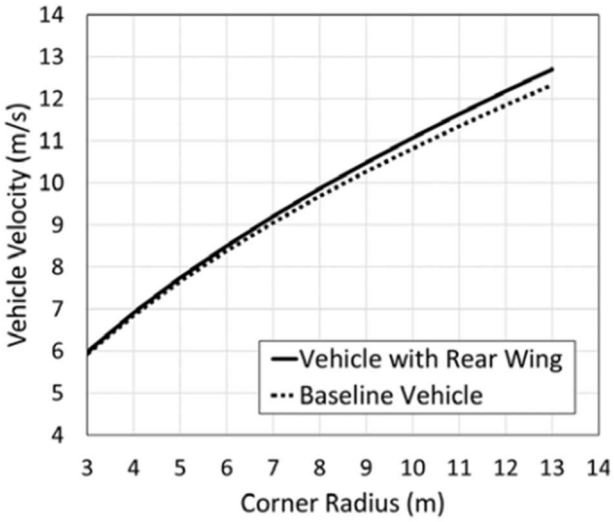

Figure 31: Velocity-Corner Radius graph (Jackson, 2018).

Next, the acceleration of the vehicle was studied at the velocity of 25 *m/s*. The option of DRS open increased the potential of acceleration by 15.7%, as depicted in ***Figure 32***.

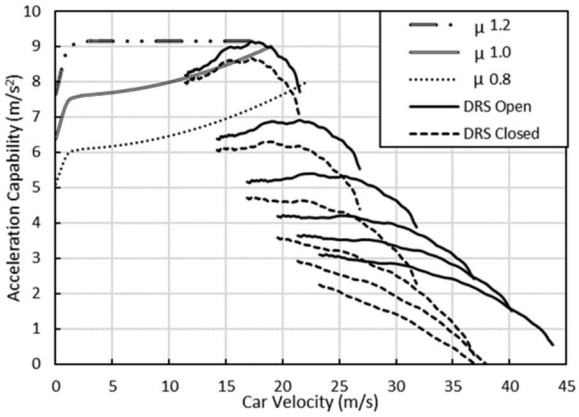

Figure 32: Acceleration Capacity-Velocity graph (Jackson, 2018).

The overall improvements were meant to make the car more competitive in dynamic events (Jackson, 2018).

The next study of (Jalappa, 2015) aimed to observe how the inlet area of an under tray of a car could change the lift coefficient (***Figure 33***). The first part was a two-dimensional analysis of the inlet angle and it was studied with two approaches. In the first approach only the inlet angle changed and the length remained unchanged. On the contrary, in the second approach the inlet angle was fixed and the length of it was changed. The velocity for all the models was set at 15 *m/s*, 22.5 *m/s* and 30 *m/s* (***Figures 34, 35***). The limitations of a 2-D study were known, as it could not capture the air coming from the side and the various vortices that were created within the tunnels. In particular, the 2-D study concerned the way that the inlet ratio affects the throat and diffuser inlet area.

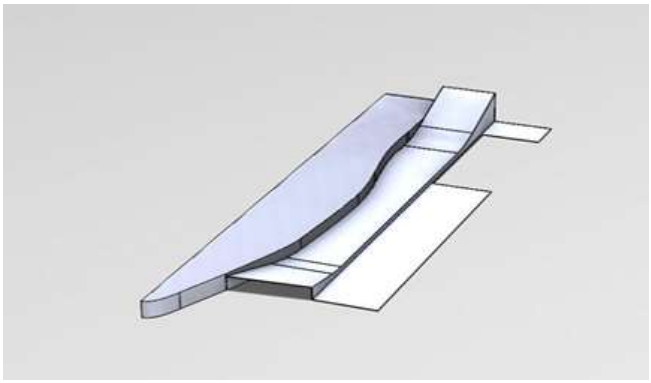

Figure 33: Single diffuser under tray (Jalappa, 2015).

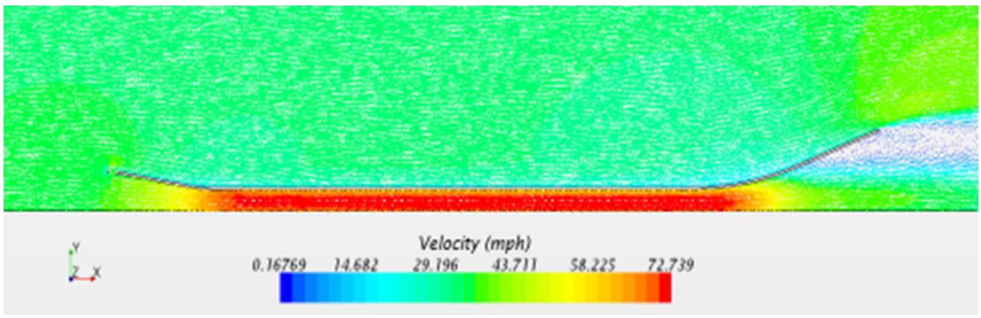

Figure 34: Visualization of the velocity simulation results (Jalappa, 2015).

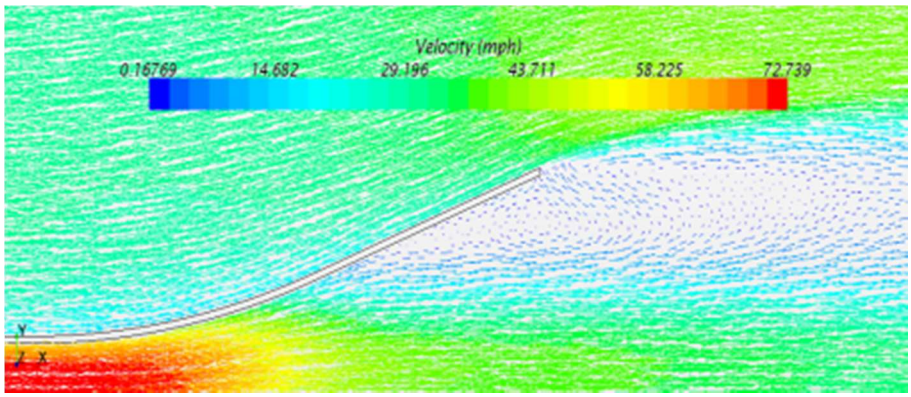

Figure 35: Visualization of the velocity simulation results at the back of the inlet (Jalappa, 2015).

The results of the inlet angle and inlet area ratio showed that as the angle increased, the average lift also increased (***Figures 36, 37***).

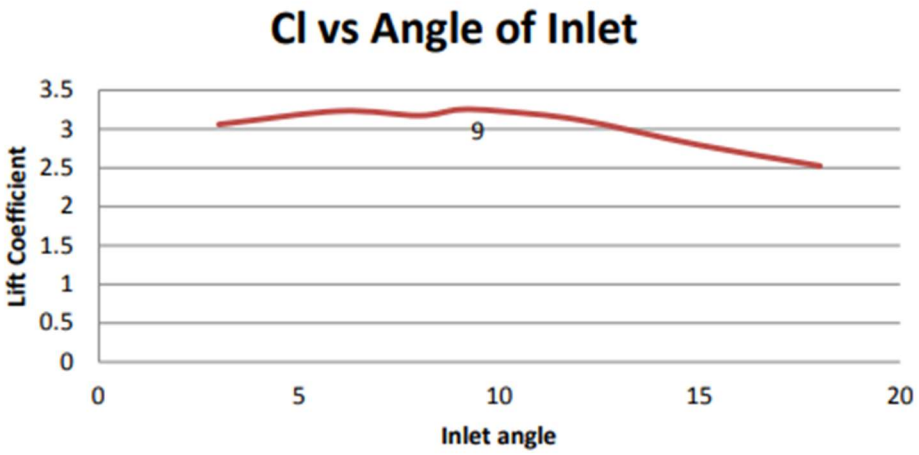

Figure 36: Lift Coefficient-Inlet angle graph (Jalappa, 2015).

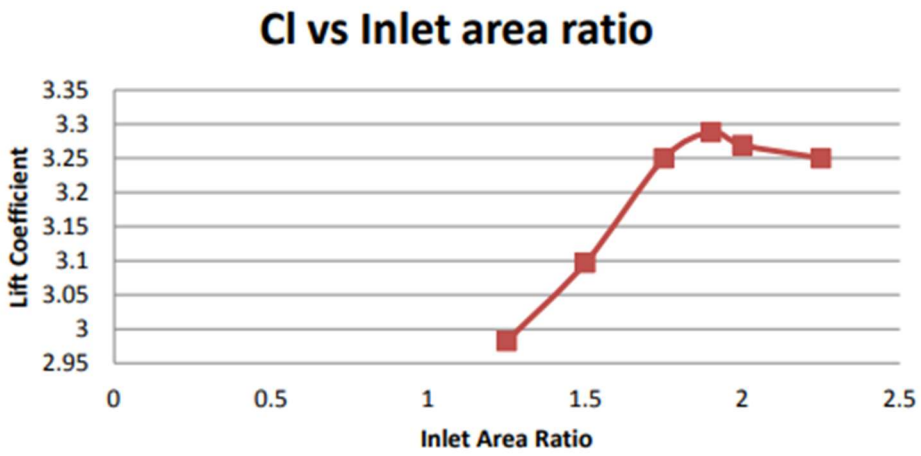

Figure 37: Lift Coefficient-Inlet angle ratio graph (Jalappa, 2015).

In more detail, the inlet angle values were between 1.25 and 2.25 and the lift coefficient values were between 2.98 and 3.25, which showed that at an angle of 3° the C_l was 3.04. With an increase of the angle to 9° the C_l increased by 8% at 3.28 (***Figure 36***). The angle ratio was selected at 1.9 with a C_l of 3.3 (***Figure 37***). The three dimensional analysis tested the different models of the under tray for the purpose of increasing the downforce. All the diffuser models were tested at the same speed as the 2-D simulation. The testing started with the diffuser angle, which was designed so it could move up and down. Two kinds of diffuser designs were simulated, one with a straight diffuser and one with a curved one (***Figure 38***).

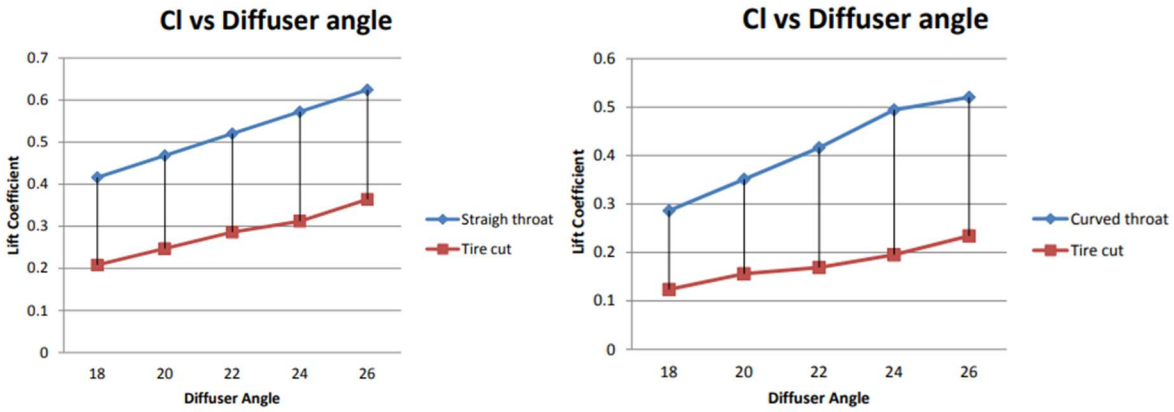

Figure 38: Lift Coefficient-Diffuser angle graphs for straight and curved throat (Jalappa, 2015).

The test conducted on a few specific angles and it showed that as the angle of the straight diffuser increased the lift also increased.

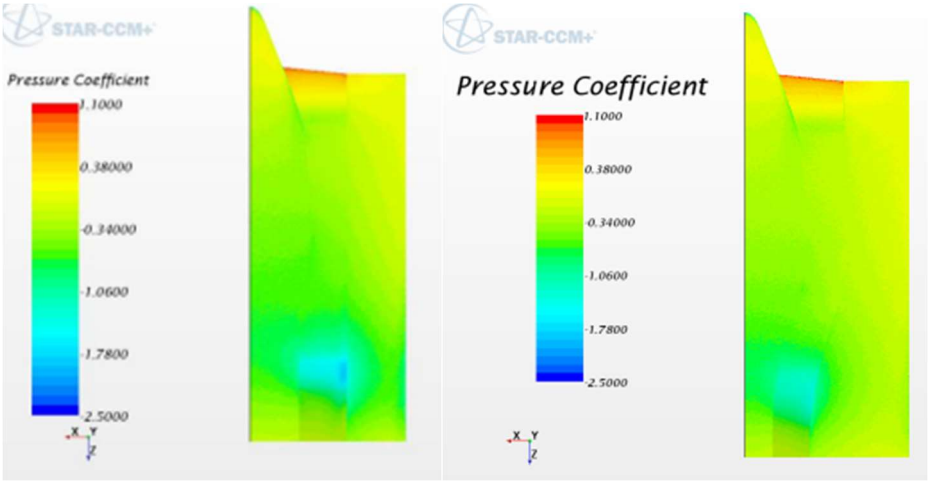

Figure 39: Visualization of the Pressure Coefficient of the diffuser (straight vs curved throat) (Jalappa, 2015).

At 18° the average C_l took values between 0.42 and 0.28 (***Figure 39***).

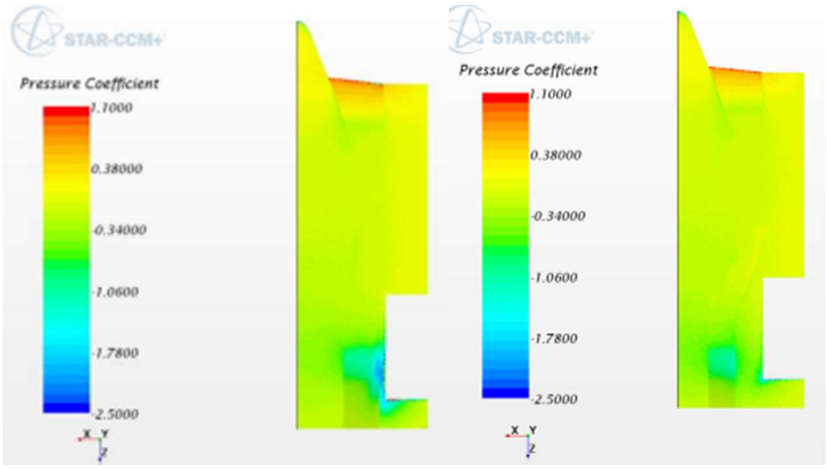

Figure 40: Visualization of the Pressure Coefficient of the diffuser (straight vs curved throat) with tire cut (Jalappa, 2015).

There was also a test that the design had a tire cut and the average C_l was 0.21 and 0.12, meaning that there was 50% reduction (***Figure 40***).

The next characteristic that was studied was the inlet and diffuser radius, with a set angle of 9° for the inlet and 26° for the diffuser (***Figures 41, 42***).

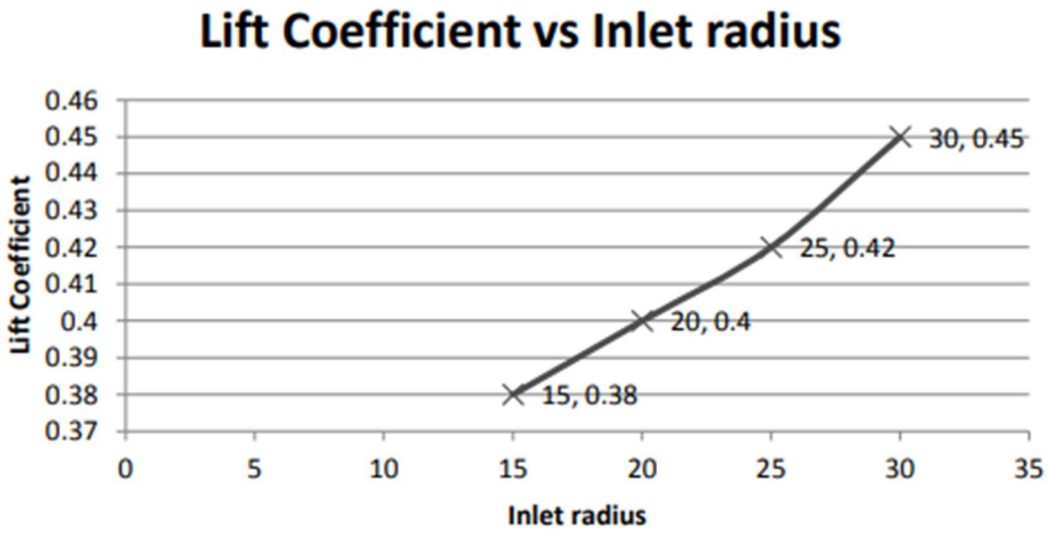

Figure 41: Lift Coefficient-Inlet radius graph (Jalappa, 2015).

The inlet radius test values were 15in, 20in, 25in, and 30in (***Figure 41***).

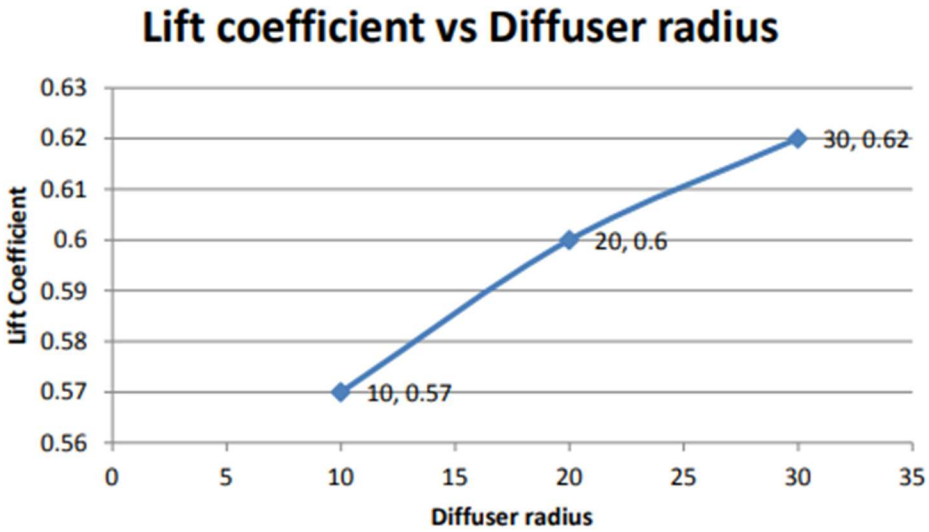

Figure 42: Lift Coefficient-Diffuser radius graph (Jalappa, 2015).

The diffuser radius test values were 10in, 20in, 30in, and 40in. For the inlet and the outlet, the 30in radius was chosen (***Figure 42***).

A second diffuser was designed and it was tested in the same variety of angles, 18° to 26° (***Figure 43***).

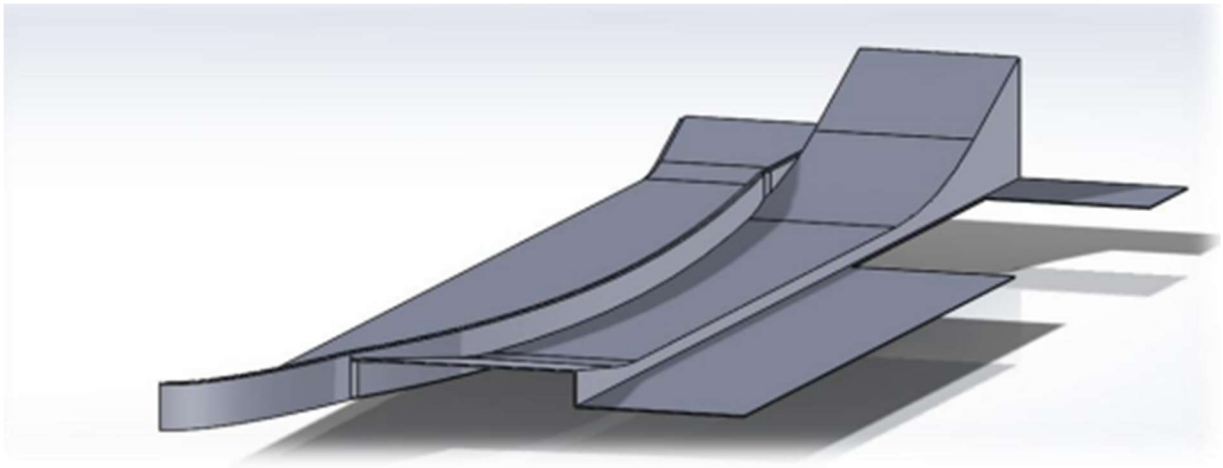

Figure 43: Double diffuser under tray (Jalappa, 2015).

The results showed that the second diffused improved the C_l by 11%, from 0.36 to 0.4 as the ***Figure 44*** depicts.

D1(Angle)	D2(Angle)	Down-force	Cl
26	26	31	.40
26	24	28	.36
26	22	27	.35
26	20	25	.33
26	18	22	.29

Figure 44: Different angle values in accordance with the produced downforce and lift coefficient (Jalappa, 2015).

On the double diffuser model a gurney flap was added so it can maximize the generated downforce. On both diffusers the angle was set to 26° (***Figure 45***).

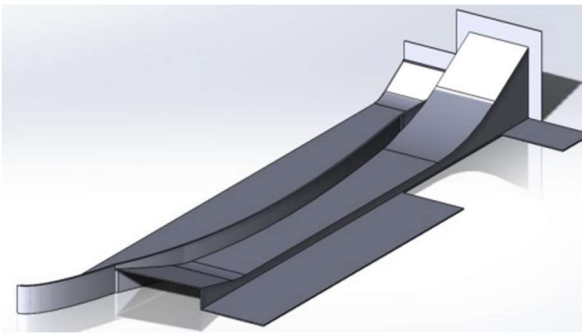

Length	Cl
0.5	0.38
1	0.42
1.5	0.44
2	0.47
2.5	0.48

Figure 45: Double diffuser and table of its length in accordance with lift coefficient (Jalappa, 2015).

A few sizes of the gurney flap were tested and the results showed an increase of 15% of C_l and the one with 2in length was chosen (***Figure 45***).

The final study used the symmetry of the under tray for computational reasons. The parameters of the previous characteristics were set as: the inlet area was 9°, the inlet ratio 1.9, both diffusers were 26° and the gurney flap was 2 in. It tested how the rotating tires affect the under tray (***Figures 46, 47***).

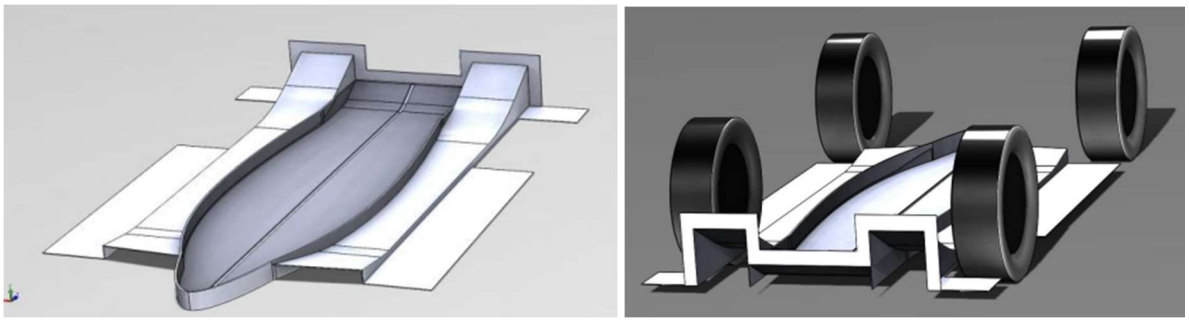

Figure 46: Full under-tray model and full under-tray model with tires (Jalappa, 2015).

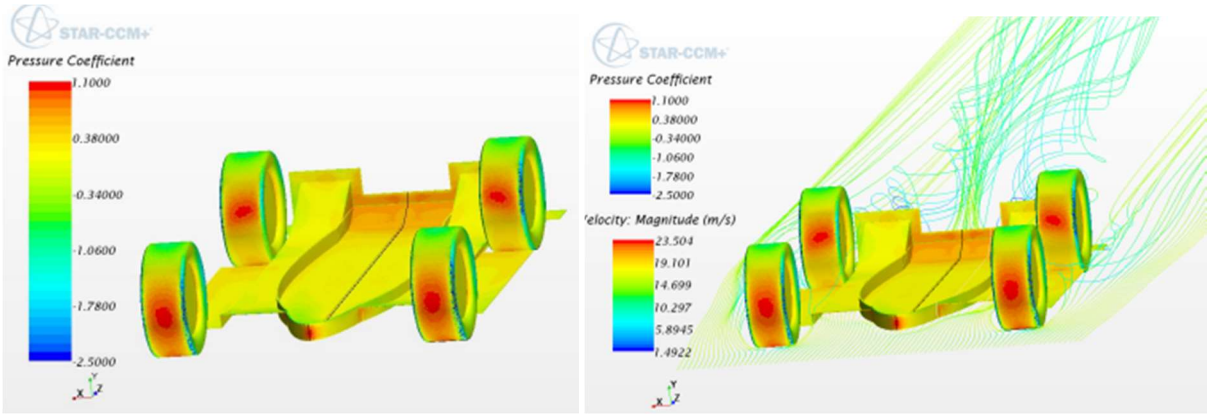

Figure 47: Visual of air flow simulation of under-tray model with tires (Jalappa, 2015).

In the final results, the improvements that were made throughout this study were noticeable. These results were produced with a speed of 30 *m/s* (***Figure 47***). Through the 3-D analysis, a 33% increase of downforce was made possible and the gurney flap increased the downforce also by 50% (***Figure 48***). With the second diffuser and gurney flap was a 23% increase of the C_l.

Under tray type	Down-force(LBF)
Old under-tray free stream (2006)	93
Under-tray w/o gurney	120
Under-tray with gurney	146
Under-tray w/o gurney rotating tires	73
Under-tray with gurney rotating tires	84
Under-tray in 2 degree pitch	115

Figure 48: Final results of under tray types in accordance with downforce (Jalappa, 2015).

The ride height of the under tray also influenced the downforce generated, since there was a 10% drop of downforce with a reduction of height by only 0.75in (Jalappa, 2015).

In the study of (Doddegowda, 2006) the simulation starts with the experimentation with various types of meshes and turbulence models for a single element wing (***Figure 49***).

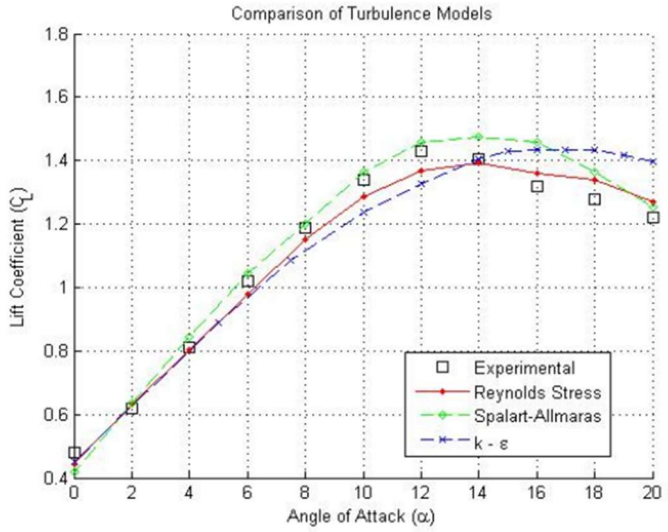

Figure 49: Lift Coefficient-Angle of attack graph (Doddegowda, 2006).

After the decision of which process of design to follow for the single element wing (***Figure 50***), the study continued on the multi element wing.

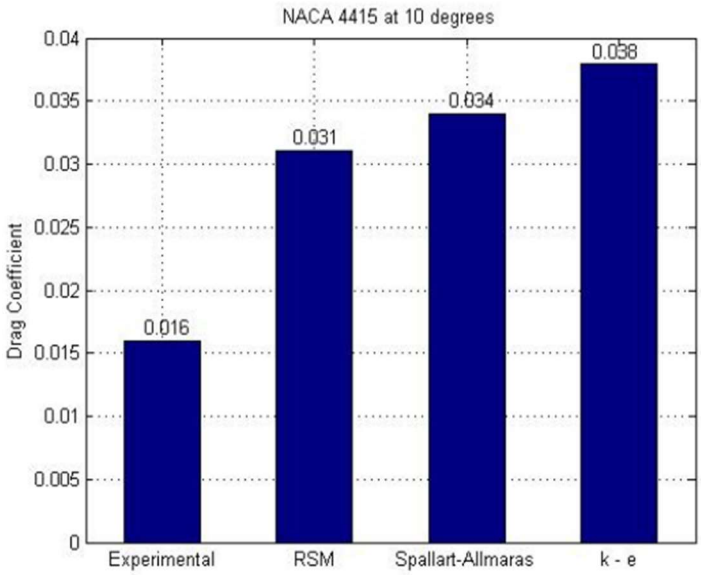

Figure 50: Drag Coefficient compared to experimental values (Doddegowda, 2006).

The purpose of a wing is the downforce generation but this comes also with a higher drag, which is important to the car acceleration. With the acceptable drawbacks, a 4-element wing was chosen and the simulation results for C_l and C_d are presented in ***Figure 51***.

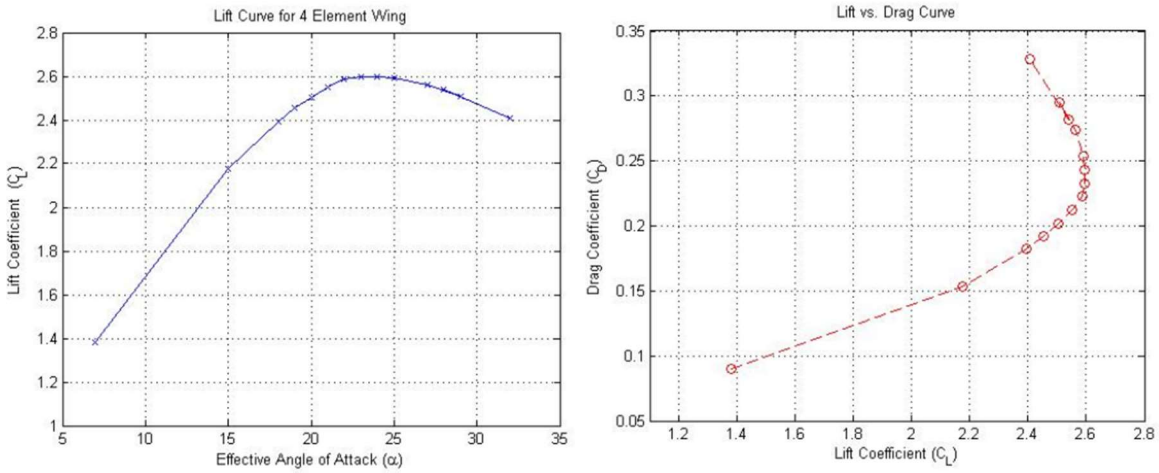

Figure 51: Lift Coefficient-Effective angle of attack and Drag coefficient- Lift Coefficient graphs (Doddegowda, 2006).

A wind tunnel experiment took place, so the simulation results could be validated. The experiments with the 1:2 wing model were at the set speed of 35 *mph* and the set angle was 22° (***Figure 52***).

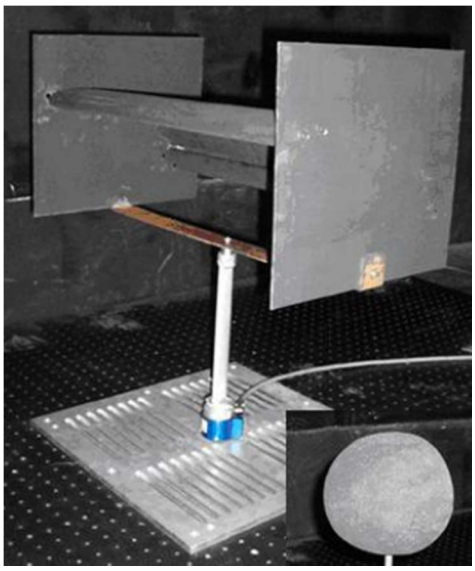

Figure 52: 1/2 model of the four-element wing in the wind tunnel (Doddegowda, 2006).

With the comparison of the numerical with the experimental results it's clear that they have a 10% difference on C_l (***Figure 53***). However, the numerical results of the C_d didn't compare well with the experimental ones. The reason was the overestimation of the turbulence.

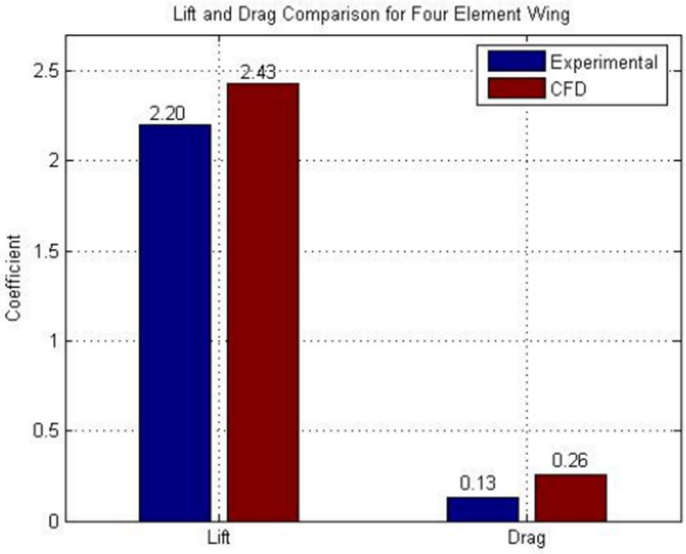

Figure 53: Lift and Drag comparison with experimental and CFD results (Doddegowda, 2006).

The front wing was designed in such a way that the first elements were blowing air towards the high camber element which could produce a high lift coefficient (***Figure 54***).

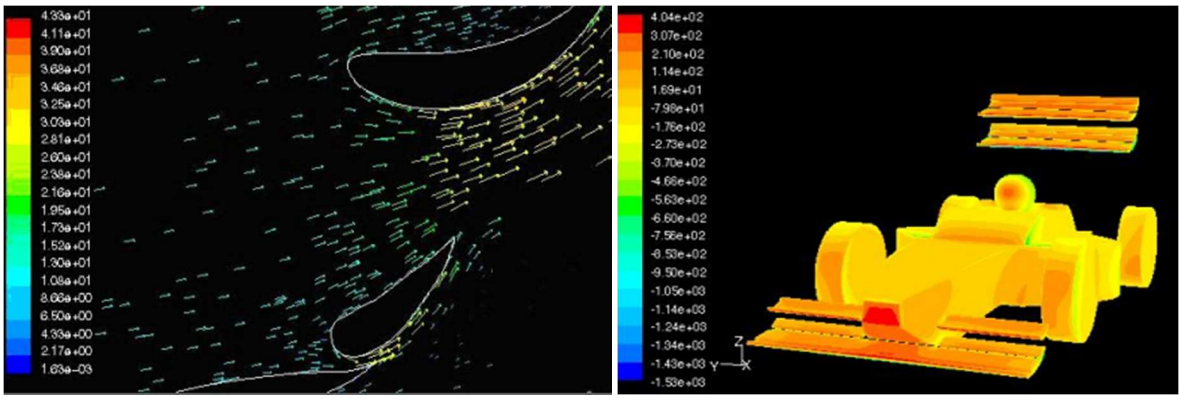

Figure 54: Visualization of the velocity at the front wing and surface pressure of a simplified full car model (Doddegowda, 2006).

The rear wing was designed as an eight-element wing and it could produce high downforce. As a result, it improved the lap time of the race car (Doddegowda, 2006).

The next study (Dharmawan, 2018) simulated the car in set speeds of 60, 80, 100, 120, and 140 *m/s*. Different models were simulated in those speeds for the purpose of studying the amount of drag force in the vehicle with the wings installed. The first model had no front and rear wings, for the purpose of studying the aerodynamic parameters without them (***Figure 55***).

Figure 55: Car model without the front and rear wings (Dharmawan, 2018).

The second model had the front and rear wings attached to it, so the drag force produced can be computed (***Figure 56***).

Figure 56: Car model with the wings (Dharmawan, 2018).

The goal of a three paired airfoil and endplate front wing was to separate the airflow in two directions. The different sections that the wing was divided were made so they can divert the air flow to the side pods and around the front wheels (***Figure 57***).

Figure 57: Front wing (Dharmawan, 2018).

The aim of a diffuser is to decrease the turbulent flow under the car and create a flow so it can decrease the lift. This diffusers base was designed with a nozzle shape so it can increase the downforce produced and to have low pressure at the exit so the car has better grip (***Figure 58***).

Figure 58: Diffuser (Dharmawan, 2018).

The model of the rear wing was designed so it could increase the downforce and make the rear wheels have more grip. It had two airfoils inside; one downside and they flanked the two endplates (***Figure 59***).

Figure 59: Rear wing (Dharmawan, 2018).

The results showed that the car with aerodynamic additions performs better than the one without (***Figure 60***).

Cd	Velocity (km/h)	Drag Force (N)
0.72	60	115.842
0.73	80	204.504
0.73	100	323.017
0.73	120	464.175
0.73	140	600.134

Cd	Velocity (km/h)	Drag Force (N)
0.55	60	156.399
0.55	80	225.638
0.56	100	335.955
0.56	120	448.924
0.57	140	624.401

Figure 60: Comparison of values with (left) and without (right) aerodynamic attachments (Dharmawan, 2018).

More specifically, the car without the wings and the diffuser has a higher drag force with a C_d value of 0.73. The aerodynamic additions on the other model decrease the drag force with a C_d

value of 0.53, meaning that it had a 23% reduction. This shows the importance of the correct aerodynamic design (Dharmawan, 2018).

2.2 Structural analyses

In the next paragraphs we will continue with some studies of structural analyses of the chassis of various Formula Student/SAE cars, which consist of static structural analysis, torsional analysis, bending analysis, and modal analysis. The torsional analysis sections of these studies will be presented as a reference for the following torsional analysis of our chassis. In almost all the fooling studies the construction material that was used was the Chromyl Steel or AISI4130.

The torsional analysis of (Chikkali & Patil, 2020) was centered around the torsional stiffness of the chassis, meaning how much the chassis could withstand twisting forces. This was important for the turning and cornering ability of the car. A force of 3000N was applied on the front right-side suspension and the same force with opposite direction and the front left side suspension while the rear suspension was fixed (***Figure 61***).

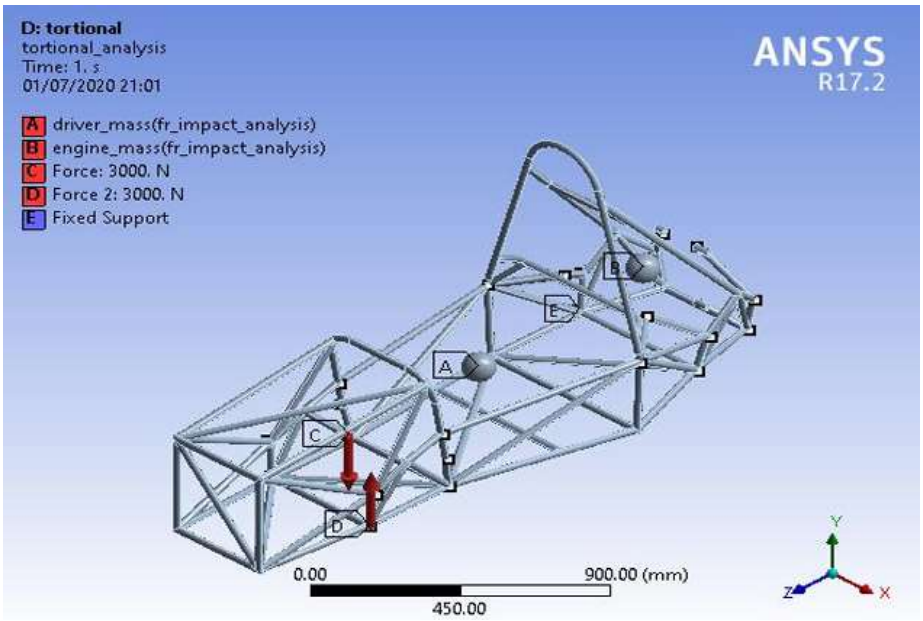

Figure 61: Boundary conditions of the analysis (Chikkali & Patil, 2020).

The calculation of the Von Misses stress gave results of a maximum stress 274.24 *MPa* and max deformation 10.924 mm (***Figure 62***).

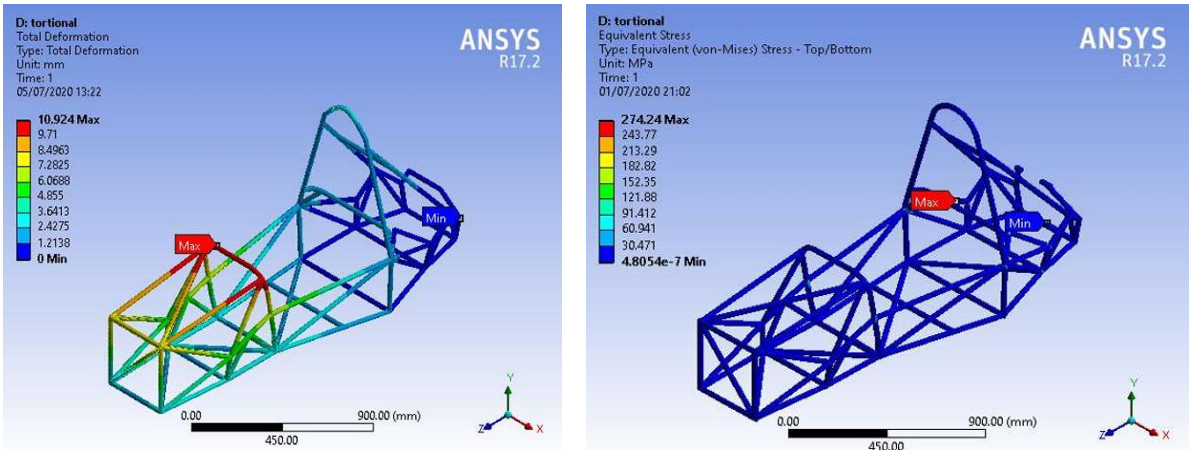

Figure 62: Visualization of the Torsional Deformation analysis and the Von Mises Stress (Chikkali & Patil, 2020).

The analysis was done in the environment of ANSYS 17.2 software (Chikkali & Patil, 2020).

In the study of (Ghosh, et al., 2018), the chassis was studied in two sections, the front and then the rear one. Starting from the front section, a force of 3673.2 N was applied upward on the suspension of one side and an equal downward force on the suspension of the other side (***Figure 63***). The forces were always applied on the 4 nodes of the suspensions. The maximum stress was 3.66549e+008 *N/m^2* (366,549 *MPa*) and the maximum deformation was 23.6564 mm (***Figure 64***).

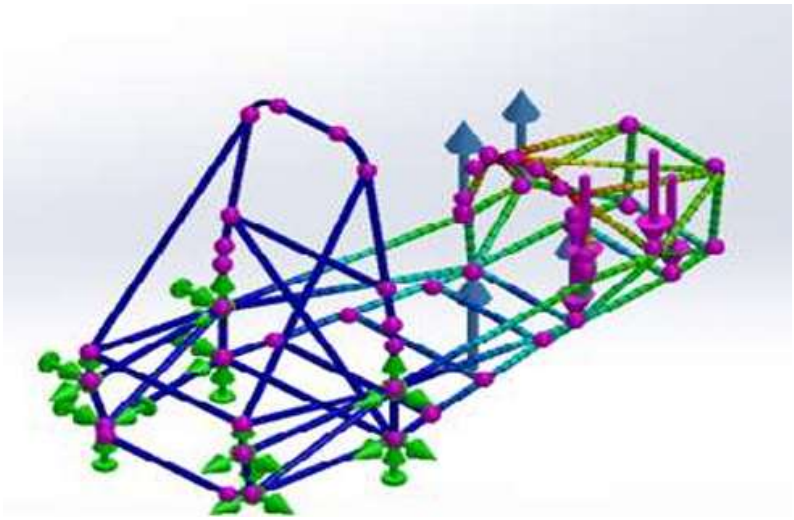

Figure 63: Boundary conditions of the Front Torsional analysis (Ghosh, et al., 2018).

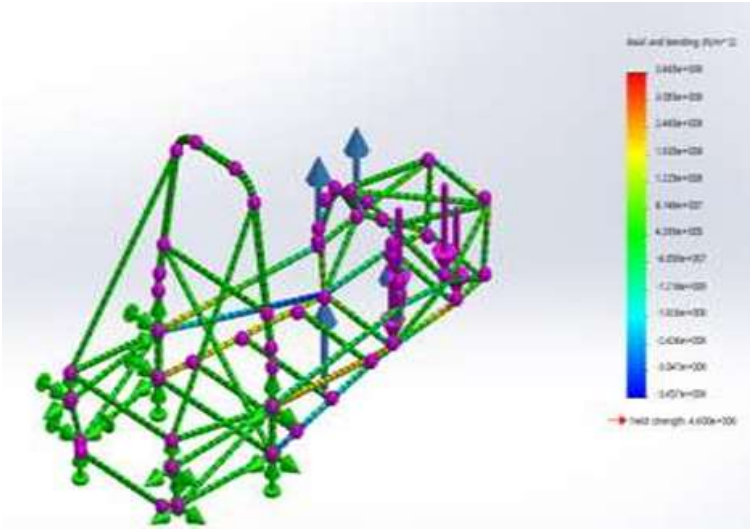

Figure 64: Visual of the generated stress in Front Torsional analysis (Ghosh, et al., 2018).

Continuing to the rear section, a force of 6545 N was applied upward on the suspension of one side and an equal downward force on the suspension of the other side (***Figure 65***). The maximum stress was 3.72938+008 *N/m^2* (372,938 *MPa*) and the maximum deformation was 32.3287mm (***Figure 66***).

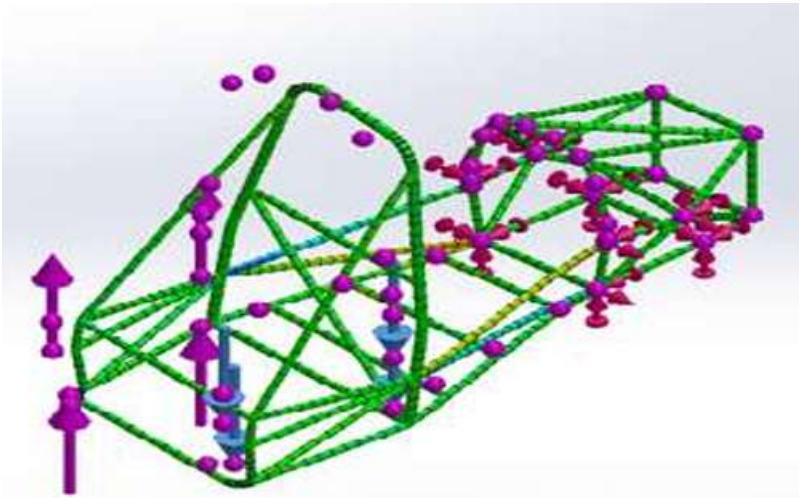

Figure 65: Boundary conditions of the Rear Torsional analysis (Ghosh, et al., 2018).

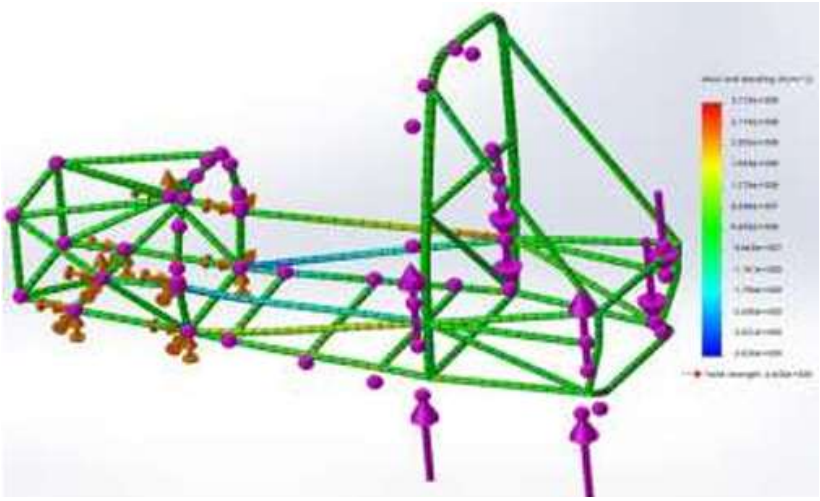

Figure 66: Visualization of the generated stress for the Rear Torsional analysis (Ghosh, et al., 2018).

The force on the rear section of the chassis was greater because the rear section of the future car would be heavier than the front one, with all the equipment mounted on it. The analysis was done in the environment of SOLIDWORKS software (Ghosh, et al., 2018).

In the study of (Shukla, et al., 2016) the mesh that was used for the analysis of the chassis in CATIA V5, consisted of linear tetrahedral elements. The rear section of the chassis was fixed and the rest of the structure was bent clockwise along the x-axis with a moment of 360 *N-m* applied to it (***Figure 67***).

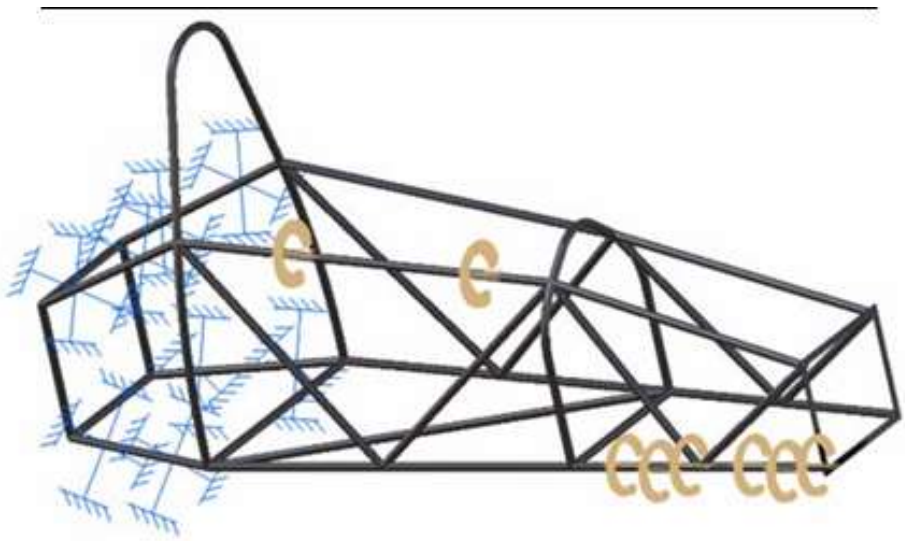

Figure 67: Boundary conditions for the test of (Shukla, et al., 2016).

The torsional analysis gave results of maximum Von Mises Stress equal to 26.6 *MPa* and maximum deformation of 0.347mm (***Figure 68***) (Shukla, et al., 2016).

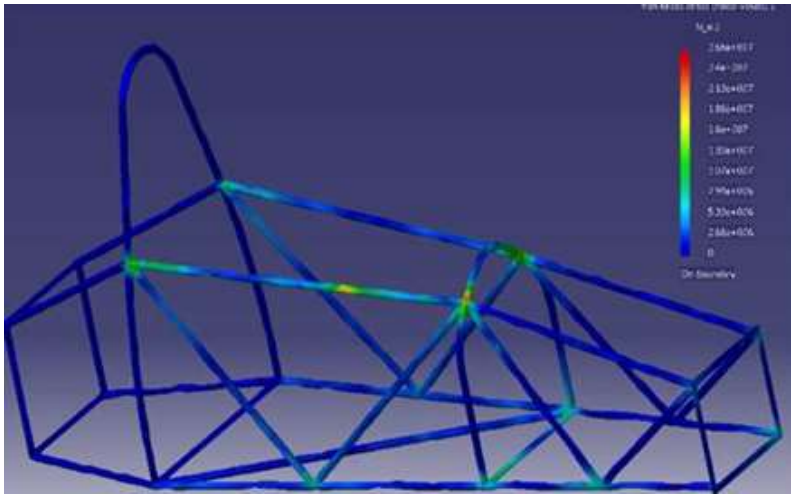

Figure 68: Visual of Von Mises stress results (Shukla, et al., 2016).

The torsional analysis in the study of (Putsala, et al., 2022) was performed in a way that simulated the chassis' front wheels fell into a dump. That meant that a load of 2000 N applied in the lower pick-up nodes in each side of the chassis.

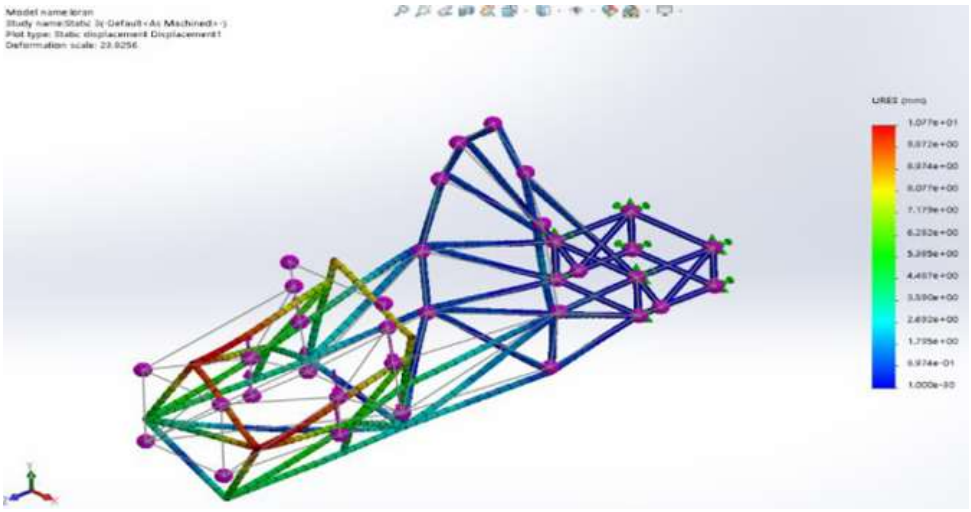

Figure 69: Visualization of the Displacement of the chassis (Putsala, et al., 2022).

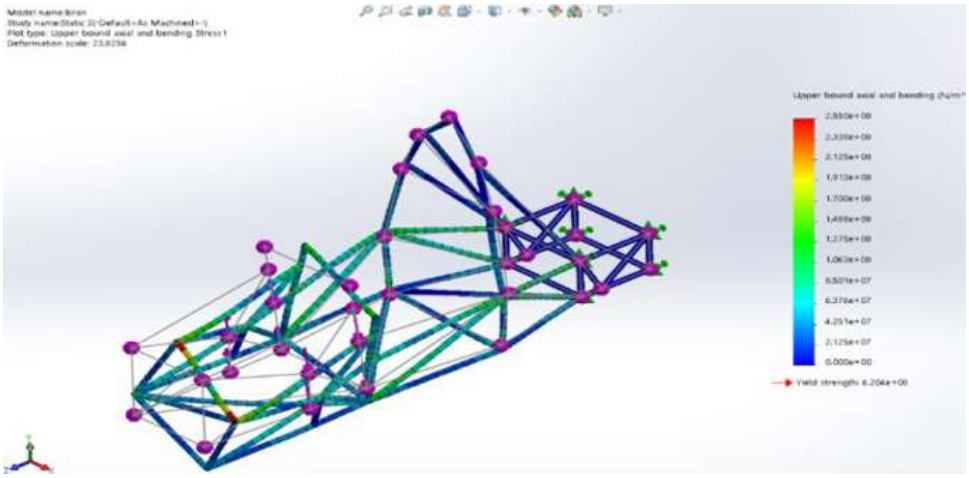

Figure 70: Visualization of the Von Mises stress results (Putsala, et al., 2022).

The analysis results gave a maximum Von Mises Stress of 250 *MPa* (***Figure 69***) and a displacement of 10.77mm (***Figure 70***) (Putsala, et al., 2022).

The mechanical properties of the chassis construction material in the next study of (Singh, 2010) are described in ***Figure 71*** corresponding to steel alloy IS 3074.

STEEL GRADE: IS 3074		
S.No.	**Properties**	**Values**
1	Young's modulus	2e+011 N/m^2
2	Poisson ratio	0.266
3	Density	7860 kg/m^3
4	Yield Strength	3.73e+008 N/m^2

Figure 71: Mechanical Properties of the chassis material (Singh, 2010).

The elements used for meshing were Linear Tetrahedral ones and the software tool that was used for the design and the finite element analysis (FEA) was the CATIA V5. For the static torsional loading the rear suspensions were clamped and the front bulkhead side was subjected to a clockwise moment of torque across the X-axis of 316 *N-m* (***Figure 72***).

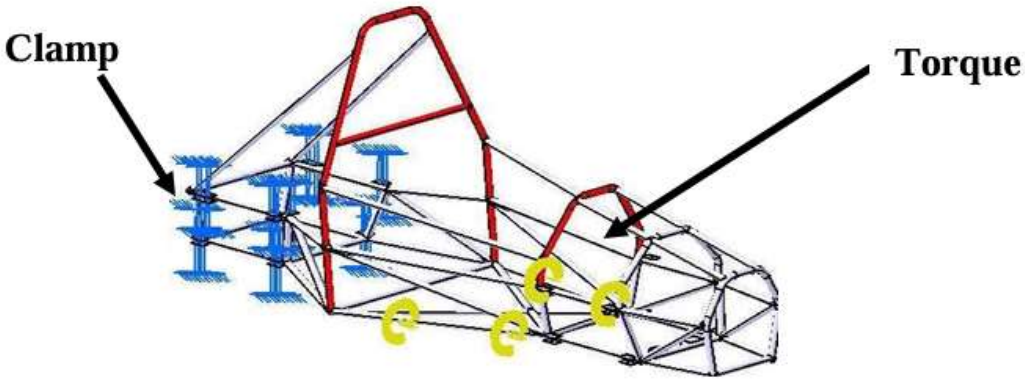

Figure 72: Boundary conditions of the test (Singh, 2010).

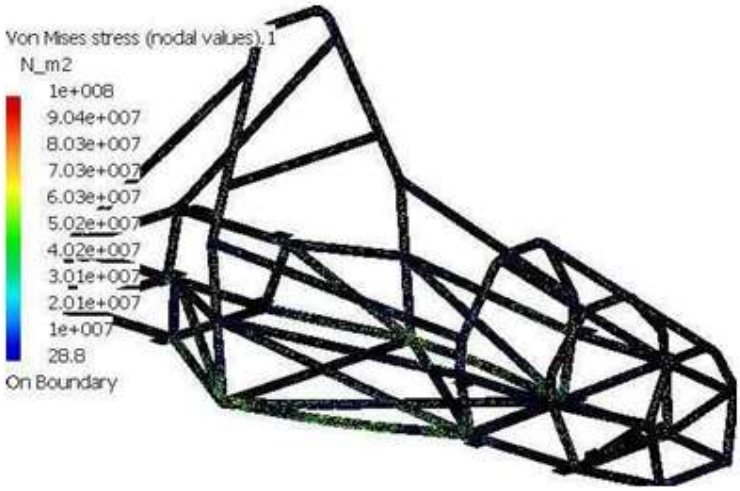

Figure 73: Visualization of the Von Mises stress results (Singh, 2010).

The Von Mises results gave an overall stress of 5.02x10^7 *N/m^2* (50.2 *MPa*) with a maximum stress of 1e+008 *N/m^2* (***Figure 73***) and a maximum deformation of 2.24 mm in the bulkhead support and the lower side impact members (Singh, 2010).

For the finite element analysis of the chassis in the study of (Pathak , 2020), a linear tetrahedral elements of 5 mm size were used. The chassis was clamped diagonally opposite rear suspension mounts and a force of 8240 N was applied on diagonally opposite front suspension mounts.

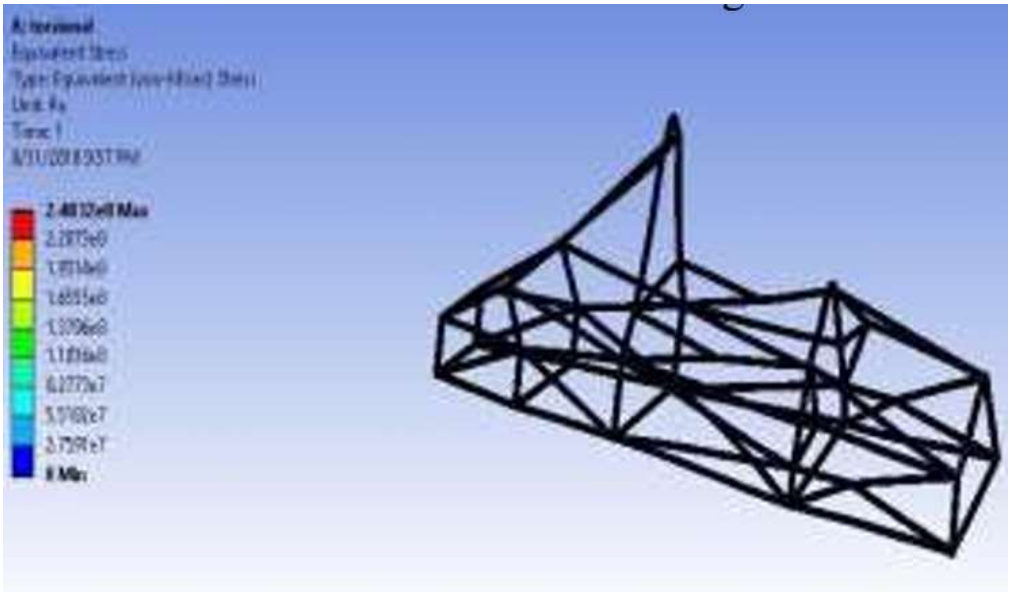

Figure 74: Visualization of the Von Mises stress results (Pathak , 2020).

The maximum Von Mises Stress was equal to 2.4817e8 *N/m^2* (248.17 *MPa*) (***Figure 74***) and the maximum displacement on suspension points in vertical Y-axis was 1.56 mm (Pathak , 2020).

3. Design of the Chassis

CATIA V5R20 software, developed by Dassault Systèmes, is widely used in Computer-Aided Design (CAD) and Computer-Aided Engineering (CAE). It is well known for its applications in 3D design, as well as for the simulations and analyses of complex engineering systems, such as aircrafts, ships, cars, industrial machinery, and consumer goods. It offers 3D modeling features, 2D drafting tools and a wide range of engineering analyses tools. This design software offers advanced features so the users can create highly detailed and precise models. In this case, CATIA was chosen for its parametric and surfacing capabilities, which provide the ability to parametrically model complicated geometries. The parametric design was used so the various dimensions can be controlled freely by set parameters, without redesigning the same parts when a change was needed.

The tools that were used in this study were:

- Generative Surface Design Workbench (the tool where the newly measured chassis was modelled) (***Figure 75***).
- Analysis & Simulation (the tool where the torsional analysis was performed) (***Figure 104***).

3.1 Measurement of the physical chassis

After the construction of the chassis of the FSTUC racing car, several expected deviations from the initial 3D geometrical model were observed, due to the construction procedures that had been used. The main errors are connected with the cutting, forming and welding the cylindrical steel rods, which were used as the construction material of the chassis. Additional errors were attributed to the imperfections of the aluminum jig that was used for the construction of the chassis, as well as errors during the measuring of the different parts of the chassis. It is also important to consider the imperfect stability and anchoring of the physical clamps that linked the various parts with the jig. Additionally, the high temperatures, taking place during the welding of the metallic parts of the chassis, caused additional imperfections to the final dimensions of the chassis (due to the corresponding thermal stresses).

In order to have an accurate 3D geometrical model of the final chassis, after its construction it was measured as precisely as possible with the available measurement instruments and devices. With the new measurements in hand, a new 3D geometrical model of the chassis was designed using Catia V5. The details of the design procedure are described in the following paragraphs.

Figure 75: Genetative Shape Design workbench of CATIA V5.

3.2 Plane definition

Starting with the design of the chassis, the chassis was divided into sections, and the planes were defined accordingly. At the center of the axis system were the three original planes, the Ground plane (xy plane) which defined the ground level of the design and the starting point of the dimensions, the Main Hoop plane (yz plane), which defines the plane where the main hoop of the chassis would be placed, and it was the starting point of most of the front and rear side planes. The zx plane, which had the role of the symmetry plane, although the chassis was not perfectly symmetrical. Parallel to the Ground plane 55mm up, the Lowest Point plane was defined and, as the name suggests, it was the closest to the ground point of the chassis; at the same point, defined in an angle of 85-degrees, the Firewall plane was the support of the Main Hoop sketch. Parallel to that, at a distance of 155mm from the ground, the Floor plane was defined, which corresponds to the floor level of the chassis. Then, at a distance of 345 mm the Side Impact plane defined the height of the external frame of the chassis. The front side of the chassis was defined with two planes, the Front Hoop plane, at a distance of 810 mm, and the Front Bulkhead plane, at a distance of 1555 mm from the starting point. The rear side was defined with three planes, the Rear Planes 1 & 2, and the Rear Wheel Center plane. The Rear Plane 1 was at a distance of 610 mm, being the start of the backend side of the chassis. At 277 mm from Rear Plane 1, was defined the Rear Plane 2, being the end part of the chassis. Between these two planes the Rear Wheel Center plane and the Rear Suspension plane were defined, where the back wheels will be placed (***Figures 76-78***).

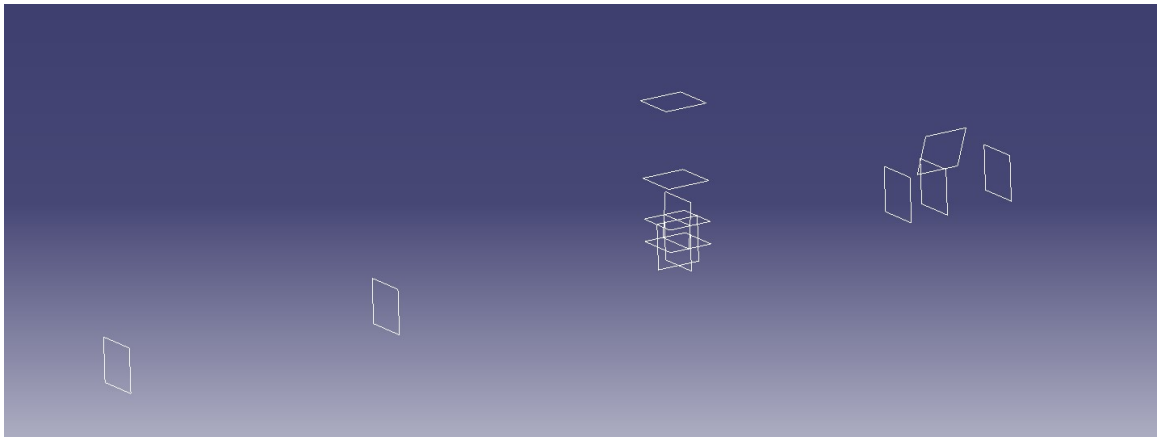

Figure 76: Planes used for the 3D geometry definition.

Figure 77: List of the planes used for the 3D geometry definition.

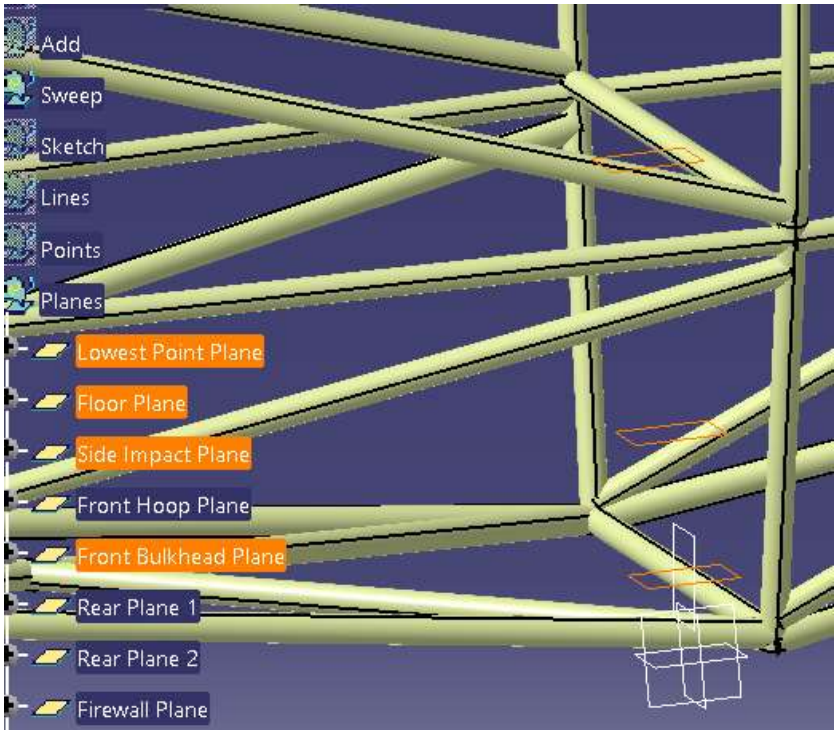

Figure 78: Planes used for the different vertical levels.

3.3 Wireframe definition

After the plane definition, a wireframe was constructed from points and connecting lines, all arranged in the space in regard to the new measurements of the chassis (***Figure 79***). The placement of the points and the actual dimensions of the chassis were not, in fact, completely symmetrical, as it was supposed to be according to the original geometrical model.

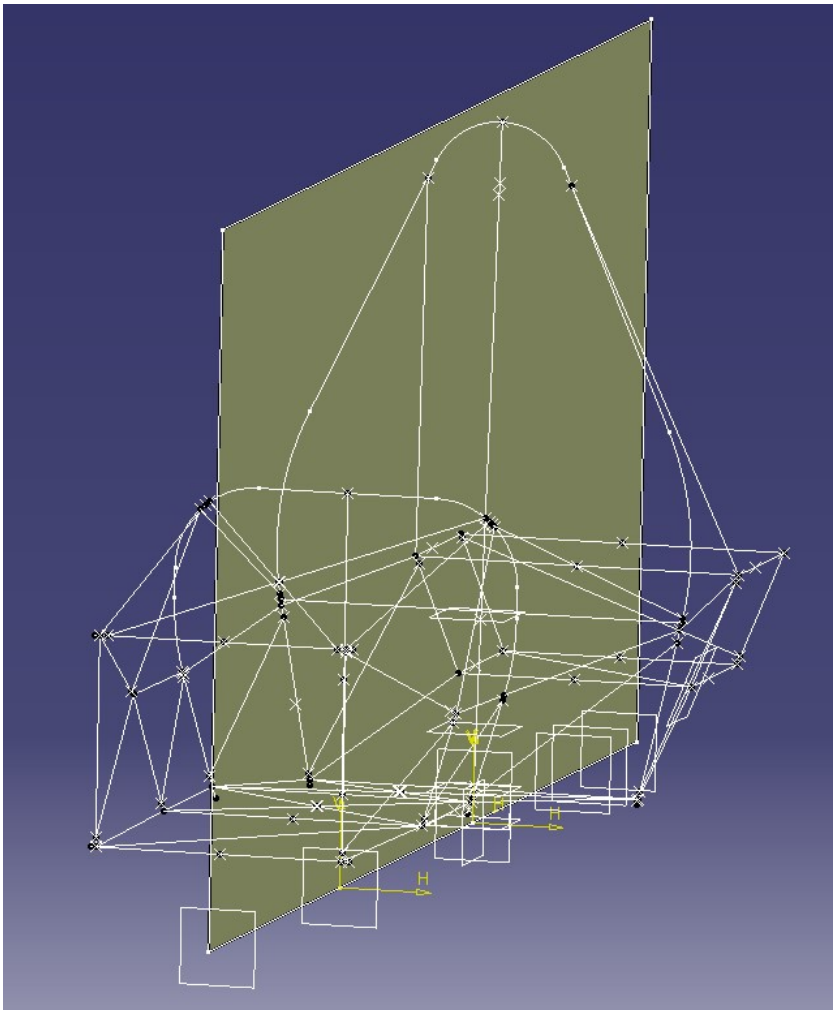

Figure 79: Symmetrical surface.

The main differences between the 3D original geometrical model and the physical vehicle frame were on the max width and the max length of the chassis. The width of the 3D original model was 710 mm and the length was 2560 mm. The width of the physical chassis was 704 mm and the length was 2.500 mm. The front part of chassis was the front bulkhead, along with the area where the driver's pedals were positioned (***Figure 80***).

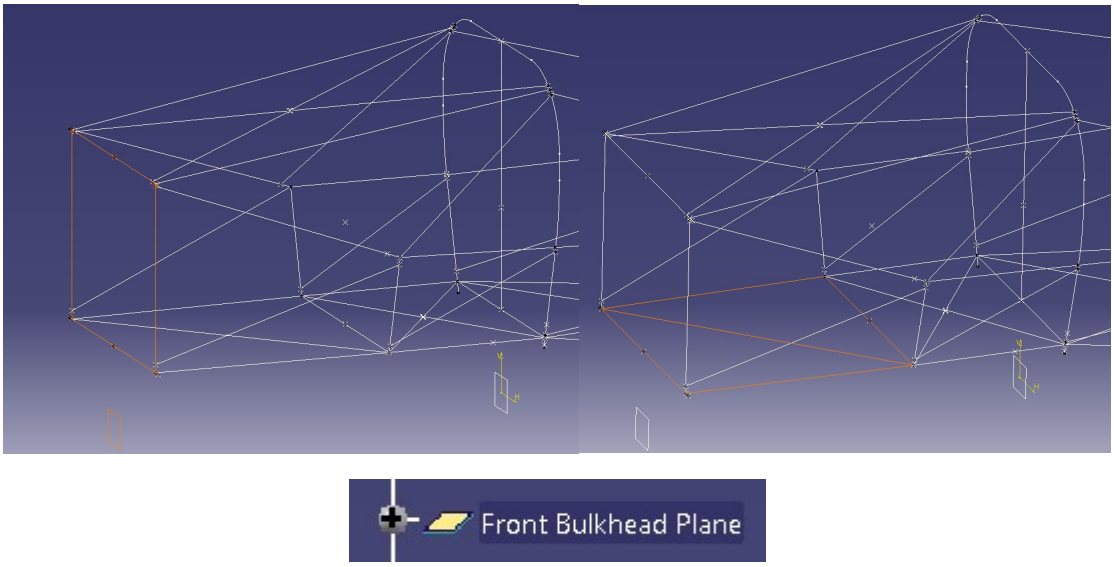

Figure 80: Front Bulkhead wireframe area and the related plane.

The front suspension area (***Figure 81***) was the part of the chassis where the front suspension system of the chassis would be designed. The wheels, the shock absorbers, the control arms, the tie rods would be placed around this area.

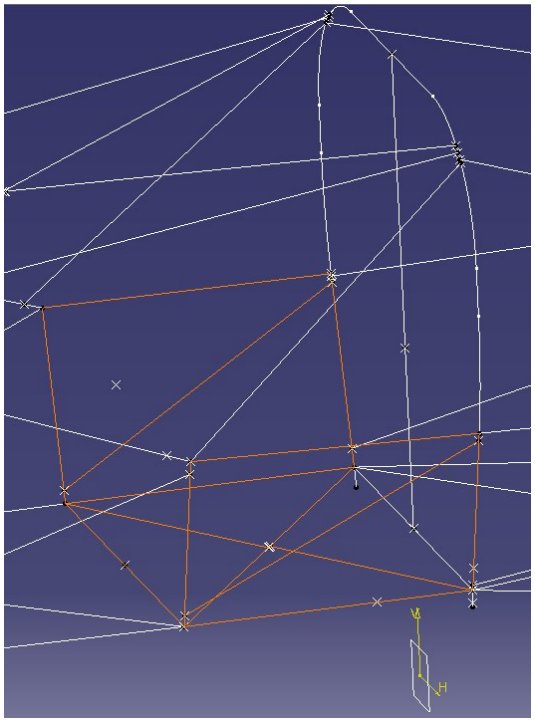

Figure 81: The front suspension wireframe area.

The front hoop area was designed using the Sketch option, due to the complexity of the dimensions and the difficulty of creating the correct tangent circles (***Figure 82***).

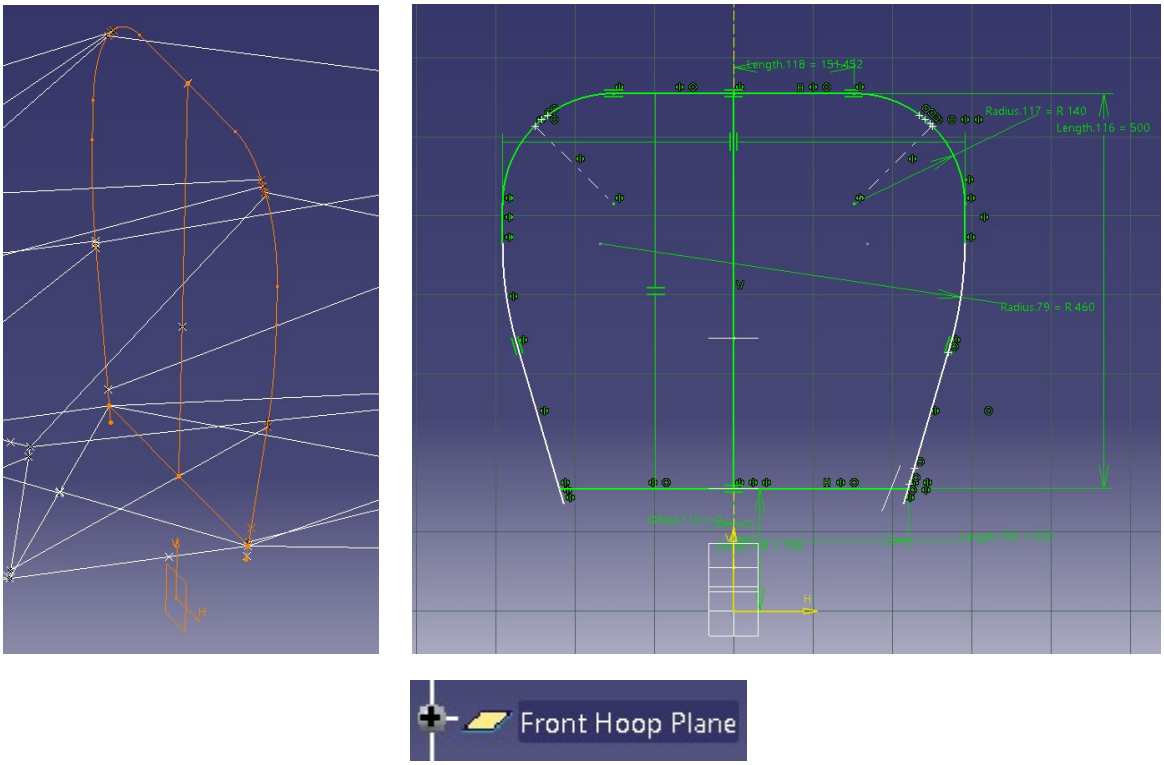

Figure 82: The front Hoop wireframe and the related plane.

The Main hoop (***Figure 83***) was also designed using the Sketch option, for the same reasons as the Front Hoop. It was the area where the driver's and seat would be placed along with the firewall.

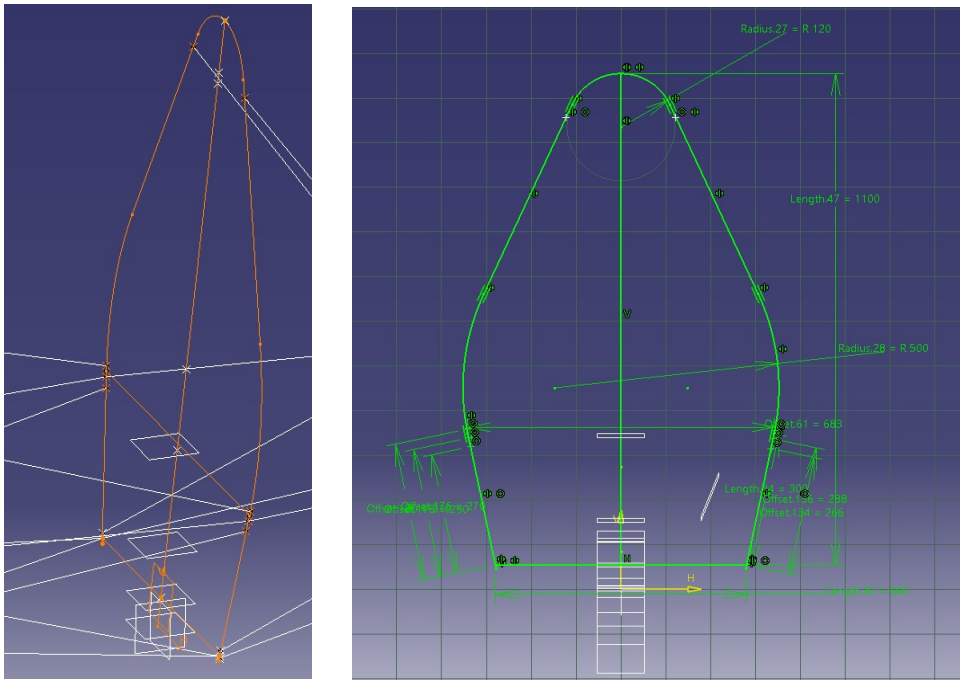

Figure 83: The Main Hoop wireframe and the related plane.

On the main hoop, at the back of the driver's seat, the firewall will be placed, which protects the driver from the high temperatures of the engine area. The main hoop was also designed using the sketch option. However, in contrast to the front hoop, it was defined in an angled plane. As ***Figure 84*** depicts, the main hoop structure was placed in an 85-degrees angle, starting from the height of the "Lowest Point" plane.

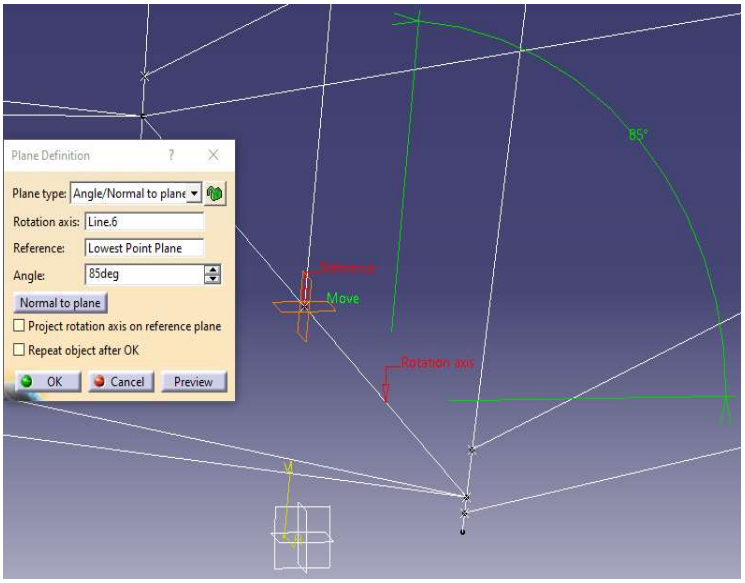

Figure 84: Angled plane of the Main hoop/Firewall.

Part of the Main Hoop was also the shoulder harness mounting bar (***Figure 85***), where the safety belt system of the driver will be installed.

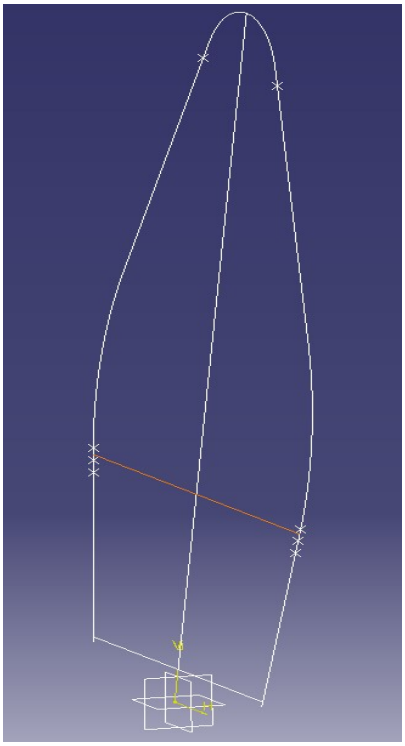

Figure 85: Shoulder harness mounting bar.

Figure 86 depicts the main hoop bracing frames and the engine area. The bracings supports the back of the main hoop and covers most of the upper engine parts. The engine is placed of course behind the firewall, as mentioned before, and most of the weight was distributed at the lower part of the area.

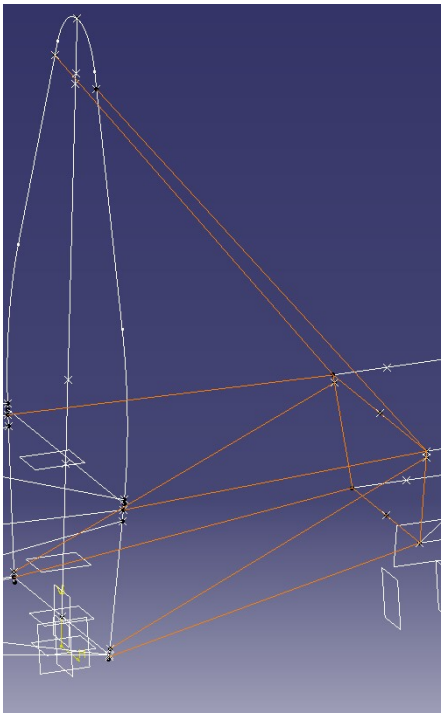

Figure 86: Main hoop bracing frames and engine area.

The rear suspension area would be the designated place of the back suspension system of the racing car (***Figures 87, 88***).

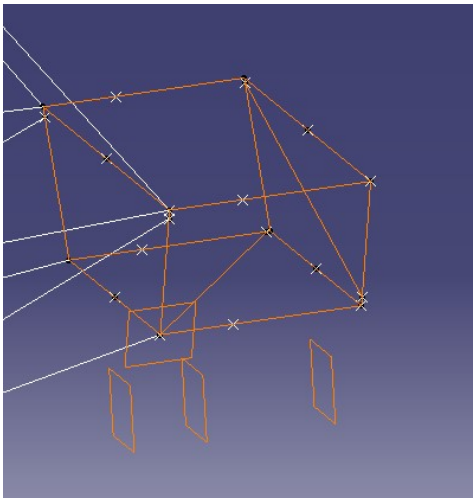

Figure 87: The rear suspension wireframe area and the related planes.

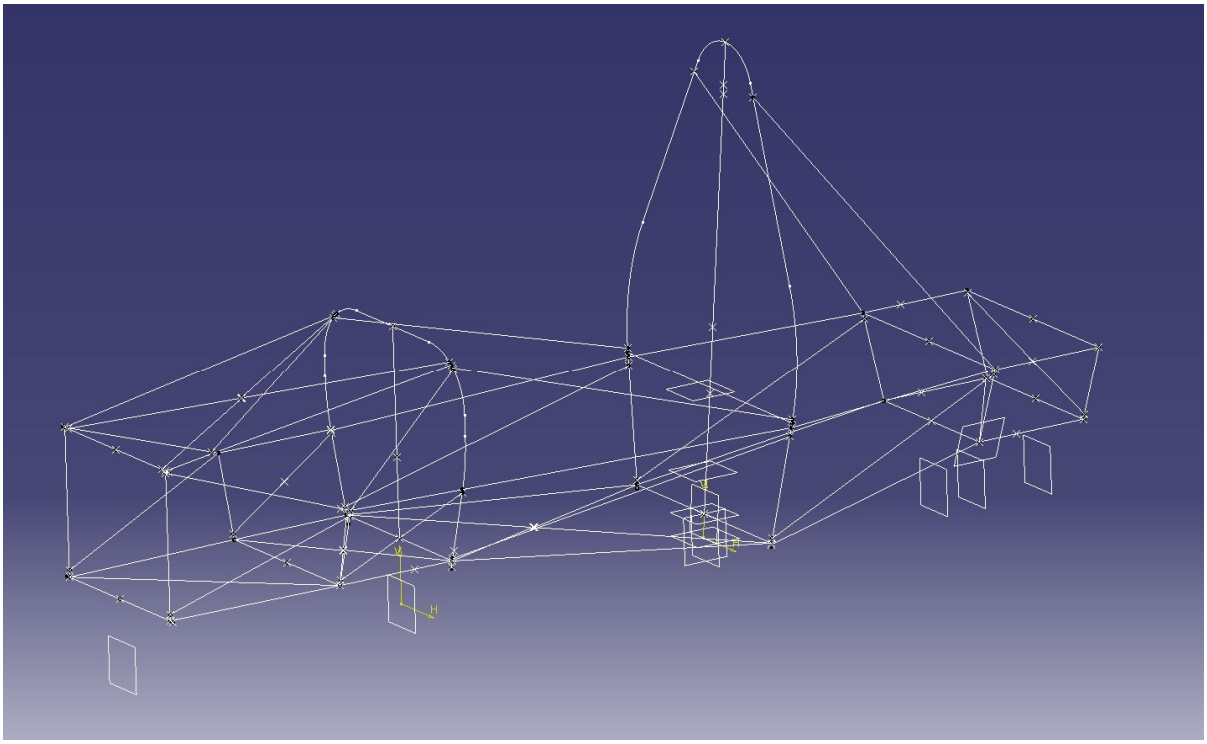

Figure 88: The complete wireframe.

3.4 Design of the tubes

Afterwards, with the use of the "Sweep" tool (***Figures 89, 90***), the surface of a tube-like shape around each line was generated. The boundaries of each surface was the two points at the opposite ends of each connecting line. The dimension was the internal radius of each tube.

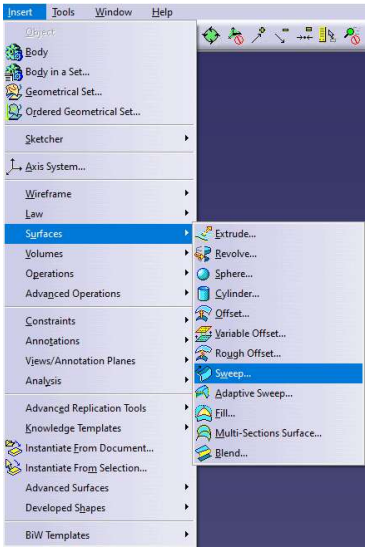

Figure 89: The Sweep tool.

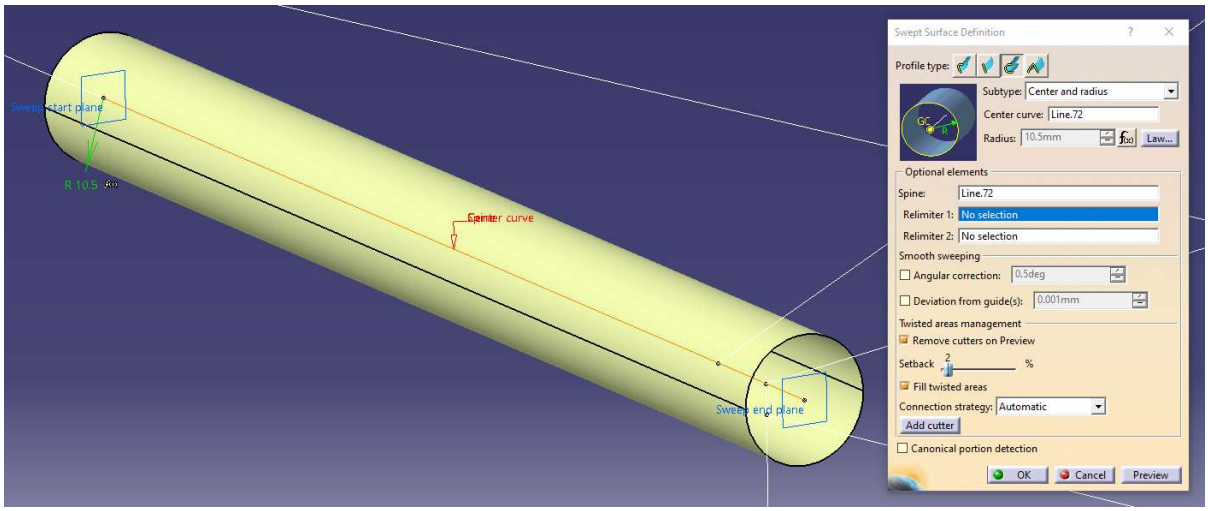

Figure 90: Sweep's use example.

Two diameters were used in this part of the design, one that was equal to 10.5 mm, which was applied in most sections of the chassis and another one equal to 9.9 mm. The second one was used primarily around the driver's area, at the front hoop, at some side impact structures, and at the main hoop, for better durability, ensuring the driver's safety in the case of an accident (***Figure 91***).

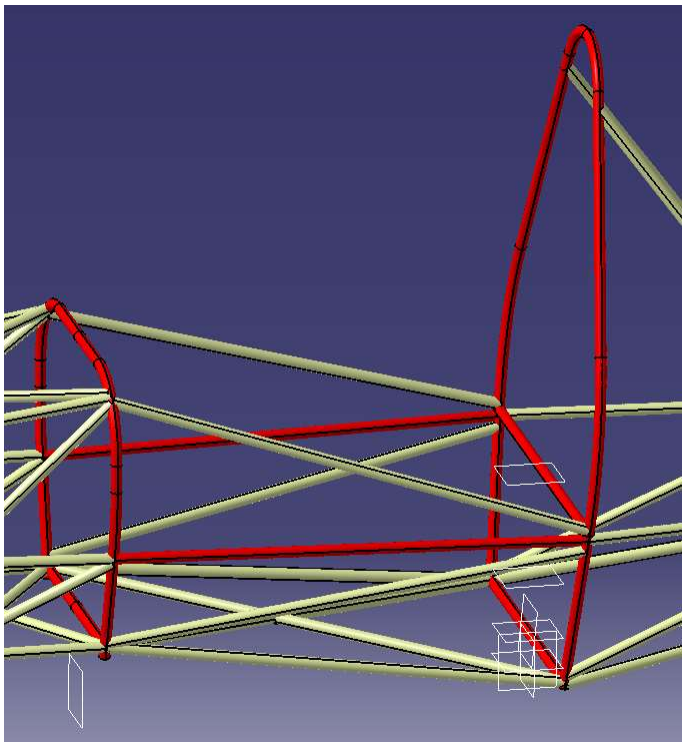

Figure 91: The 9.9 mm radius sections.

In Parametric modeling, the dimensions and features controlled by the user are termed as User parameters, while Formulas represent the relationships between these different geometrical entities and parameters. This type of modeling allowed to control these geometrical entities, such as Radius and Tube Thickness, by simply changing the parameter's value, a procedure that would require time consuming direct manipulation for each individual section of the chassis. As ***Figure 92*** illustrates, the f(x) symbol showed that the 10.5 mm value is linked to a formula. The two types of dimensions that were used in Sweep are depicted in ***Figure 93*** as Radius Internal No1 & No2 and the same is true for the two types of Tube Thickness that will be explained later in this document.

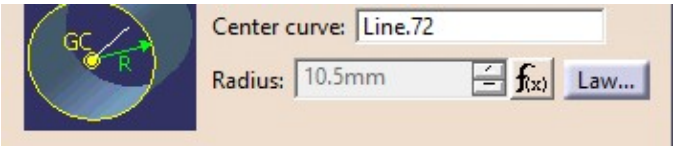

Figure 92: Example of a formula in use.

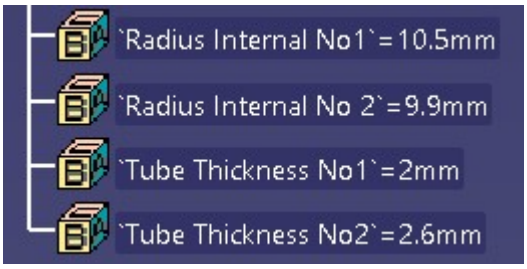

Figure 93: Cylindrical tubes' parameter list.

The resulted design, after the sweep surface engulfed every part of the wireframe, is presented in ***Figure 94***.

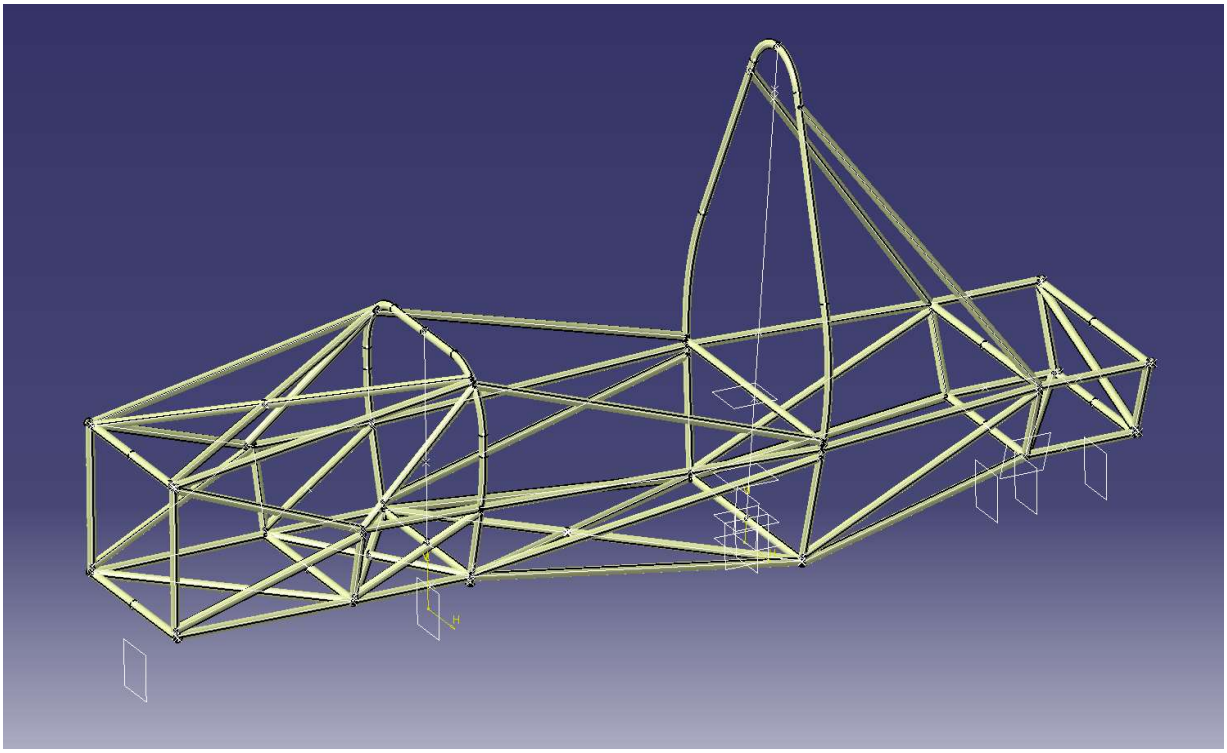

Figure 94: Complete sweep of chassis.

During the design of the tube-like surfaces, due to the wireframe layout, parts of the surfaces intersect, as it appears in ***Figure 95***.

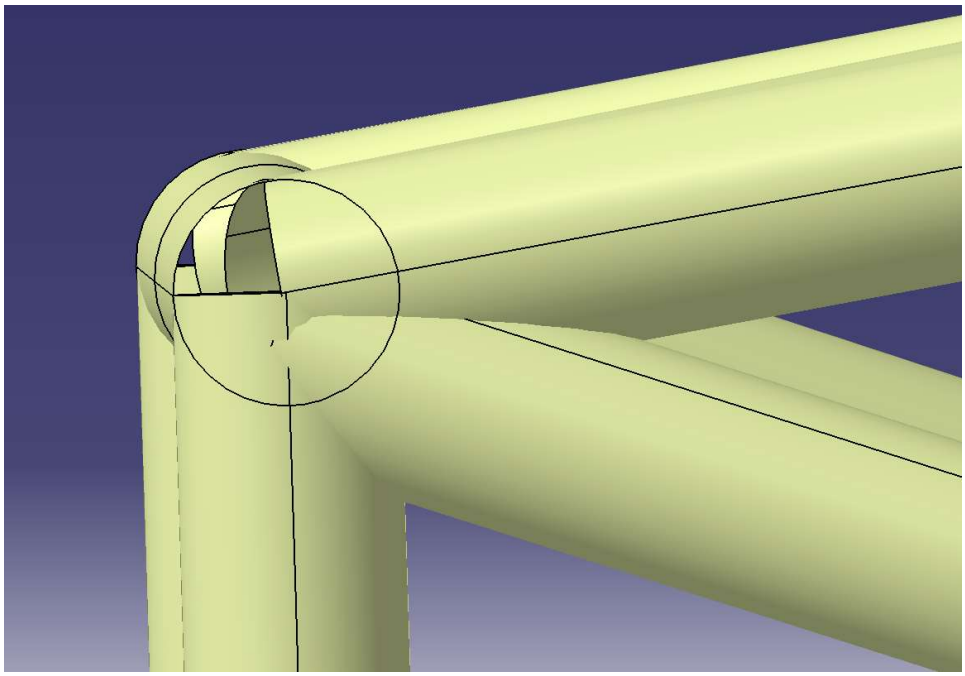

Figure 95: Intersected tube surfaces.

This excess surface requires removal with the use of the "Trim" tool (***Figure 96***). At the physical chassis the cylindrical metal rods were welded to each other, so there was no excess material inside the rods.

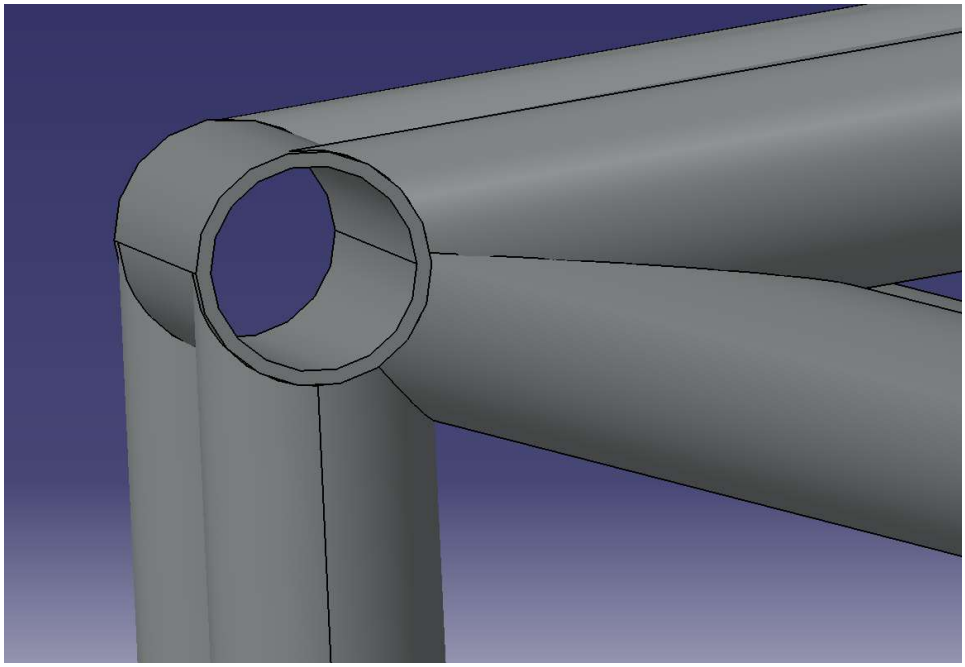

Figure 96: Example of a trimmed area.

Because of the high complexity of the 3D model, there was no trimming of the internal excess surfaces (and volumes) between the tubes and, since this didn't affect the study and the design as a solid, it was not modified.

3.5 Adding Thickness to the Surfaces

The tube surfaces have to be turned into solid tubes. With the use of the "Thick Surface" tool, the cylindrical rods were subsequently generated (***Figure 97***).

With the "Volume" toolbar, designs that previously were only surfaces can be turned into a solid, something with real world properties and qualities, so it can be studied as a solid material. Up to this stage of the study, the main purpose of using this tool is to create the physical dimensions of the chassis.

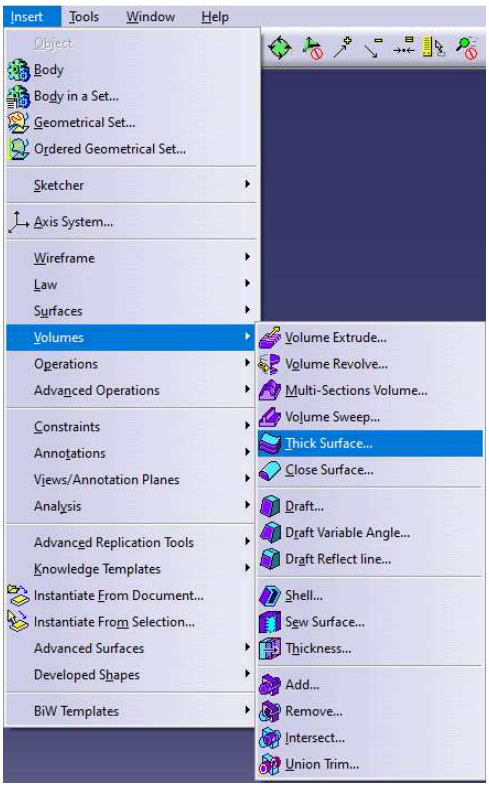

Figure 97: The Thick Surface tool.

Most of the rods have a thickness equal to 2.0 mm (***Figure 98***), while the thicker ones (previously mentioned – placed around the driver's seat) have a thickness equal to 2.6 mm (***Figure 99***). These two options had as a result an external radius of 23 mm and 22.4 mm accordingly.

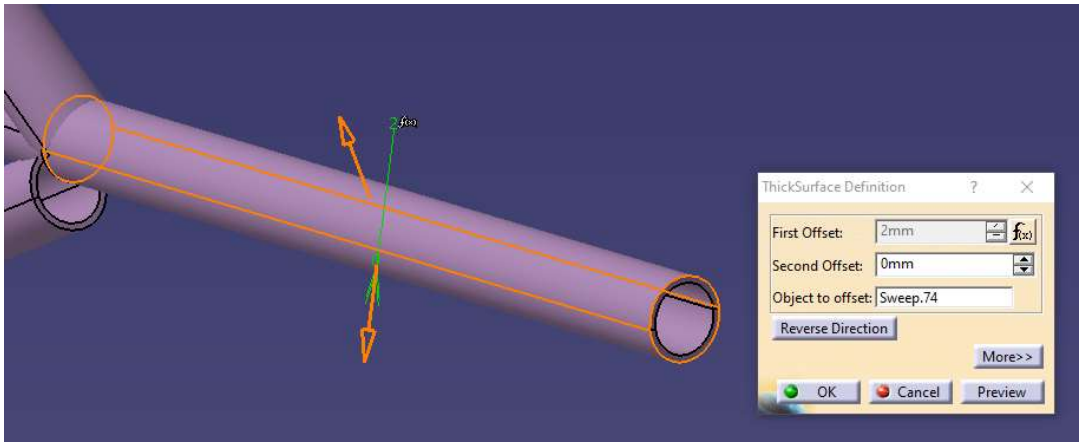

Figure 98: The first type of the Thick Surface example.

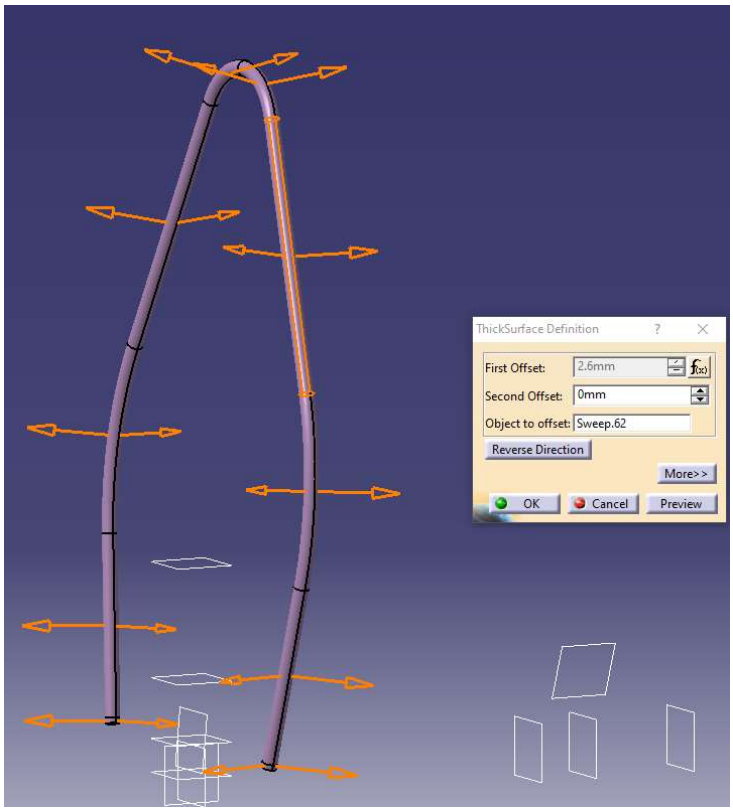

Figure 99: The second type of the Thick Surface example.

The complete design so far, after the Thick Surface tool was applied and engulfed every part of the tube-like surface, is being presented at the ***Figure 100***.

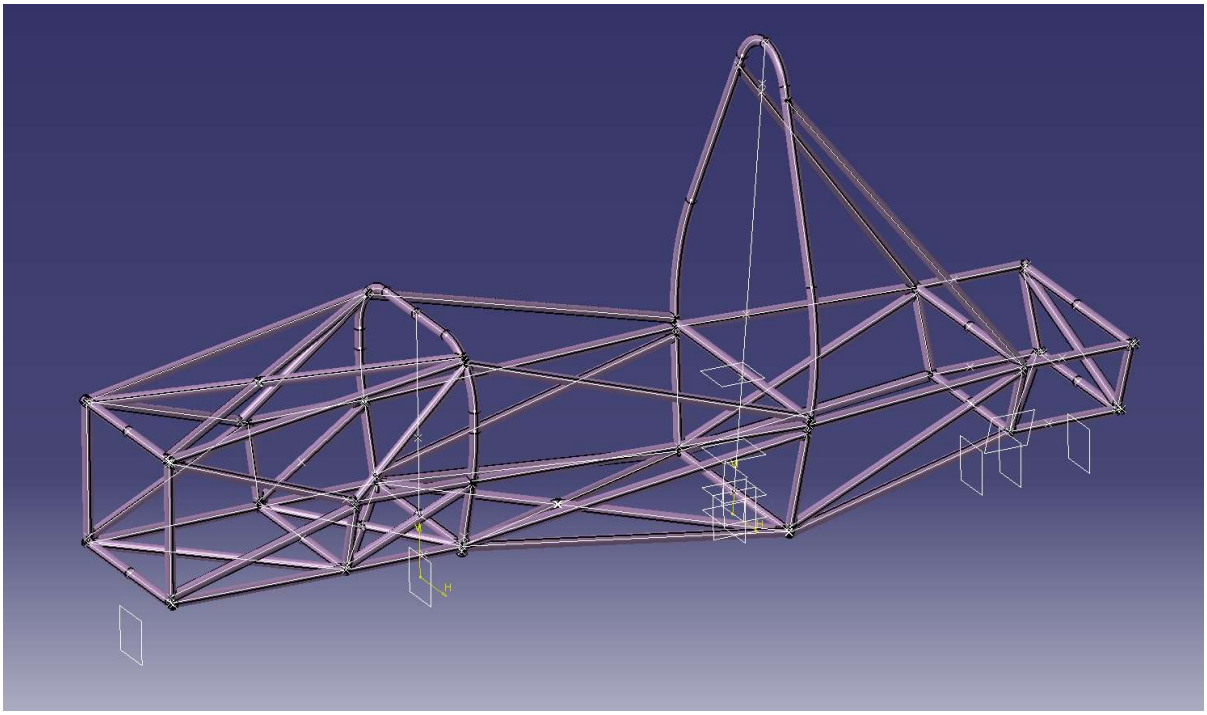

Figure 100: Complete Thick Surface's use of the chassis.

For the better study of the chassis, the 3D model should not have separate parts. With the successive application of the "Add" tool this was achieved (***Figure 101***). The different solid parts of the chassis were defined as a unified solid and this was achieved by adding each individual rod to another, until it was only one entity, as depicted in ***Figure 102***.

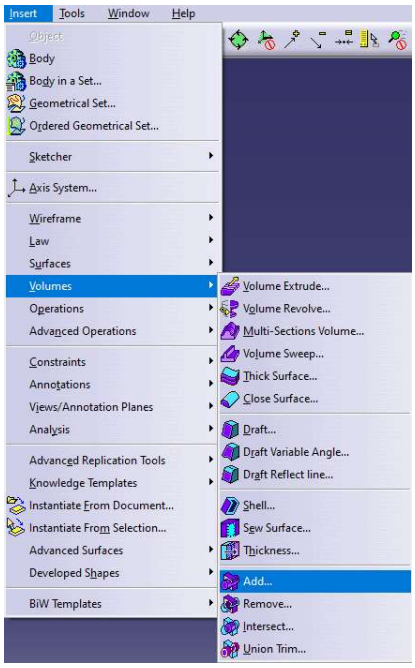

Figure 101: The Add tool.

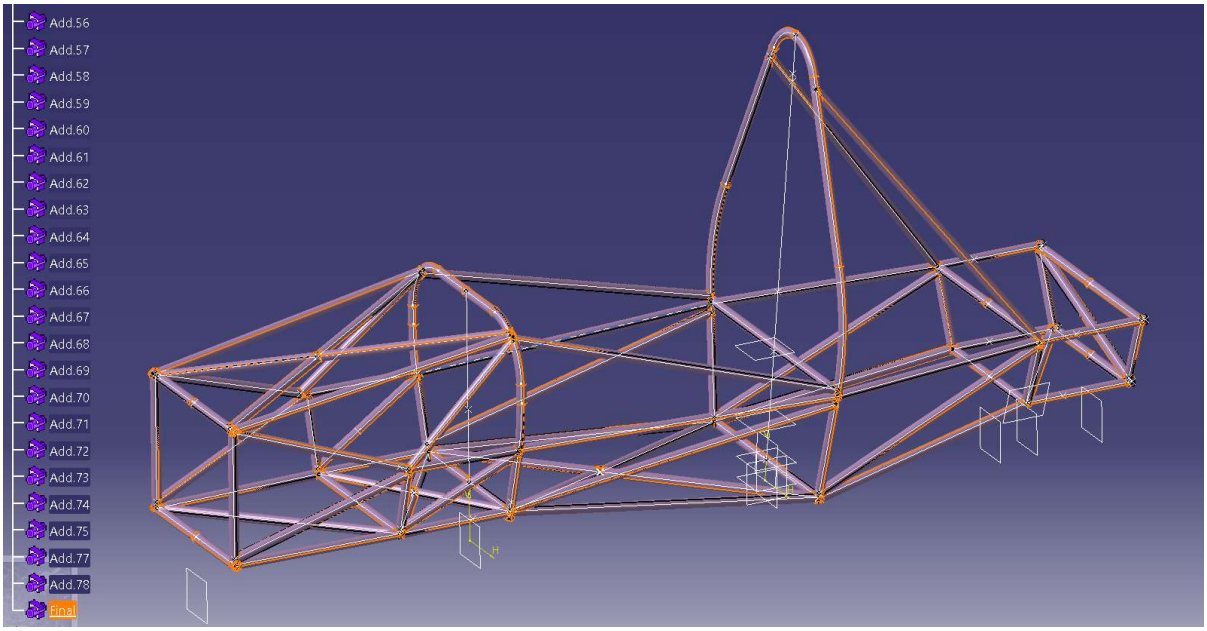

Figure 98: Complete solid entity of the chassis.

3.6 Rules compliance – Material

The design of the chassis was made in accordance with the Formula Student 2023 Rules. All the structural dimensions of the chassis were within the given limits, as they are described in ***Figure 103***. The first type of tubes aforementioned, have an internal radius of 10.5 mm and wall thickness of 2 mm; given the minimum 1.2 mm wall thickness of the regulations was by far within the limits. More specifically, the majority of the metal rods of the chassis were 0.8 mm thicker than the minimum wall thickness, while some parts of the Side impact structure were 1.4 mm thicker, because they belonged to the second type of the tubes used. The second type had an internal radius of 9.9 mm and a wall thickness of 2.6 mm; given the minimum 2 mm wall thickness of the regulations, were also within the limits. The main and front hoops and shoulder harness mounting bar, which, as mentioned before, was part of the main hoop, were all 0.6 mm thicker than the minimum allowed wall thickness.

Item or application	Minimum wall thickness	Minimum cross-sectional area	Minimum area moment of inertia
Main and front hoops, shoulder harness mounting bar	2.0mm	175mm^2	11320mm^4
Side impact structure, front bulkhead, roll hoop bracing, driver's restraint harness attachment (except as noted above)	1.2mm	119 mm^2	8509 mm^4
Front bulkhead support, main hoop bracing supports	1.2mm	91 mm^2	6695 mm^4

Figure 99: Minimum Material Requirements.

The primary structure of the car, according to the rules, has to be constructed with mild or alloy steel, with a minimum of 0.1 carbon. The tubes that were used were steel tubes ST37.4 (DIN 1630). The composition of this material was maximum 0.17% Carbon by mass, max. 0.35% Silicon, max. 0.04% Phosphorus, max. 0.04% Sulfur and no less than 0.35% Manganese and 0,020% Aluminum. The non-welded strength of the material, according to the rules, had to be 200 *GPa* for the Young's Modulus (E), 305 *MPa* for the Yield Strength (Su) and 365 *MPa* for the Ultimate Tensile Strength (Su). The ST37.4 certifications have a minimum of 235 *MPa* for the Yield Strength and 350 to 480 *MPa* for the Ultimate Tensile Strength, as depicted in ***Figure 127***, which are all in compliance with the racing rules.

4. Torsional Analysis

The following step of this study corresponds to the torsional analysis of the chassis. For this kind of analysis, a different workbench of CATIA had to be selected, the Analysis & Simulation Workbench (***Figure 104***).

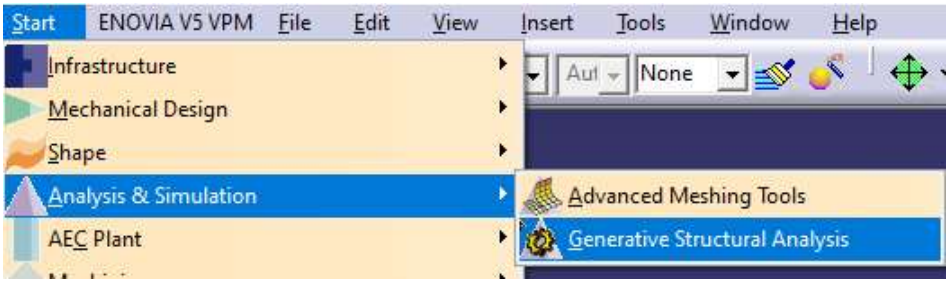

Figure 100: Generative Structural Analysis option.

In that environment it was possible to make a Stress Analysis and see how the chassis structure could handle different loads applied to it and which specific areas were the most stressed. The other result of the analysis that was relevant to this study was the computation of displacements. These values are computed in the surfaces of the constructed model and show how much had a point in the stressed structure, moved from its original position. This analysis helps to validate that the design work is valid and efficient.

For the Analysis Workbench (***Figure 105***) in order to calculate the stress and the deformation of the chassis, a configuration was necessary. The setup of the environment was done in five main steps.

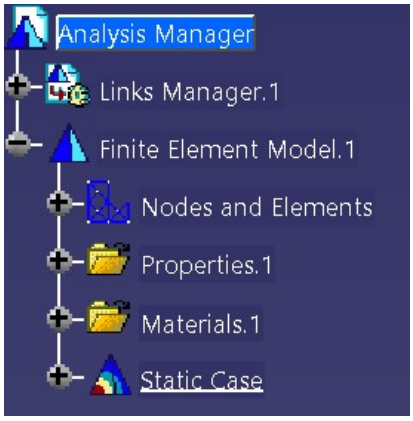

Figure 101: The parameters of Analysis Manager.

The first step was to choose the correct and optimal mesh for the 3D model. The kind of the mesh that the software was able to analyze the surface of the model with, was the Linear OCTREE Tetrahedron Mesh. For CATIA V5 to be able to make the calculations needed, it had to discretize the chassis into smaller components, called mesh elements. These mesh elements

are connected to each other at points called nodes. In our case, tetrahedron (4 nodes) mesh elements were used to approximate the volume of the chassis (***Figure 106***). The discretization of the Partial Differential Equations into all the available elements and the solution of the resulting system of algebraic equations provides the stresses and deflections in every node of the mesh.

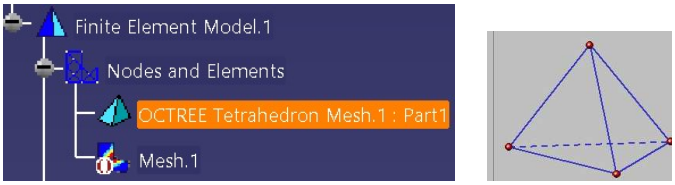

Figure 102: OCTREE Tetrahedron Mesh option.

Two parameters had to be defined for the mesh, the mesh size and the mesh sag (***Figure 107***). The mesh size is the size of the mesh elements. The value that can be set is the length of each edge of a tetrahedron. The absolute mesh sag is the maximum gap between the mesh and the geometry.

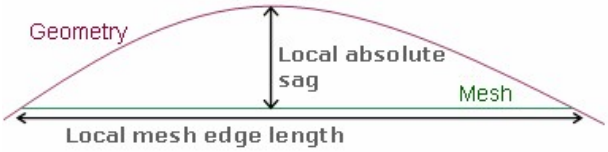

Figure 103: Mesh size and mesh sag visual explanation.

The difference of absolute and proportional sag is that the second is the ratio between the local absolute sag and the local mesh edge length.

After a lot of trials and failed computations the final values of these two parameters were set to 1.6 mm for the mesh size and 0.4 mm for the mesh sag (***Figure 108***). The fails were caused by the input of very small values, in an attempt to find better approximation of the surface and therefore the result was a faulty mesh that couldn't be processed.

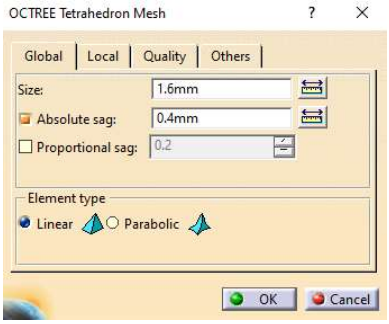

Figure 104: Mesh parameters.

The selection of the correct values was very time consuming, because in the one hand a small size of mesh elements gives better approximation, but in the other hand the number of nodes

grows also, along with the number of equations that have to be solved. For the visualization of the mesh that was applied, the "Shading with Edges" option was enabled (***Figure 109***).

The mesh of the chassis is presented in the ***Figure 110*** and an example of two random tetrahedrons that constitute the mesh is presented in the ***Figure 111***.

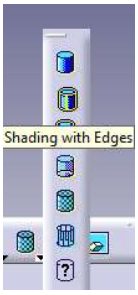

Figure 105: The option that visualize the mesh of the chassis.

Figure 106: The mesh of a part of the chassis.

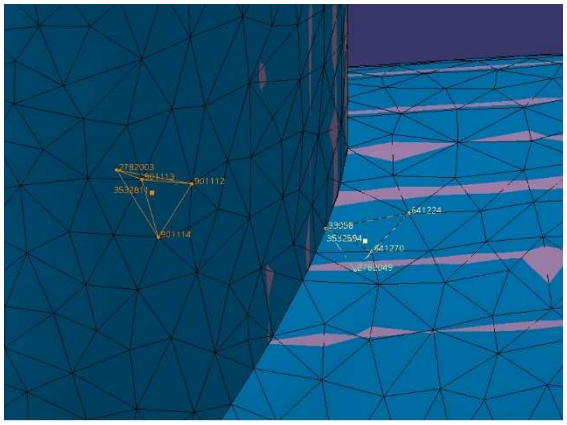

Figure 107: Two examples of tetrahedrons.

The second step was the selection of the material. The obvious choice for the defined material is Steel, same as the material of the actual chassis (***Figure 112***).

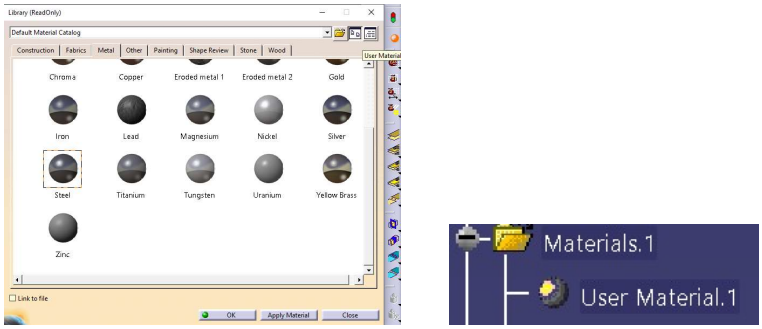

Figure 1082: Material selection.

For the visualization of the material that was applied, the "Shading with Material" option was enabled (***Figures 113, 114***).

Figure 109: The option to visualize the material of the chassis.

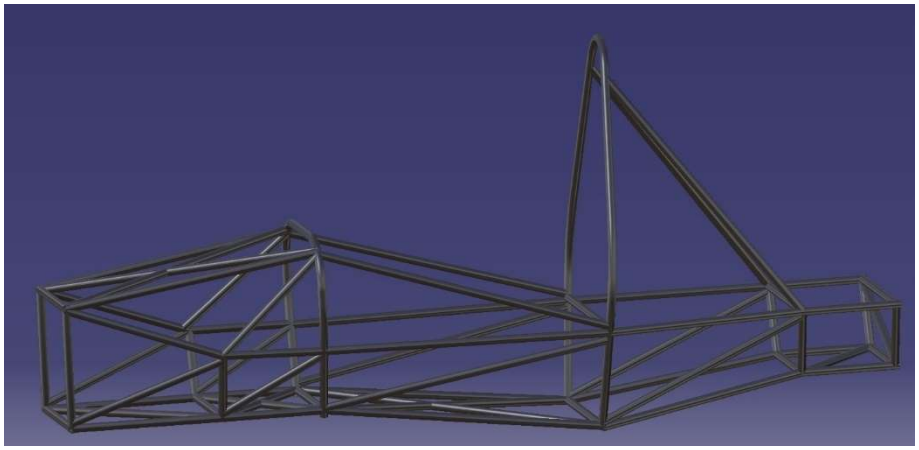

Figure 110: The chassis after the material selection.

The third step was to define the "3D Property" and the whole chassis was chosen as one solid 3D entity (***Figure 115***).

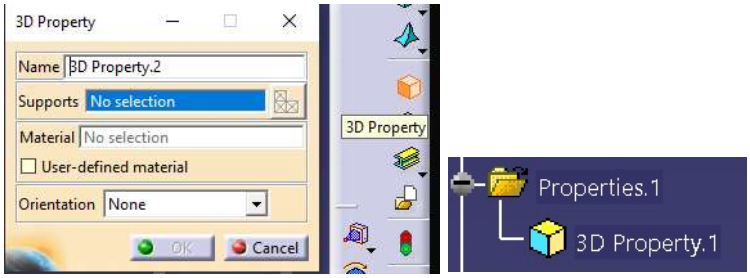

Figure 111: Seting the chassis as 3D property.

Continuing to the fourth step, the chassis had to be restricted of its movement, when the forces will be applied. For the chassis to be analyzed for stress and deformation, fixed points have to be defined. The tool "Clamp" was chosen and it was applied to 3 of 4 suspension areas of the chassis with the purpose of immobilizing them. An example of a clamp is presented in ***Figures 116-118***.

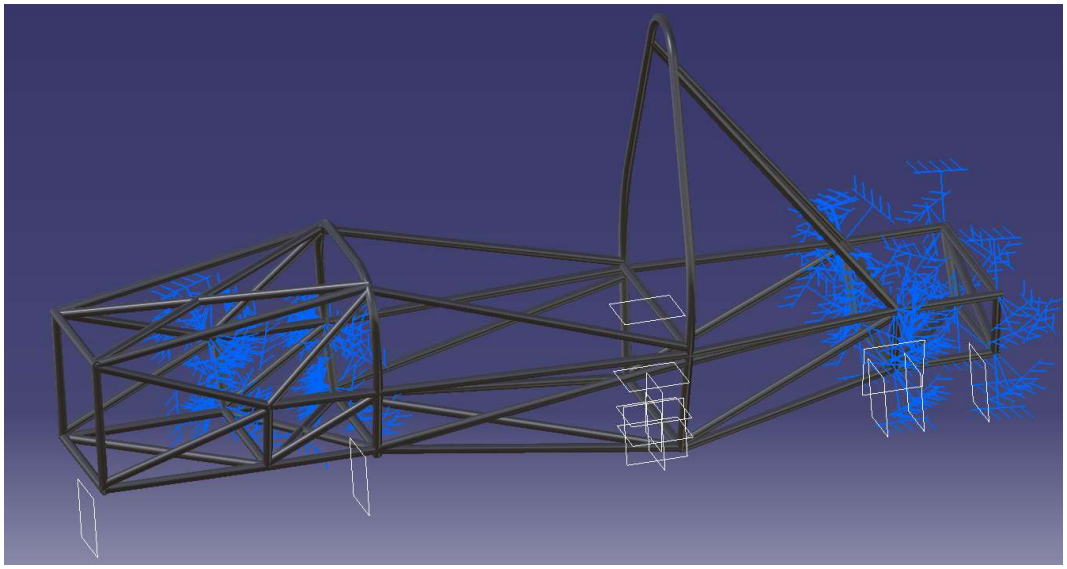

Figure 112: Chasis with the clamped nodes.

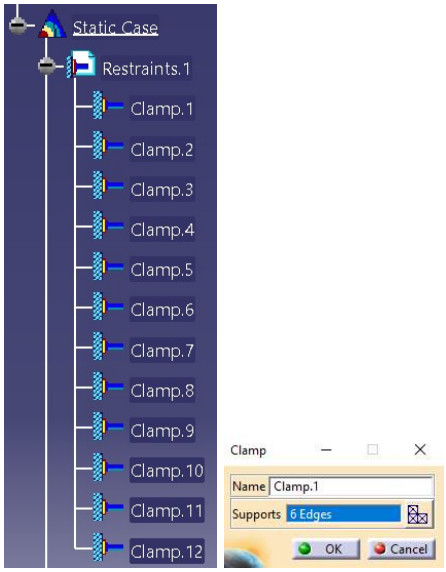

Figure 113: Example of a clamp set up.

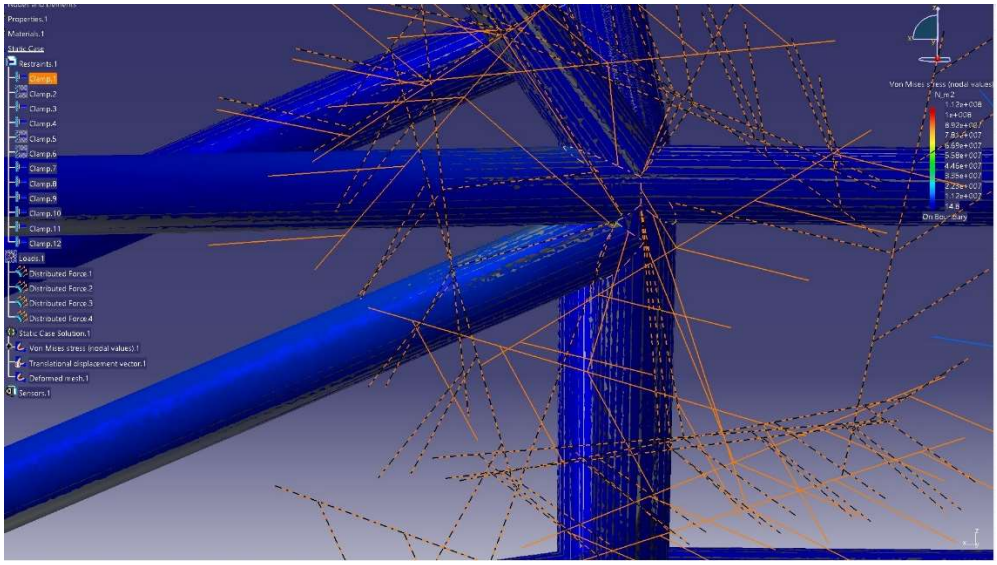

Figure 1148: The edges that had been set for Clamp.1.

The front left suspension was not clamped (immobilized) because it was the area where the loads will be later exerted (***Figure 119***).

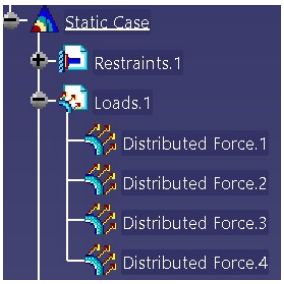

Figure 1159: The four loads setted for the analysis.

The last step of the parameterization of the analysis was the setup of the loads. Each suspension area had 4 main junctions and at each one of them a single force will be applied (***Figure 120***).

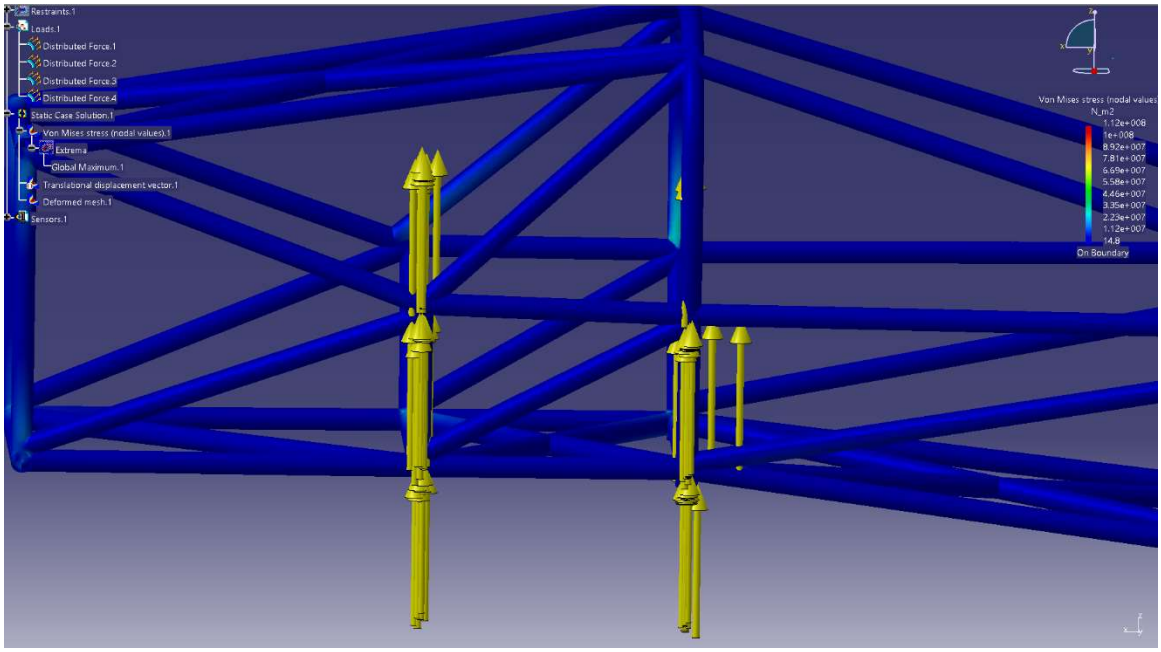

Figure 11620: Visual of the loaded suspention juctions.

The corresponding rod junctions do not have one specific point for the force to be exerted on, so the edges throughout the node area had to be chosen as the force application points (***Figure 121***).

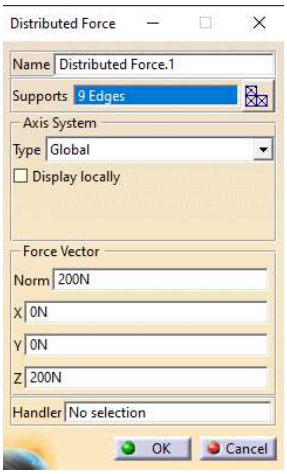

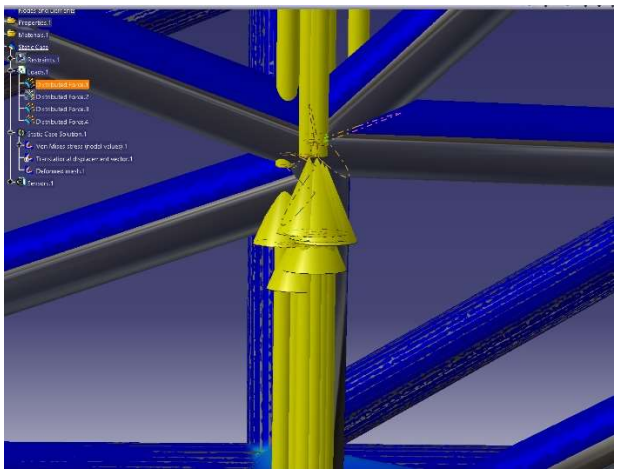

Figure 11721: Example of a load set up.

The simulations would start with a force of 200 N (20 *kg*) per junction and continue with 400 N, 600 N, 800 N and 1000 N. The force was set per junction, so the total force applied in each run in presented in the following table:

Force (per junction)	Total Force on the suspension
200 N	800 N
400 N	1600 N
600 N	2400 N
800 N	3200 N
1000 N	4000 N

Starting from 200 N at each junction, it would sum up to 800 N of force applied for the first run of the calculations and accordingly continued for the rest of the simulation runs (***Figure 122***).

The same set up as in the first node, would respectively be applied in the 3 other junctions.

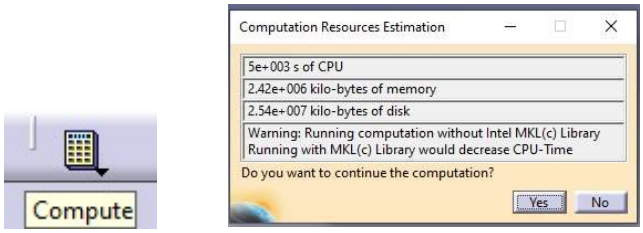

Figure 118: Compute option and Computation resources estimation.

5. Results

Following the configuration of this analysis, the first run of the calculations was performed. The results that were relevant for this study were those of the Von Mises Stress and the deformation of the chassis. Those two options were available in the workbench after the calculations concluded (***Figure 123***).

Figure 119: Von Mises option.

Starting with the Von Mises Stress results, it was possible to determine the most stressed areas of the chassis structure. As ***Figure 124*** shows, the difference in colours signified the difference in the stress value in that part of the chassis and it goes from the least stressed areas with colour blue, to the most stressed areas with colour red.

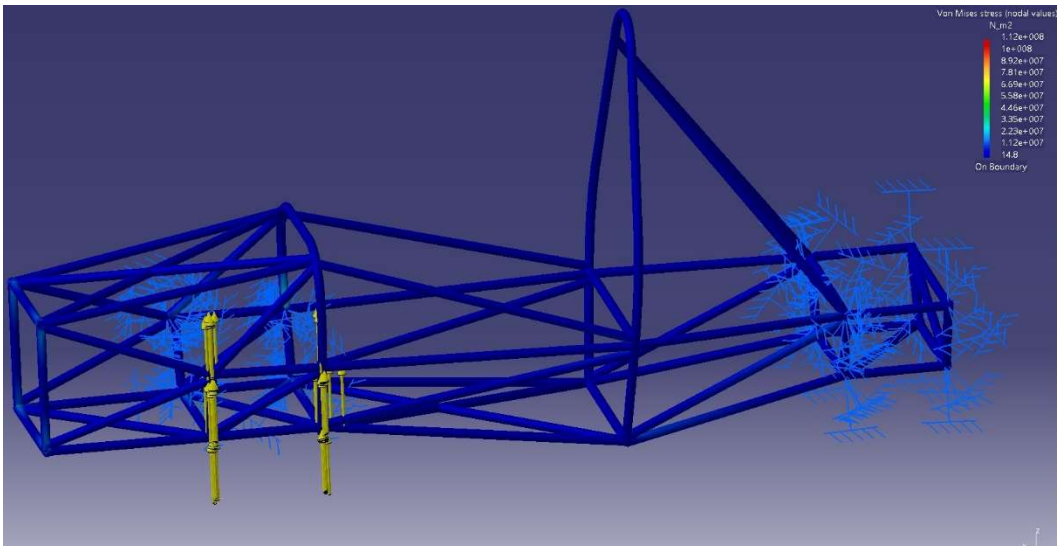

Figure 1204: Visual representation of the Von Mises stresses on the chassis.

The areas that were the most stressed, are located in the opposite side of the suspension, where the force was exerted. Across the simulations, the least and most stressed areas remained the same, with the only change being the maximum values of the corresponding results.

The option “Image Extrema” (***Figure 125***) presented the global maximum stress point, allowing the most stressed part of the structure to be identified. That point was located at the bottom of the front right suspension, a reasonable area considering the place and direction of the loads (***Figure 126***). The value of the point according to the amount of force can be shown in the following table.

Force (per junction)	Max Global Stress	Total Force in Megapascals
200 N	1.11539 e+008 N/m^2	111.539 MPa
400 N	2.23079 e+008 N/m^2	223.079 MPa
600 N	3.34618 e+008 N/m^2	334.618 MPa
800 N	4.46157 e+008 N/m^2	446.157 MPa
1000 N	5.57696 e+008 N/m^2	557.696 MPa

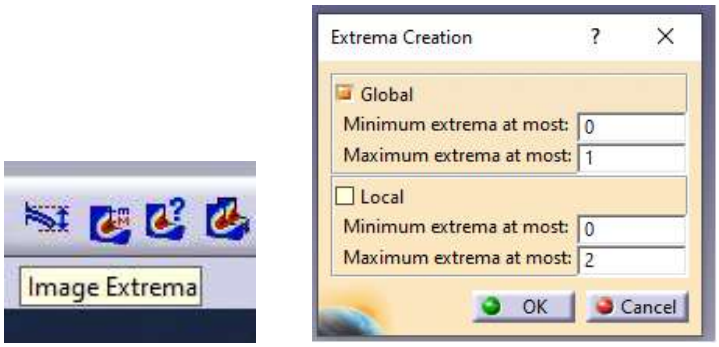

Figure 1215: Image Extrema option and set up.

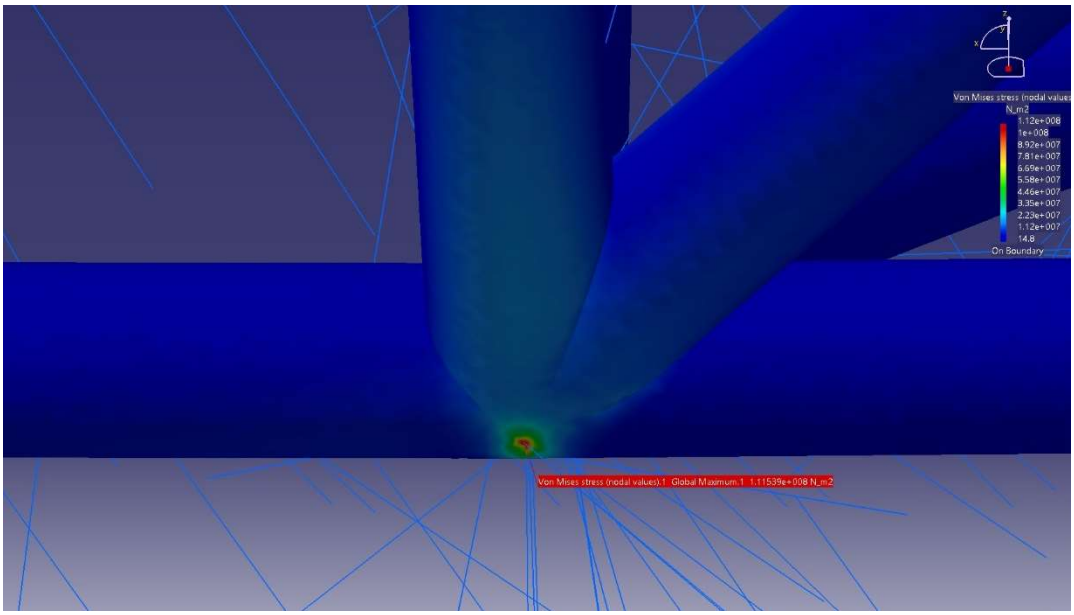

Figure 1226: The global max point location of Von Mises stress.

These results had to be evaluated and compared with the Yield Point (proof stress) (***Figure 127***) of the construction material, which had an average value around 300 *MPa*. This tolerance was acceptable considering the conditions of this study.

Skúška ťahom - *Tensile test - Prova di trazione* : 20 °C

C. Nr.	Číslo tavby *Cast number* *Numero di colata*	Medza klzu *Yield point - Proof stress* *Limite di snervamento*	Pevnosť v ťahu *Tensile strength* *Carico di rottura*	Ťažnosť *Elongation* *Allungamento*
		ReH/ MPa/	Rm/ MPa/	Lo= A5,65/ %/
	Predpis - *Requirements - Richiestt* : min. max.	235 —	340 480	25.0 —
1	45917	312	423	38.0
2	47316	317	420	39.3
3	50504	294	407	40.0

Figure 1237: The steel's certifications.

The chassis was stressed at the first two runs of simulations, with 800 N and 1600 N of total force. At the third run, in which 2400 N of total force was exerted, the material leakage threshold was exceeded with a result of 334.618 *MPa*. The following simulations were performed for the purpose of understanding the performance of the chassis for higher applied forces (***Figure 128***).

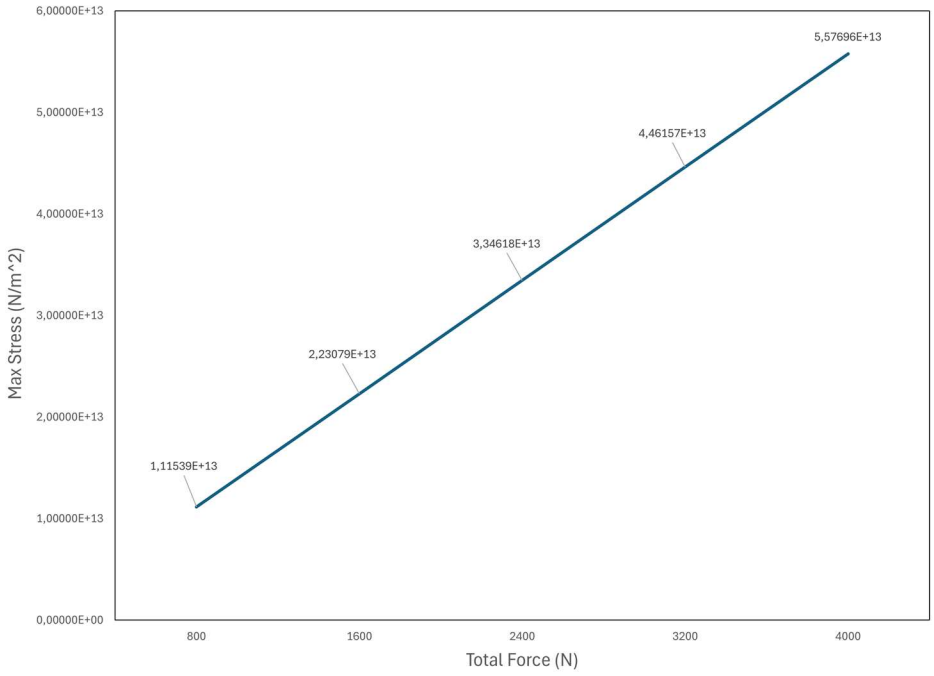

Figure 1248: Max Stress-Total Force graph.

The simulated scenarios helped to ascertain the behavior of the chassis in very difficult situations and intense loading conditions. In reality, all of the suspensions are working together and share the load.

The diagrams (***Figures 129-132***) show the increase of stress values in accordance to the force exerted at each run. Each diagram corresponds to one of total of four nodes of the suspension. With this way, the behavior of each part of the suspension can be studied.

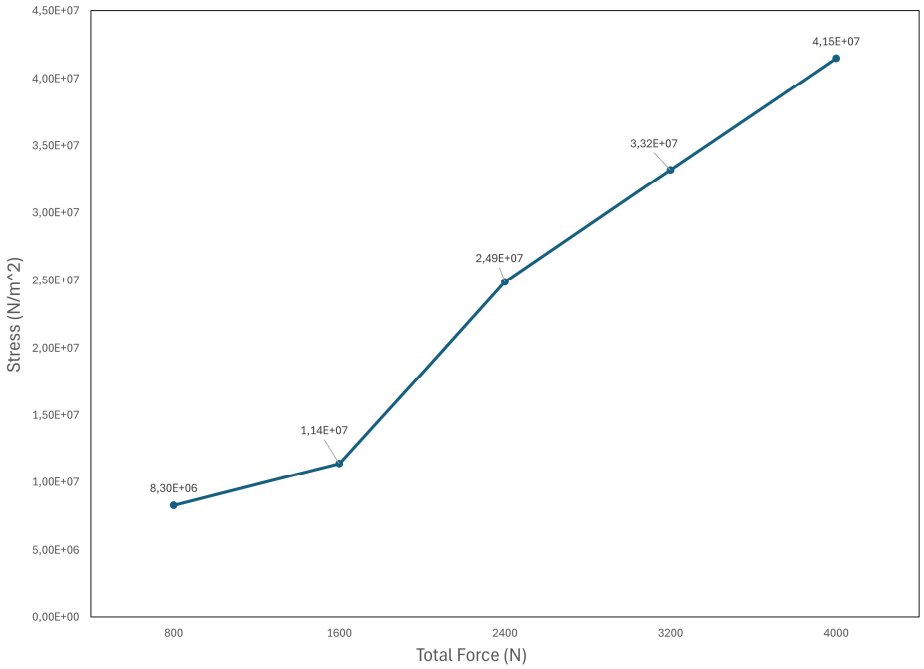

Figure 1259: Stress-Total Force graph at the first juction.

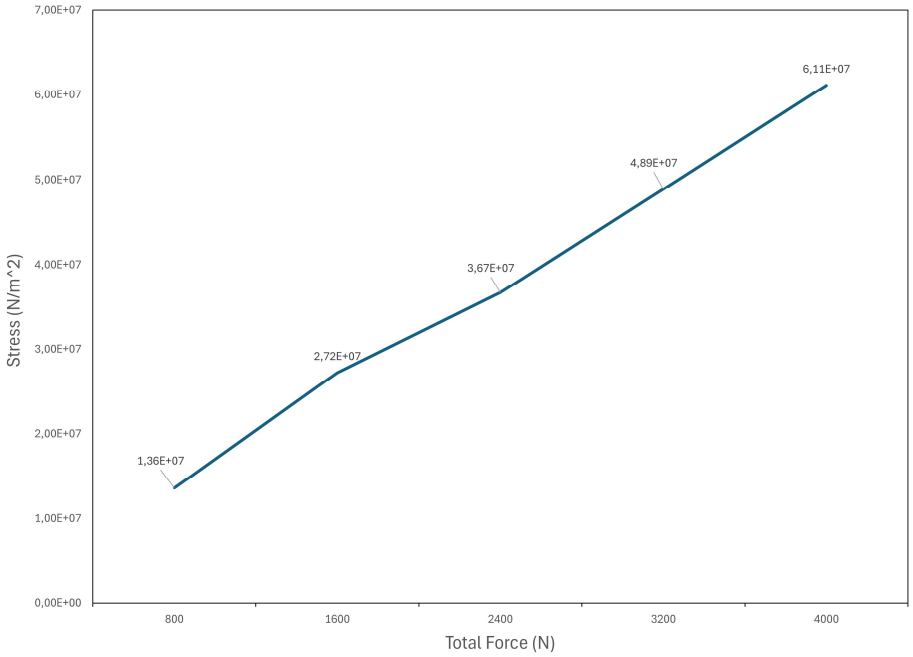

Figure 12630: Stress-Total Force graph at the second juction.

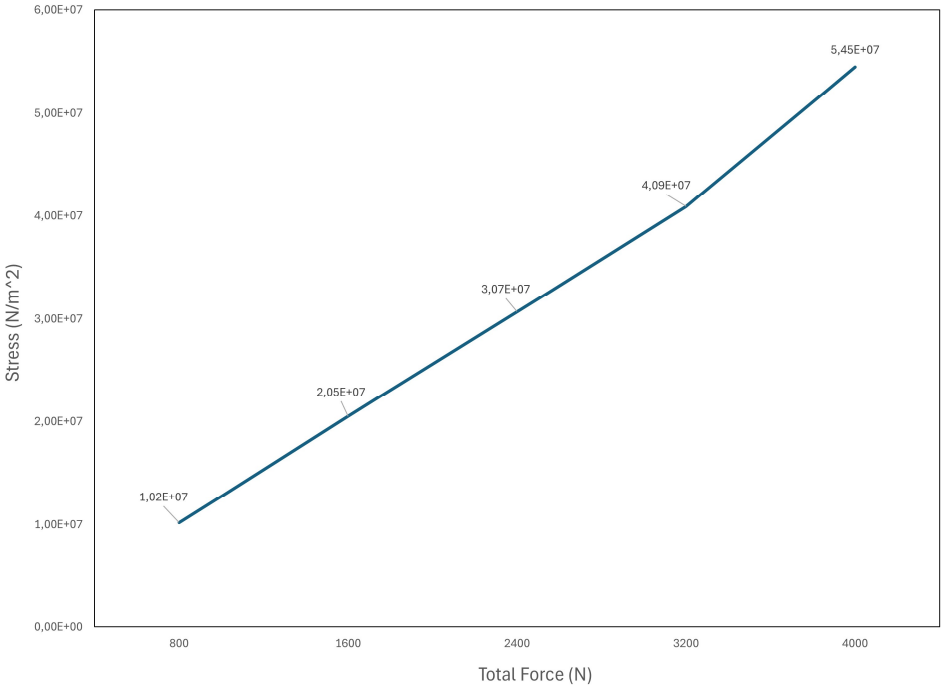

Figure 12731: Stress-Total Force graph at the third juction.

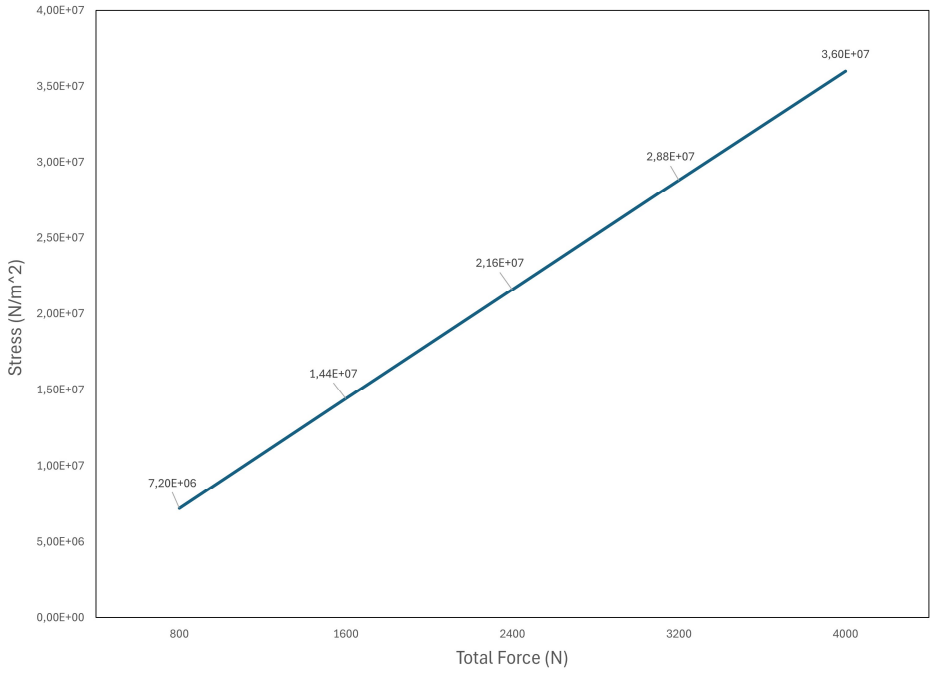

Figure 1282: Stress-Total Force graph at the forth juction.

Continuing with the deformation results, the most deformed part of the chassis was the area from the left half of the Front Bulkhead part, up to the suspension, where the loads were exerted. The said area is depicted in ***Figures 133, 134*** with red coloring.

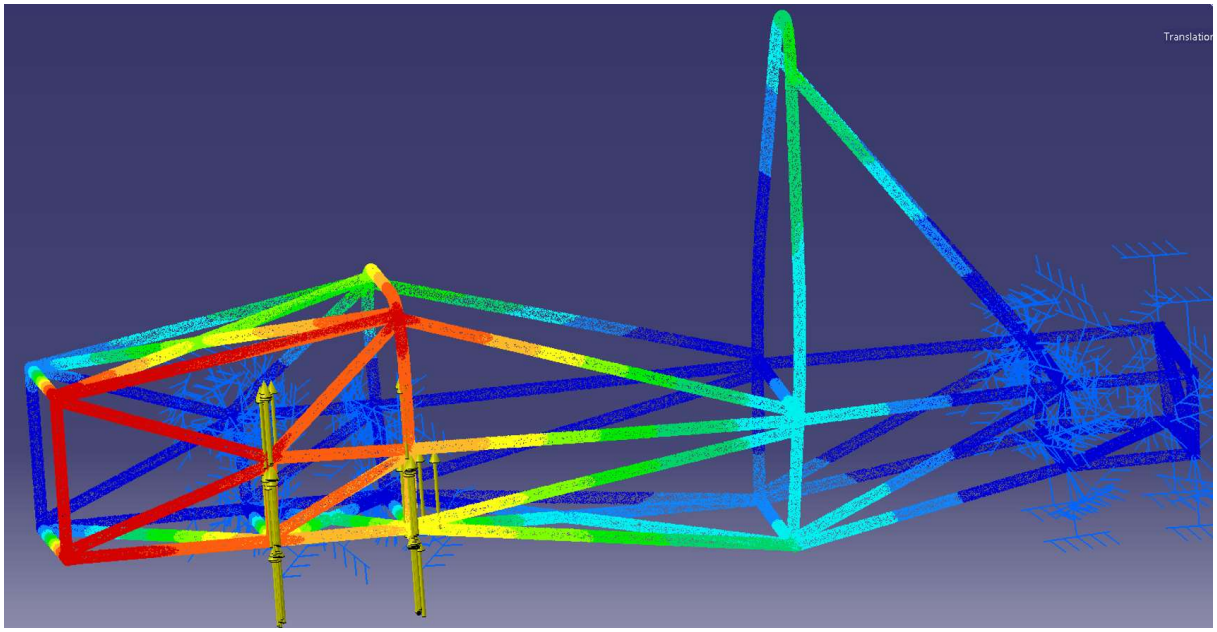

Figure 129: Visual respresentation of the chassis deformation.

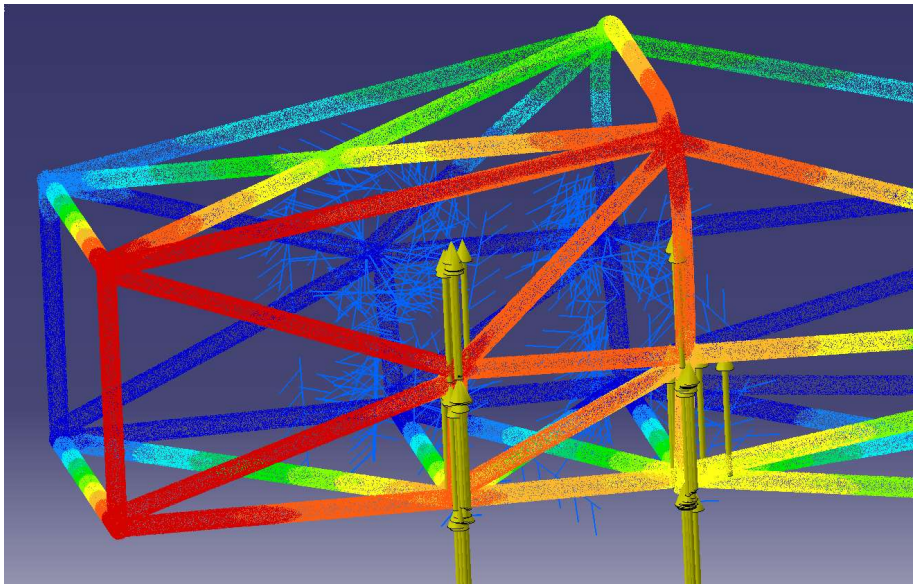

Figure 130: Visual respresentation of the chassis deformation (Closeup).

The maximum stress point had small deformation as ***Figure 135*** depicts.

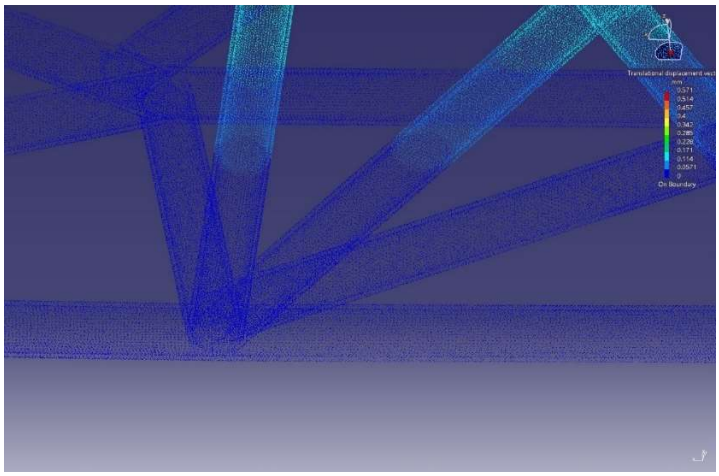

Figure 131: Deformation in the Global max stress point area.

The following diagrams (***Figures 136-140***) show the increase of deformation values in accordance to the force exerted at each simulation run. The linear variation is compatible with the simulation of linear deformations with the utilized solver (no plastic deformations are encountered).

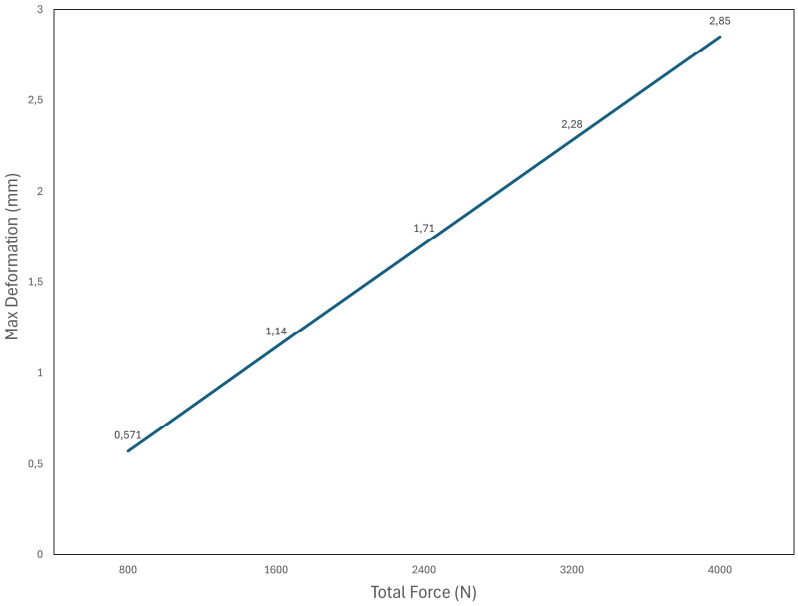

Figure 132: Max Deformation-Total Force graph.

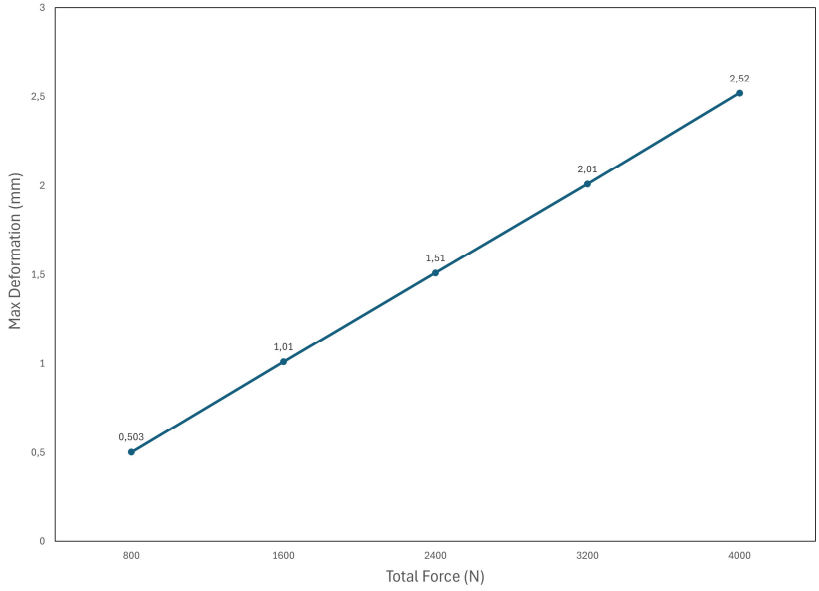

Figure 133: Max Deformation-Total Force graph at the fist juction.

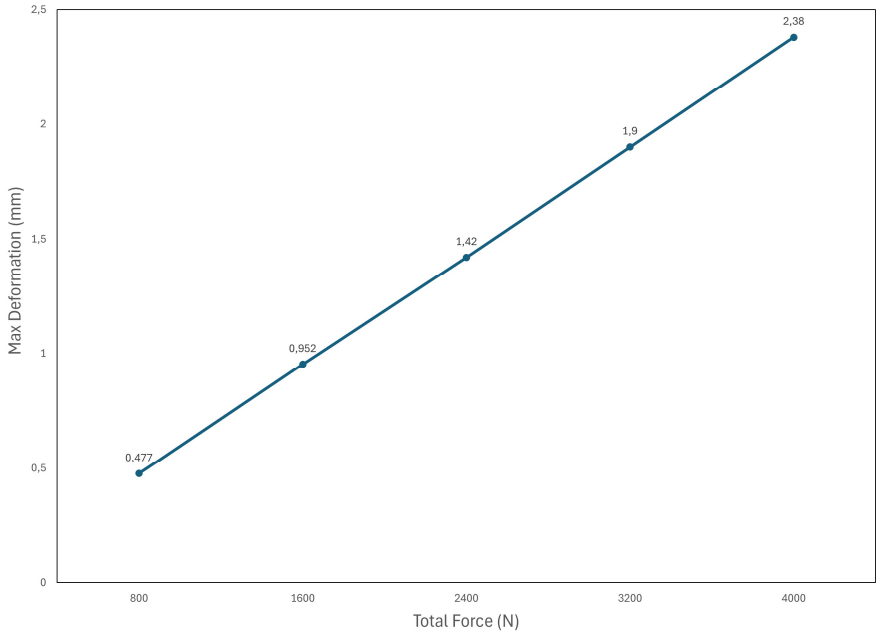

Figure 134: Max Deformation-Total Force graph at the second juction.

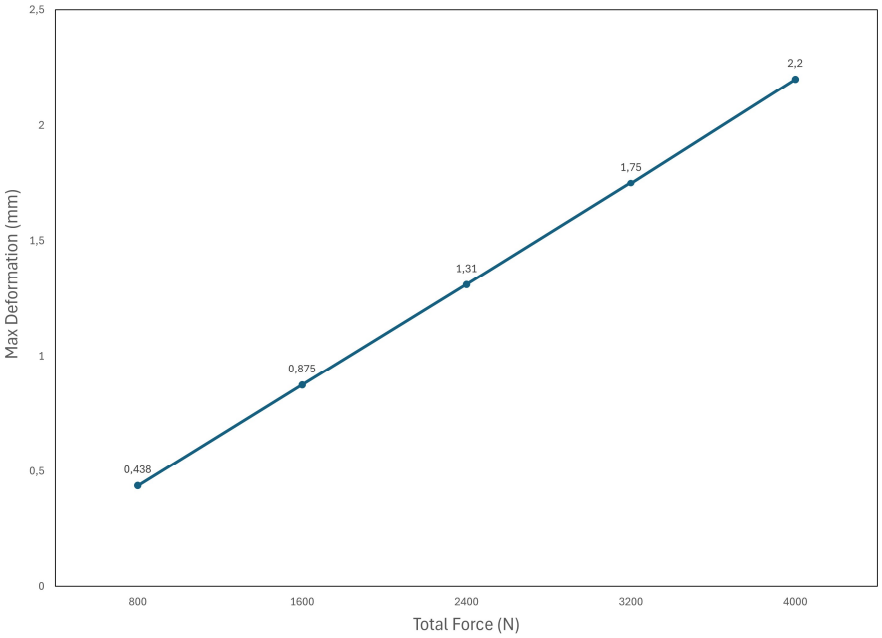

Figure 135: Max Deformation-Total Force graph at the third juction.

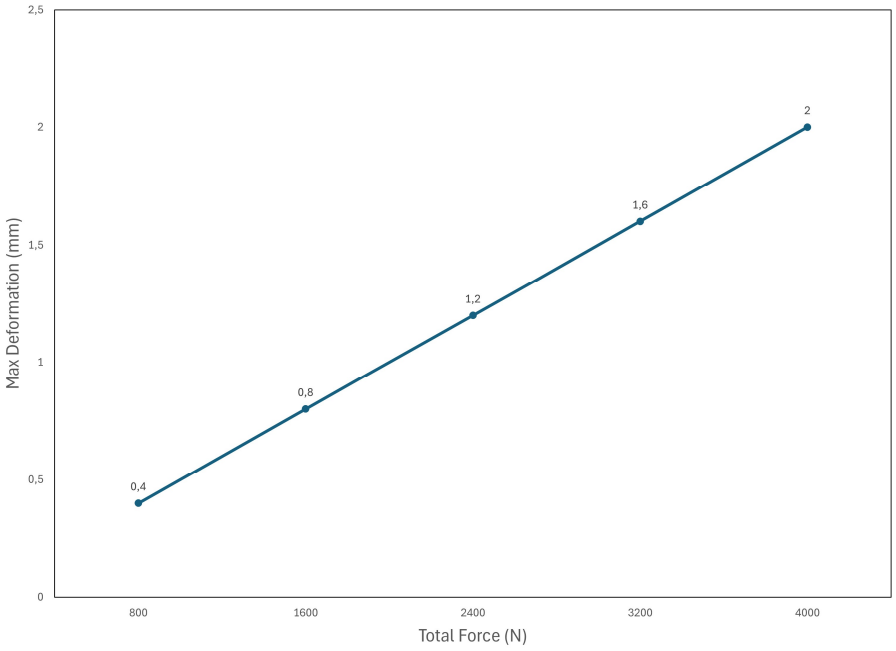

Figure 13640: Max Deformation-Total Force graph at the forth juction.

5.1 Rule compliance – Steel Properties

The Formula Student's 2023 rules limits for the steel properties are being described in the ***Figure 141***. The Yield Strength (Sy) of 305 *MPa* is the limit that was relevant to this torsional analysis.

T3.2.4 The steel properties used for the calculations in the SES must be:

Non-welded strength for continuous material calculations:

i. Young's Modulus (E) = 200 GPa

ii. Yield Strength (Sy) = 305 MPa

iii. Ultimate Strength (Su) = 365 MPa

Welded strength for discontinuous material such as joint calculations:

i. Yield Strength (Sy) = 180 MPa

FORMULA STUDENT

ii. Ultimate Strength (Su) = 300 MPa

Figure 13741: Formula Student Rules 2023 for the steel properties.

The construction material characteristics were previously described in ***Figure 127*** which gave an average value around of 300 *MPa*, being within the regulation limits. The torsional analysis put those characteristics to test. The results showed that the structure withstood 1600 N of force (223.079 *MPa*) and it failed at 2400 N of force (334.619 *MPa*). However, the regions where the stresses went beyond that limit were very small. These problematic regions can be further reinforced very easily, so as to withstand higher forces.

6. Conclusions

In this Diploma Thesis a new 3D geometrical model of the base structure of the Formula Student TUC team's chassis was constructed, based on the real dimensions of the chassis. This was accomplished after the precise measurements of all the dimensions of the constructed chassis. The CATIA V5R20 was used for the construction of the digital CAD model of the chassis.

The design approximated the physical structure in a very detailed manner, which gave the opportunity to conduct simulation tests with accurate results. With the conducted simulations the regions with the higher stresses and deformations have been depicted. The results are very rational and a linear variation of stresses and deformations with the loads was observed. The computed maximum deformations were very small, even for the higher loads, in the order of 2 mm. This is a very good result and shows that the chassis has a high rigidity. The areas where the maximum stresses exceed the limits can be easily reinforced, by adding material.

7. References

Chikkali, V., Patil, R., 2020. FEA Analysis of FSAE Chassis. *International Journal of Engineering Researh & Technology (IJERT),* 9(07).

Cravero, C., Marsano, D., 2022. Computational Investigation of the Aerodynamics of a Wheel Installed on a Race Car with a Multi-Element Front Wing. *Fluids,* 7(6), 182.

Dharmawan, M.A. et al., 2018. Aerodynamic Analysis of Formula Student Car*, AIP Conference Proceedings*, 1931, 030048.

Doddegowda, P., George, A.R., Bychkovsky, A.L., 2006. Use of Computational Fluid Dynamics for the Design of Formula SAE Race Car Aerodynamics*, SAE World Congress*, Detroit, Michigan.

Ghosh, A. et al., 2018. Structural Analysis of Student Formula Race Car Chassis. *International Researsh Journal of Engineering and Technology (IRJET),* 05(12).

Hetawal, S., et al., 2014. Aerodynamic Study of Formula SAE Car. *Procedia Engineering*, 97, pp. 1198-1207.

Jackson, F., 2018. Aerodynamic optimisation of Formula student vehicle using computational fluid dynamics. *Fields journal of Huddersfield student research*.

Jalappa, G.B., 2015. *Design and Optimization of Undertray for Formula SAE Race Car Using CFD Analysis,* MSc Thesis, University of Texas at Arlington.

Mariani, F., Poggiani, C., Risi, F., Lorenzo, S., 2015. Formula-SAE Racing Car: Experimental and Numerical Analysis of the External Aerodynamics. *Energy Procedia*, 81, pp. 1013-1029.

Parmar, P., et al., 2018. Aerodynamic Optimisation of Formula Student Car. *IJCRT,* 6(2) ISSN: 2320-2882.

Pathak, R., 2020. CFD and FEA Analysis of Formula SAE Student Car for Optimum Performance. *EPRA International Journal of Research and Development (IJRD),* 5(3).

Putsala, K.S.K., Rao, P.K.V., Muthupandi, M., Mojeswararao, D., 2022. Numerical analysis on space frame chassis of a formula student race car. *Materials Today: Proceedings,* 66, pp. 754-759.

Rizal, N.E.M. et al., 2012. Aerodynamics of ARTeC's PEC 2011 EMo-C Car. *Procedia Engineering*, 41, pp. 1775-1780.

Shukla, S., Agnihotri, S., Sahoo, R.R., 2016. Design and Analysis of Formula SAE Chassis. *Journal of Aeronautical and Automotive Engineering (JAAE),* 3(1).

Singh, R.P., 2010. Structural Performance Analysis Of Formula SAE Car. *Jurnal Mekanikal ,* 31, pp. 46-61.

Tzanakis, A., 2012. *Conceptual and aerodynamic design of an urban vehicle,* Diploma Thesis, Technical University of Crete, Greece.

Octree Mesher (maruf.ca)